Universidade de Aveiro
2018

Departamento de Química

Cátia Daniela Jordão Leal

Remoção de AOX de efluentes da indústria da pasta de papel por fotocatálise heterogénea

Removal of AOX from pulp mill industry effluents by heterogeneous photocatalysis

Universidade de Aveiro
2018

Departamento de Química

Cátia Daniela Jordão Leal

Remoção de AOX de efluentes da indústria da pasta de papel por fotocatálise heterogénea

Removal of AOX from pulp mill industry effluents by heterogeneous photocatalysis

Dissertação apresentada à Universidade de Aveiro para cumprimento dos requisitos necessários à obtenção do grau de Mestre em Engenharia Química, realizada sob a orientação científica da Doutora Ana Luísa Daniel da Silva, Investigadora Auxiliar no Laboratório Associado CICECO do Departamento de Química da Universidade de Aveiro, e da Doutora Paula Cristina de Oliveira Rodrigues Pinto, Investigadora do RAIZ – Instituto de Investigação da Floresta e do Papel

Este trabalho foi desenvolvido no âmbito do projeto PROTEUS - POCI-01-0247-FEDER-017729, financiado pelo Portugal 2020 através do Fundo Europeu de Desenvolvimento Regional (FEDER), enquadrado no Programa Operacional Competitividade e Internacionalização (POCI).

o júri

presidente

Professora Doutora Maria Inês Purcell de Portugal Branco
Professora Auxiliar do Departamento de Química da Universidade de Aveiro

Doutora Márcia Carvalho Neves
Investigadora de Pós-Doutoramento, CICECO - Universidade de Aveiro

Doutora Paula Cristina de Oliveira Rodrigues Pinto
Investigadora, RAIZ – Instituto de Investigação da Floresta e do Papel

agradecimentos

Esta dissertação é o culminar de uma vida académica repleta de alegrias e bons momentos e gostaria de demonstrar o meu reconhecimento e gratidão a todos aqueles que me acompanharam ao longo destes anos e, em particular, ao longo deste trabalho.

Começo por deixar o meu agradecimento à Doutora Ana Luísa Silva pela sua orientação e partilha de conhecimento, pelo seu incentivo, estímulo e constante acompanhamento, que considero ter sido fundamental.

Agradeço ao RAIZ, em especial, à Doutora Paula Pinto, pela oportunidade e apoio demonstrado, e à Sofia Caldeira e à Teresa Rodrigues por toda a ajuda oferecida nas medições de AOX.

A quem me ajudou na caracterização dos materiais, em particular, à Marta Ferro, pelas sessões de TEM e à Ana Estrada e à Rosário Soares, pelas análises de XRD.

Ao Professor João Labrincha e ao Rui Novais do Departamento de Engenharia de Materiais e Cerâmica, pela partilha e disponibilização das esferas geopoliméricas.

Aos colegas de laboratório do NanoLab, CICECO, pela vossa disponibilidade, pela ajuda na síntese dos nanomateriais, pelos conselhos e pela boa disposição todos os dias.

Aos amigos que estão comigo desde sempre e aos amigos que este curso me deu, pela amizade, companheirismo e incentivo contínuo.

Por último, mas não menos importante, gostaria de agradecer à minha família por todo o amor e apoio incondicional.

Obrigada a todos!

palavras-chave

Fotocatálise, compostos halogenados adsorvíveis, efluente de branqueamento, dióxido de titânio, magnetita

resumo

Nos últimos anos, as fábricas da pasta de papel têm enfrentado desafios na gestão do tratamento de efluentes, devido ao aumento da produção dos mesmos e às preocupações ambientais, relacionadas com a necessidade de cumprir limites de descarga que são cada vez mais rigorosos e impostos por nova legislação.

Os efluentes gerados na etapa de branqueamento contêm, entre outros poluentes orgânicos, compostos halogenados adsorvíveis (AOX) que podem ser foto-oxidados com radiação ultravioleta. Existem fortes evidências que confirmam a eficiência das nanopartículas de dióxido de titânio (TiO_2) como fotocatalisador na degradação de compostos AOX. No entanto, há a necessidade de desenvolver suportes para o nano-TiO_2, de modo a permitir a sua recuperação e reutilização em ensaios fotocatalíticos consecutivos, sendo este o principal objetivo desta tese.

Assim, neste trabalho investigaram-se duas estratégias independentes: (1) a preparação de nano-TiO_2 com propriedades magnéticas com vista a uma recuperação fácil e rápida por separação magnética e (2) o uso de esferas geopoliméricas contendo TiO_2, que foram produzidas com uma percentagem de cinzas de resíduos da produção da pasta e papel. Todos os materiais preparados foram caracterizados por difração de raio X, espectroscopia (FTIR e UV-vis) e microscopia eletrónica (SEM e TEM).

As nanopartículas de TiO_2 com propriedades magnéticas foram preparadas por co-precipitação *in situ* de magnetite (Fe_3O_4) na presença de TiO_2. Os materiais Fe_3O_4/TiO_2 foram preparados com teores variáveis de TiO_2 (entre 14.0 e 43.5%m/m), sendo compostos por nanopartículas de magnetite e TiO_2, numa configuração irregular e não homogénea. O teor mais elevado de TiO_2 foi obtido para a amostra Fe_3O_4/TiO_2 (1:3) após centrifugação (43.5%).

As esferas geopoliméricas contendo TiO_2 tinham cerca de 3 mm de diâmetro médio e uma superfície porosa. Em termos de composição química, os compostos maioritários são TiO_2 (24%), quartzo (22%) e muscovita (20%).

Numa etapa seguinte, todos os materiais foram testados na degradação fotocatalítica de AOX em amostras reais provenientes do caudal de branqueamento. Os ensaios decorreram durante 1 hora, num fotoreator laboratorial, com adição de H_2O_2 e utilizando luz UV como fonte de radiação. A percentagem de remoção de AOX foi semelhante, independentemente do tipo de suporte utilizado. Os melhores resultados foram obtidos com Fe_3O_4/TiO_2 (1:3) centrifugadas (remoção de 73.3% de AOX) e com as esferas (remoção de 68.9% de AOX). Comparando estes resultados com os de TiO_2 não suportado (76.6%), a eficiência de remoção nos fotocatalisadores suportados foi ligeiramente menor. Além disso, também se observou que o uso de luz UV aumenta o desempenho dos fotocatalisadores, enquanto o tipo de agitação (agitação magnética vs. injeção de ar comprimido) não influenciou de forma significativa os resultados.

A percentagem de catalisador recuperado magneticamente diminuiu com o aumento do teor de TiO_2 e com a exposição à luz UV, sugerindo que estes materiais sejam sensíveis à radiação UV e que percam alguma da sua força magnética durante os ensaios de fotocatálise. Reutilizando os fotocatalisadores recuperados numa segunda série, a remoção de AOX foi relativamente similar às anteriores, com o melhor resultado a pertencer a Fe_3O_4/TiO_2 (1:1), 75.8%, o que provou a sua capacidade de ser eficientemente reutilizado para remover AOX.

As esferas geopoliméricas tiveram a sua superfície e poros degradados após os vários testes de fotocatálise, mas a sua composição química não se alterou significativamente. Estas também foram submetidas a uma segunda série de ensaios que permitiram remover cerca de 65.5% de AOX.

keywords

Photocatalysis, adsorbable organic halides, bleaching effluent, titanium dioxide, magnetite

abstract

In recent years, pulp and paper mills have faced challenges on wastewater treatment management, due to the increase of effluents production and the environmental concerns, related with the need to meet progressively rigorous discharge limits imposed by new legislation.

The effluents generated in pulp bleaching contain, among other organic pollutants, adsorbable organic halides (AOX) that can be photo-oxidized using ultraviolet radiation. There are strong evidences that confirm the efficiency of nanoparticles of titanium dioxide (TiO_2) as photocatalyst in the photodegradation of AOX compounds. However, there is a need to develop supports for nano-TiO_2, in order to allow its recovery and reutilization in consecutive photocatalytic tests, and this is the main aim of this thesis.

Thus, this work investigated two independent strategies: (1) the preparation of nano-TiO_2 with magnetic properties aiming easy and fast recovery by magnetic separation and (2) the use of geopolymer spheres containing TiO_2, that were produced with a percentage of ash from residues of pulp and paper mills. All the materials were characterized using X-ray powder diffraction, spectroscopy (FTIR and UV-vis) and electron microscopy (SEM/TEM).

The TiO_2 nanoparticles with magnetic properties were prepared by *in situ* co-precipitation of magnetite (Fe_3O_4) in the presence of TiO_2. The Fe_3O_4/TiO_2 materials were prepared with variable TiO_2 content (between 14.0 and 43.5wt%) and were composed of nanoparticles of magnetite and TiO_2, in an irregular and non-homogeneous configuration. The highest TiO_2 content was obtained for the sample Fe_3O_4/TiO_2 (1:3) after centrifugation (43.5%).

The geopolymer spheres containing TiO_2 were around 3 mm average diameter, with porous surface. In terms of the chemical composition, the major crystalline compounds were TiO_2 (24%), quartz (22%) and muscovite (20%).

In a later stage, all materials were tested in the photodegradation of AOX present in real bleaching stream samples. The experiments were carried out for 1 hour in a laboratory photoreactor, with addition of H_2O_2 and using UV-light as radiation source. The percentage of AOX removal in all the supported photocatalysts was similar. The best results were attained with Fe_3O_4/TiO_2 (1:3) centrifuged (73.3% AOX removal) and with the spheres (68.9% AOX removal). Comparing with TiO_2 non-supported (76.6%), the removal efficiency on supported photocatalysts was slightly lower. In addition, it was also seen that the use of UV-light increases the performance of the photocatalysts, while the type of stirring (magnetic vs injection of compressed air) did not influence significantly the results.

The percentage of catalyst magnetically recovered decreased with the increase of TiO_2 content and with UV-light exposure, thus suggesting that these materials are sensitive to UV radiation and that they lose some of their magnetic force during the photocatalysis trials. Reusing the recovered photocatalysts in a second run, the AOX removal was relatively similar to the previous ones, with the best result obtained with Fe_3O_4/TiO_2 (1:1), 75.8%, which proved their ability to be efficiently reused to remove AOX.

The geopolymer spheres presented their surface and pores degraded after photocatalysis, but their chemical composition did not change significantly. These photocatalysts were also subjected to a second series of tests, which allowed to remove about 65.5% of AOX.

Index

List of Figures

List of Tables

List of Abbreviations

	Name	Unit
ADt^{-1}	Air-dry tonne of pulp product	-
AOP	Advanced oxidation process	-
AOX	Adsorbable organic halides	$kg \cdot ADt^{-1}$
ATR	Attenuated total reflectance	-
BOD	Biochemical oxygen demand	$kg \cdot ADt^{-1}$
cfg	Centrifuged	-
COD	Chemical oxygen demand	$kg \cdot ADt^{-1}$
e_{CB}^-	Electron on the conduction band	-
ECF	Elemental chlorine free	-
EDS	Energy dispersive spectroscopy	-
E_g	Band gap energy	eV
F_m	Magnetic force	N
FTIR	Fourier-transform infrared spectroscopy	-
h_{VB}^+	Electron gap on the valence band	-
H_a	Applied magnetic field intensity	$A \cdot m^{-1}$
hν	Photon energy	J
μ_0	Permeability	$N \cdot A^{-2} \cdot m$
m	Mass	g
M_p	Magnetization	$A \cdot m^{-1}$
ρ_{sample}	Concentration of AOX on the sample, value not corrected	$mg \cdot L^{-1}$
ρ_{blanck}	Concentration of AOX on the blank test	$mg \cdot L^{-1}$
rec	Recovered	-
SEM	Scanning electron microscopy	-
T	Temperature	°C
TCF	Totally chlorine free	-
TEM	Transmission electron microscopy	-
V	Volume	mL
V_p	Volume of the magnetic particle	m^3
UV	Ultraviolet	-
UV-vis	Ultraviolet-visible spectroscopy	-
XRD	X-ray powder diffraction	-

1. Introduction

1.1 Industry of paste and paper

1.1.1 History of the paper production

The invention of the paper goes back many years ago and it come from different regions of the world, who through different methods and raw materials created what were the precursors of the paper. In the earliest times, man wrote and drew on stones, bones, metals, wood, shells, and many others, and later he found more suitable materials such as papyrus, parchment and paper. [1]

The word "paper" comes from the Latin *papyrus*, the plant that grew on the banks of the Nile River in Egypt and from which were extracted the fibers that served as a surface for hieroglyphic writing since 2700 BC. However, due to the fragility of the papyrus, after the Arabic invasion, the Persians replaced it by the parchment, obtained from animal skin. It was only later, in 105 AC, thanks to Tsai Lun in China that paper began to be produced through the bark trees and textile fibers. [2]

Over the years, papermaking techniques have been improved and knowledge rapidly spread throughout Asia and later throughout Europe, thanks to the Muslim invasions of the eighth century. Later, in the fourteenth century, there were already several paper mills in Europe, particularly in Spain, France and Germany, whose raw materials were linen, hemp and cotton rags. After cleaning, sorting and cutting, these were boiled with potash or soda ash to remove the remaining dirt and colour. Until then, the whole production was quite handmade and manual, but in century XIX, with the increase of the demand of paper for printing of books and newspapers, the German Friedrich Keller developed an industrial method of production of paper from the pulp of wood. [1] [3]

In the last 20 years, the pulp and paper sector has been growing in the world economy because of the continuous increase in pulp and paper production and consumption. It is an industry sector that follows the technological developments associated, to meet the continuous demands of consumers and the increasingly stringent fulfilment of environmental criteria. [4]

1.1.2 Paper production in Portugal

In Portugal, the production of paper began at the end of the century XIV, however, it was only industrialized in XVIII. As mentioned above, in the last century, much progress has been made in this area, both in terms of improving stablished techniques and creating new ones and Portugal following this trend was the first country to produce chemical pulps from eucalyptus using the sulphite technique in 1923 and the sulphate technique (Kraft process) in 1957 in The Navigator

Company, Cacia. Later, on 1993, CELPA, the Pulp Industry Association, was created as a result of the merging of the ACEL (Association of Pulp Producing Companies) and FAPEL (Portuguese Association of Paper and Card Manufacturers). CELPA has associated the four companies responsible for the entire national production of virgin fiber pulp and about 80% of national paper production, namely Altri, Europac, Renova and The Navigator Company. [1] [5]

RAIZ, Forest and Paper Research Institute, located in Quinta de S. Francisco, Eixo, Aveiro, is a private non-profit organization that was established in 1996 as an association between The Navigator Company, University of Coimbra, University of Aveiro and University of Lisbon (School of Agriculture). Its activity is mainly financed by The Navigator Company and other private entities, also receiving national and european public funds. [6]

The organization was created to contribute to the competitiveness and sustainability of the eucalyptus value chain by developing innovative solutions, providing specialized consulting services, boosting the new circulation and organic economy, promoting cooperation with universities and R&D centres and to train highly qualified and motivated human resources. [6]

1.1.3 Productive process

The raw material of this industry is the wood, an organic material mainly composed by carbon (49%), oxygen (44%) and hydrogen (6%), as well as some inorganic elements (Na, Ca, K, Mg, Si) and nitrogen, with little variations between the different species. These elements form polymers, such as cellulose, hemicellulose and lignin, which percentage differ in hardwoods (e.g. *Eucalyptus globulus*) and softwoods (e.g. *Pinus sylvestris*). [3] [7]

Cellulose is the most abundant material (40-47%), followed by hemicellulose (25-39%) and lignin (16-31%). Cellulose is a strictly linear homopolymer consisting of β-1,4-glycosidic linked D-glucopyranose units, while hemicelluloses are heteropolysaccharides formed by pentoses, as xylose, and hexoses, as glucose. The type of polysaccharide present depends once again if it is a hardwood or a softwood. Lignin, as the third major compound of the cell wall, is a complex phenolic polymer formed by the reaction between three hydroxycinnamyl alcohols. [3] [7]

The productive process involves three main steps whose aim is the maximization of the yield, with the minimization of the fiber degradation. In the first step the wood is prepared, the splinters are removed and it is cleaned with water. In the second step, named pulping, the wood is reduced to a fibrous mass, called pulp, by chemical or mechanical processes. The aim of this step is to take the lignin from the wood in way to separate the cellulose and the hemicellulose. Generally, the chemical

processes are much more used and they are based in the degradation and dissolution of lignin through chemical reactions at high temperatures. There are several methods which differ in the pH values range, the reactants, the time period and the temperature of the reaction, and the ones more frequently used are the sulphate (or Kraft) and the acid sulphite technique. [3]

Finally, bleaching is the third step, where the fibers are whitened and washed. There are two types of bleaching, the one that uses reactants based in chlorine, such as Cl_2, ClO^- and ClO_2, and the other that uses reactants based in oxygen, such as O_2, H_2O_2 and O_3. However, the global process of bleaching combines sub-processes using different reactants in a sequence and it can be classified as ECF, elemental chloride free, or TCF, totally chlorine free. All chlorine-based processes are primarily responsible for environmental problems, since they generate effluents with high amounts of chloro-phenols, adsorbable organic halides, among others. So, from the environmental point of view it is more advantageous to use the TCF processes instead of ECF, however due to the high production costs associated and the lower resistance and gloss of the pulp produced, TCF processes currently represent only 5% of the global pulp industry. [8]

1.2 Treatment of wastewaters

Pollution of the environment has been pointed out as one of the biggest problems of the modern society. Because of the growing awareness of this problem, new and increasingly restrictive regulations and legislation have been created to minimize the environmental impact.

One of the sectors most associated to this issue is the industry. The increase in industrial production associated to the emerging global population increase has created several problems, such as overexploitation of natural resources and pollution of soil, air and water. As such, there is a need today to develop new effluent treatment processes which ensure a low level of contaminants. [9]

In general, the priority is to minimize the production of waste and polluting effluents, through improvements in the process and better control of the quality of raw materials. However, currently, another strategy has also been adopted, which promotes the reuse of the effluents and the waste. In terms of energy recovery, through the energy integration on the processes, and in terms of material valorisation, through the production of new products, following the trend of circular economy. [10]

The pulp and paper industry generates considerable amounts of pollutants, mainly due to the increase in water consumption, and is considered the major source of pollution in countries such as China, India and United States of America. In fact, only the primary metals industry and the chemical

industry produce more effluents than the pulp and paper industry. The wood pulping and production of the paper products generate a considerable amount of pollutants characterized by BOD, COD, toxicity and colour, through the untreated effluents discharged to receiving waters. The generated effluents can have in their composition more than 700 organic and inorganic compounds, according to the scale of production, the quantity of water and raw materials used and the technology applied in the production. These compounds are mostly derived from tannins, lignin, resins and chlorinated compounds. Among the various contaminants, the non-biodegradables are those to take more in account, such as the adsorbable organic halides and the phenolic compounds. [11] [12]

Nowadays, there is legislation which determine the maximum amount allowed of each compound in the effluents of the industry. The best available techniques, BAT, and the maximum values allowed for the emissions on this industry are regulated by the Industrial Emissions Directive 2010/75/EU, in Europe. For AOX the yearly average need to be lower than 0.2 $kg \cdot ADt^{-1}$, in wastewaters discharged from a bleached Kraft pulp mill. [13] [14]

1.2.1 Techniques of AOX removal

The adsorbable organic halides, AOX, are formed during the bleaching step of the pulp and can be divided into two categories, according to their molecular weight. Although the compounds with low molecular weight are more hydrophobic and have a greater ability to penetrate membranes, both compounds have toxic effects, such as carcinogenic and mutagenic effects, caused by chronic and acute exposure. This exposure can induce some health problems, such as injuries to various organs, as well in the central nervous system and immune system. [15]

There are several techniques for the treatment of the effluents containing AOX, which can be divided into four categories, namely, physical, chemical, electrochemical and biological. They can be applied individually or a combination of two or more can be used to obtain better results. [16]

Some of the physicochemical techniques are coagulation, flocculation, sedimentation and adsorption on activated surfaces (such as fly ash or membranes). Other methods like photocatalytic removal, ultrafiltration, nanofiltration and reverse osmosis have presented very interesting results, however, imply a high capital investment and require pre-treatment of the effluent. [16] [17]

The electrochemical treatment converts the chloride present in the effluent into chlorate, hypochlorite and chlorine. Although the system is very effective, it presents high operating costs, a result of the high energy consumed in secondary reactions. [18]

Biological methods include the two large groups, aerobic and anaerobic. In aerobic treatment, the biological oxidation is the most widely used technique to remove BOD, by converting the organic compounds completely to CO_2 and H_2O. It was also proved the ability of this process to remove AOX (43-63%). With anaerobic treatment, the results are worst, however when the two methods are applied together or with other techniques, it becomes better. [15]

1.2.2 Advanced oxidation processes

Despite the more conventional methods presented above, none of them is truly effective in the treatment of non-biodegradable effluents with high chemical stability. As such, a possible alternative is the application of advanced oxidation processes, AOP. These allow the complete or partial mineralization of organic compounds to carbon dioxide, water and inorganic compounds, through oxidation reactions. When the full decomposition of non-biodegradable organic pollutants is not possible, it is common to combine a biological process. [16] [17]

The different processes of advanced oxidation are usually divided into two main groups: the homogeneous processes and the heterogeneous processes. Homogeneous processes occur in a single phase and the predominantly reactants used are ozone, hydrogen peroxide and Fenton's reagent, while the heterogeneous processes occur in the presence of two phases, usually a liquid phase and a solid phase, corresponding to the catalyst. AOP include different systems, such as photochemical degradation processes (UV/O_3, UV/H_2O_2), photocatalysis (TiO_2/UV, photo-Fenton) and chemical oxidation processes (O_3, O_3/H_2O_2, H_2O_2/Fe^{2+}), however, the common basis in all of them is the production of $^{\bullet}OH$ radicals. These radicals are very reactive and not very selective, so they can attack most of the organic molecules and promote their degradation. [17]

Despite the above-mentioned potentialities, AOP are processes still in the study phase due to the difficulty of scale-up them to the industry. This difficulty comes from the need in some cases of use an external radiation source, such as UV lamp, which presents some risks to operate and imply higher costs. Among all these processes, it will be given greater relevance to those may have greater influence in the follow-up of this work, namely the Photo-Fenton process and the Heterogeneous Photocatalysis with titanium dioxide, TiO_2.

1.2.3 Photo-Fenton process

In 1894, H. J. Fenton described for the first time the oxidative force of iron ions with hydrogen peroxide in certain organic molecules, which was later explained by the formation of

hydroxyl radicals, according to Equation (1). One of the disadvantages of this process is the production of iron sludge waste that can be minimized using UV or sunlight. The radiation promotes the formation of more radicals, according to Equations (2) and (3), that consequently increases the rate of degradation of the organic compounds. [17] [19] [20]

$$Fe^{2+} + H_2O_2 \rightarrow Fe^{3+} + OH^- + {}^{\bullet}OH \quad (1)$$

$$Fe^{3+} + H_2O \xrightarrow{h\nu} Fe^{2+} + H^+ + {}^{\bullet}OH \quad (2)$$

$$H_2O_2 \xrightarrow{h\nu} 2\ {}^{\bullet}OH \quad (3)$$

There was already performed some studies of AOX removal using this method. For example, a wastewater from a plant of pulp and paper manufacturing was treated with photo-Fenton and the percentage of AOX removal was 93%, which indicates the effectiveness of this treatment. [21]

1.2.4 Heterogeneous photocatalysis

The word "catalysis" was probably used for the first time by A. Libavius in the sixteenth century in his book *Alchymia* and derives from the Greek, meaning decomposition or dissolution. Over the years, several researchers, such as Berzelius and Ostwald, had been improving the definition of this phenomenon and one definition say it is the ability to decrease the activation energy of a reaction and thus increasing its speed. However, there are different mechanisms that depend of the catalyst used and of the reactive system. The term photocatalysis comes from the combination of the prefix photo and the word catalysis and refers to the acceleration of a given chemical reaction by a photocatalyst, which is activated by the radiation. In addition, depending on the stage of the catalyst and of the substrate, the photocatalysis can be homogeneous or heterogeneous. [22]

Heterogeneous photocatalysis had its origin in the 1970s when research began on photo electrochemical cells with the purpose of produce fuels from cheap materials, through the transformation of solar energy. In 1972, Honda and Fujishima used titanium dioxide, TiO_2, irradiated by a photoelectric cell, to oxidize water and generate hydrogen and oxygen. Later, in 1983, the complete degradation of trichlorethylene and chloroform by heterogeneous photocatalysis was demonstrated in dilute aqueous solutions of TiO_2 and these showed the possibility to apply photocatalysis for effluent treatment and water decontamination. Because of that, research around the world has been developed, exploring the potential of this mechanism to destroy non-biodegradable and polluting compounds on water and wastewater. [23] [24] [25] [26]

The principle of heterogeneous photocatalysis involves the activation of a semiconductor by the absorption of photons. The energy difference between the valence band, VB, and the conduction band, CB, is called band-gap energy and the absorption of photons with higher energy than the band-gap results in the promotion of electrons from the valence to the conduction band (e_{CB}^-), with the creation of a positive hole in the valence band (h_{VB}^+), as represented in the Equation (4) and Figure 1. Note that when the photon energy is greater than the band-gap energy, the excess is transformed into thermal energy. [27]

$$TiO_2 \xrightarrow{h\nu} e_{CB}^- + h_{VB}^+ \quad (4)$$

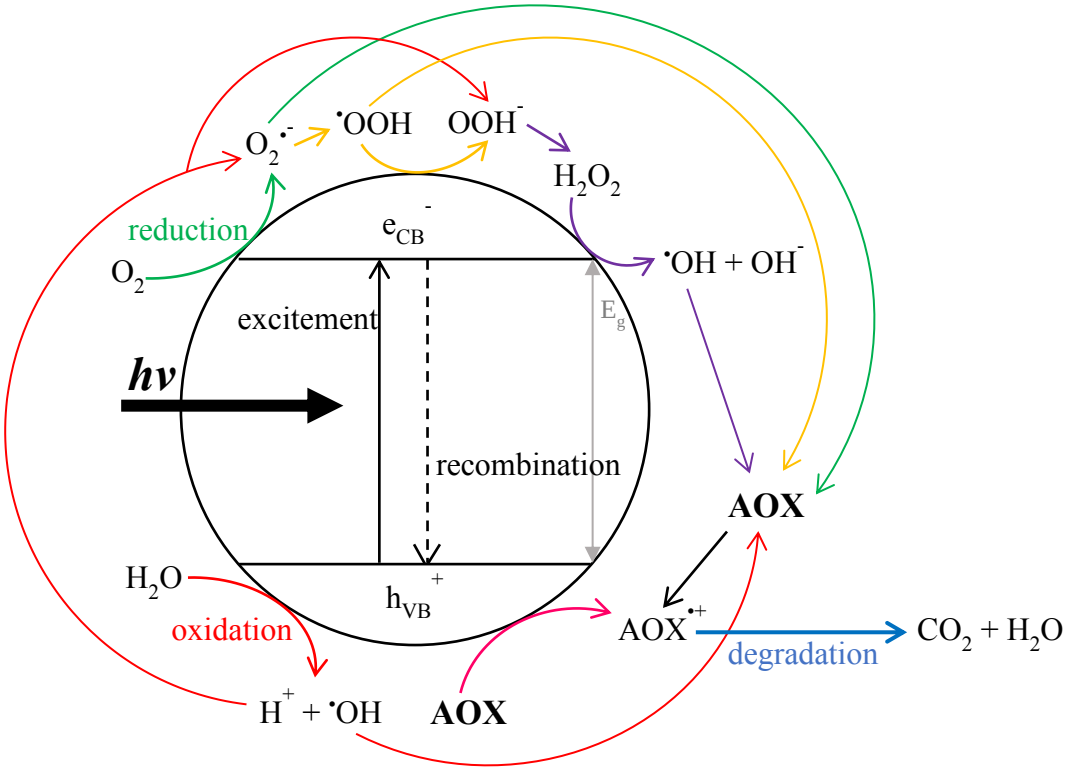

Figure 1 - Scheme of the operation method of a semiconductor on heterogeneous photocatalysis, namely in the degradation of AOX. [28]

The h_{VB}^+ and e_{CB}^- are powerful oxidizing and reducing agents, respectively. The organic compounds, such as AOX, are adsorbed in h_{VB}^+ to be oxidised and degraded into CO_2 and H_2O, Equation (5). The gap formed has also a great potential to generate •OH radicals from water molecules adsorbed on the surface of the semiconductor, Equation (6). [29]

$$AOX_{(ads)} + h_{VB}^+ \rightarrow AOX^{\bullet+} \rightarrow CO_2 + H_2O \quad (5)$$

$$H_2O_{(ads)} + h_{VB}^+ \rightarrow {}^{\bullet}OH + H^+ \quad (6)$$

The electrons at the conduction band can react with O_2 to form an anion radical superoxide, Equation (7). The presence of dissolved oxygen is extremely important during photocatalytic degradation as it can make difficult the recombination process on TiO_2 (e_{CB}^- /h_{VB}^+) and, at same time, can produce more radicals according to the Equations (7) to (11). Note the Equation (11) also demonstrates the advantageous effect of adding hydrogen peroxide, once it increases the radicals formed. Finally, all the radicals formed, R = [$^{\bullet}OH$, $O_2^{\bullet-}$, $^{\bullet}OOH$], can oxidize the organic compounds in the way to degrade them, Equation (12). [24] [29] [28]

$$O_{2\,(ads)} + e_{CB}^- \rightarrow O_2^{\bullet-} \quad (7)$$

$$O_2^{\bullet-} + H^+ \rightarrow {}^{\bullet}OOH \quad (8)$$

$$^{\bullet}OOH + e_{CB}^- \rightarrow OOH^- \quad (9)$$

$$OOH^- + H^+ \rightarrow H_2O_2 \quad (10)$$

$$H_2O_2 + e_{CB}^- \rightarrow {}^{\bullet}OH + OH^- \quad (11)$$

$$AOX + R \rightarrow CO_2 + H_2O \quad (12)$$

This potential to generate radicals may vary according to the type of semiconductor used and the pH value of the medium. For example, the pH value affects the surface of the photocatalysts and consequently influences the adsorption of the organic pollutants on the surface. [30]

The heterogeneous photocatalysis with TiO_2 has been used effectively for the treatment of pulp and paper mill wastewater and promising results have been obtained. For example, Perez et al. reported that photocatalysis can efficiently reduce the concentration of AOX from the ECF process in 80% and when it is added H_2O_2, the percentage of removal can increase to 95%. [31] [32]

1.2.5 Type of photocatalysts

The photocatalysts used in heterogeneous photocatalysis are typically semiconducting materials. There are many semiconductors on the market such as titanium dioxide (TiO_2) cadmium sulphide (CdS) zinc oxide (ZnO) and tungsten trioxide (WO_3) which due to their electronic structure can act as sensitizers in oxidation processes and light-mediated reduction. Different semiconductors have different band gaps energies, which means different reduction potentials. A substrate with a higher positive value of reduction potential is a stronger oxidant than those with a low or negative reduction potential. [27] [33]

A photocatalyst is a material activated by the absorption of a photon and is capable of accelerate a reaction without being consumed. As such, to be considered a good photocatalyst, it

must combine photoactivity and photo stability and not all the materials satisfy these both conditions. Among the semiconductors, TiO_2 is the most studied and used due to its high photocatalytic efficiency, chemical and physical stability, low cost and low toxicity. [24] [34]

1.3 Titanium dioxide

Titanium dioxide, TiO_2, also known as titanium (IV) oxide, can exist in three crystalline forms with different dimensional arrangements and densities, designated as rutile, anatase and brookite minerals (Figure 2). In terms of stability, rutile is the most stable form of TiO_2 and therefore the preferred to use. However, anatase and brookite, which at room temperature are stable, can be converted to rutile, under temperatures higher that 550 °C and 750 °C, respectively. [35] [36]

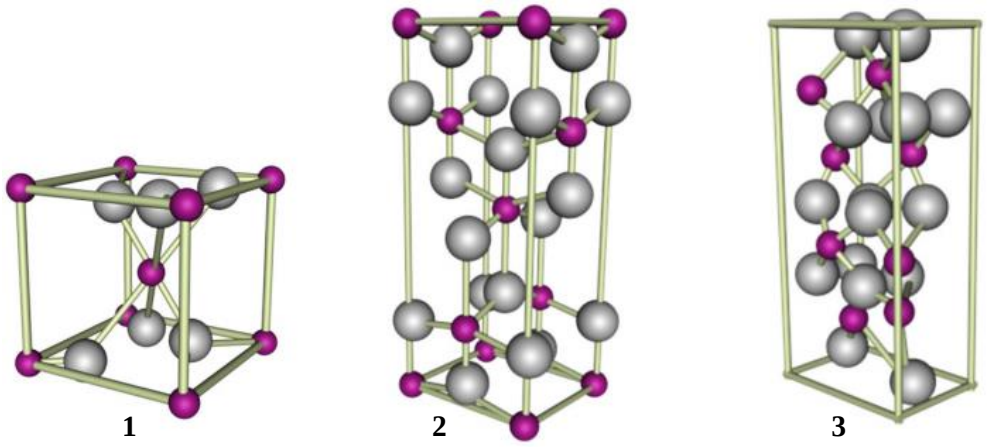

Figure 2 - Base units of rutile (1), anatase (2) and brookite (3) (grey - oxygen and purple - titanium). [35]

1.3.1 Properties and applications

Generally, TiO_2 is a white powder with no characteristic odour, having a molecular mass of 79.9 g/mol and a boiling and melting point of 2750°C and 1855°C, respectively. In terms of safety, it is non-flammable and has a low level of toxicity, but it may cause some irritation in contact with skin and eyes and by inhalation or ingestion. Regarding to nanoparticles of TiO_2, the safety standards to be taken should be the same, but it is important to note that the toxicity of nanoparticles has not been studied in detail and that the effects on human body are not well known yet. [37]

The application of titanium dioxide depends on its properties, which are strongly related to the size of the particles, as shown in Figure 3.

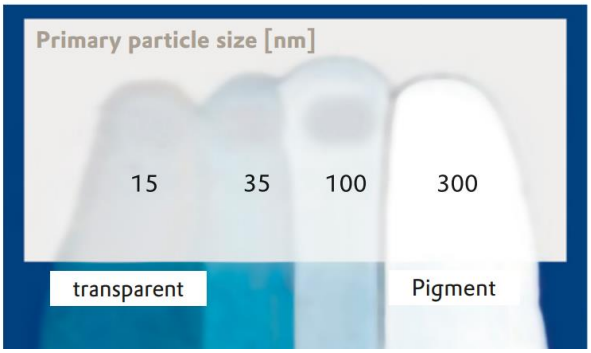

Figure 3 - Influence of the particle size on the transparency/colour of titanium dioxide. [38]

From the view point of the colour, larger particles (200-500 nm) are white and no transparent and are mainly used in pigment, being also known as "Titanium White" or "Pigment White 6". Besides that, titanium dioxide has a high refractive index of 2.70, which gives it the ability to produce a high level of opacity or hiding power, making it a much better pigment than other chemicals such as zinc oxide or porcelain. Although it is considered the best white pigment currently available, its application is not restricted to this colour, because when combined with coloured pigments, it provides them the desired hiding power. [39]

Because all that characteristics, there is a wide variety of applications, as shown in the Figure 4, ranging from pigments for paints and plastics to toothpaste, sunscreens, pharmaceutics, cosmetics and food. The world production of titanium dioxide, which began around the twentieth century, was over $10 billion in 2016 and it is expected to grow 5.8% until 2021. [35] [40]

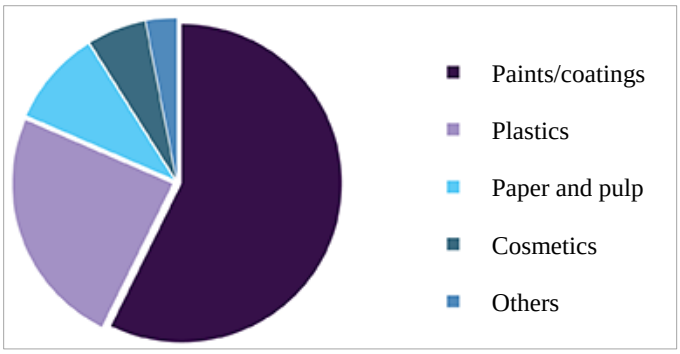

Figure 4 - Global titanium dioxide market revenue by application, data from 2015. [41]

On the other hand, according to the Figure 3, TiO_2 particles with average sizes between 14 and 21 nm, such as those produced by EVONIK, have practically no pigmentation properties and are widely used as catalysts, catalyst carriers and heat stabilizers. These commercial nanoparticles are a fine white powder with high specific surface area (50 ± 5) $m^2 \cdot g^{-1}$ and an anatase content of 80 to 90wt%, with only a small amount of rutile and without any surface treatment. [42] [38]

TiO_2 is a semiconductor sensitive to light, absorbing electromagnetic radiation in the ultraviolet zone. The band gap energy in the solid state is E_g = 3.05 eV for the rutile and E_g = 3.29 eV for the anatase, which corresponds to the absorption band of < 415nm for rutile and < 385nm for anatase, according to the Planck law. Because of the great photocatalytic activity of TiO_2 nanoparticles, these have been studied in several areas, from the treatment of wastewaters and the reduction of NO_x in the exhaust gas, to the production of antibacterial surfaces, automatic cleaning and anti-fogging. [38] [43]

1.3.2 Production of TiO_2

It is possible to extract titanium dioxide from various natural ores, such as rutile, anatase and ilmenite, Figure 5, which have different concentrations of TiO_2 and are extracted in different countries, as shown in Table 1. From an economic point of view, it is only profitable to extract titanium dioxide when it is present in the purest and more concentrated form, whereby rutile and anatase are the most extracted, also associated with its photocatalytic characteristics. [35]

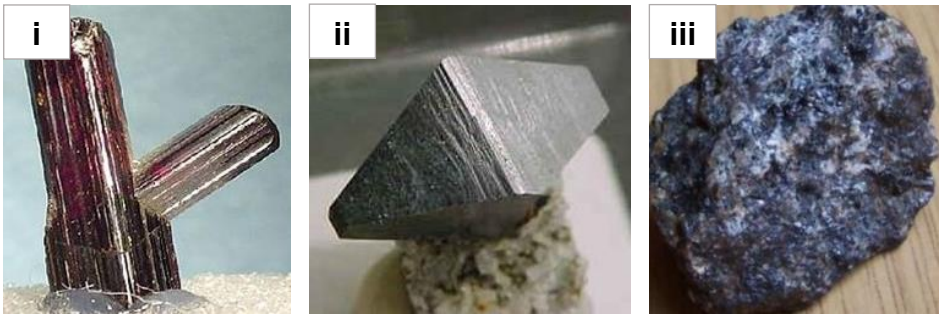

Figure 5 - Ores of rutile (i), anatase (ii) and ilmenite (iii). [44]

Table 1 - TiO_2 percentages and main locations of natural ore deposits. [42]

Ore	% TiO_2	Main locations
Rutile	90-98	Australia
Anatase	30-40	Brazil
Ilmenite	43-61	Norway, Russia, Finland and Canada

After extraction of the titanium ores it is necessary to convert them into titanium dioxide and there are two main industrial processes, the chlorine and the sulphate process. The main differences between them is in the composition of the raw material used. In general, those with higher quality (in terms of percentage of TiO_2) are preferably used in the chlorine process. However, the choice of the raw material also depends on the configuration of the industrial unit, on the environmental, health

and safety requirements and on the total production costs. For example, once all the raw materials have in their composition uranium and thorium (different concentrations in each), it is desirable to use materials with lower concentration of these compounds if the production will be made in large scale.

As mentioned, the chlorine process requires a purer ore and the raw material must contain at least 70% rutile, although this is the rarest form. Rutile can be obtained from an ore, the natural source, or can be produced synthetically. Very briefly, synthetic rutile is obtained by reducing ilmenite iron oxides to metal irons using carbon monoxide. Then a reoxidation and separation of the richest TiO_2 fraction happens, whether in the Becher process, or a leaching with hydrochloric acid is followed if it is the Benelite process. [39]

In the chlorine process, titanium dioxide is reduced in the presence of carbon and oxidized with chlorine, in a fluidized bed reactor, Equations (13) and (14). After, $TiCl_2$ is distilled and converted back to TiO_2 in an oxygen flame or plasma at high temperatures (1200-1700°C), Equation (15). The use of hazardous chemicals and a large amount of energy causes the emission of gaseous particles made this process environmentally and financially unfavourable since the early 1990s. [36] [39]

$$TiO_2 + C \rightarrow Ti + CO_2 \quad (13)$$

$$Ti + 2\ Cl_2 \rightarrow TiCl_4 \quad (14)$$

$$TiCl_4 + O_2 \rightarrow TiO_2 + 2\ Cl_2 \quad (15)$$

In the sulphate process, ilmenite ($FeTiO_3$) is treated with a concentrated solution of sulfuric acid, to selectively extract titanium oxygen sulphate, $TiOSO_4$, according to Equation (16). Then, it is hydrolysed to convert it to hydrated titanium dioxide and subjected at high temperatures (200-300°C) to remove the water, Equations (17) and (18). In terms of the number of operations units involved, it is a much more complex process than the chloride process. [36] [39]

$$FeTiO_3 + 2\ H_2SO_4 \rightarrow FeSO_4 + TiOSO_4 + 2\ H_2O \quad (16)$$

$$TiOSO_4 + (n+1)\ H_2O \rightarrow TiO_2 \cdot nH_2O + H_2SO_4 \quad (17)$$

$$TiO_2 \cdot nH_2O \rightarrow TiO_2 + nH_2O \quad (18)$$

If the purpose is to obtain nanoparticles of titanium dioxide, another method must be applied. These TiO_2 nanoparticles can be obtained by vaporizing pure titanium chloride, $TiCl_4$, at high temperatures (1000-2400°C) and in contact with air and hydrogen. In general, $TiCl_4$ is converted to

TiO_2 at the same time as the hydrogenation gas combines with the chlorine ions to form hydrogen chloride, as in Equation (19). A practical example of this method is the titanium dioxide particles from EVONIK (AEROXIDE® TiO_2 P25). [36] [38]

$$TiCl_4 + 2\ H_2 + O_2 \rightarrow TiO_2 + 4\ HCl \quad (19)$$

1.4 Techniques for the immobilization of TiO_2

The use of TiO_2 powder in photocatalysis, implies the need to add to the process of the effluent treatment a step for catalyst separation and recovery. One possible strategy to avoid this step is to use TiO_2 supported, that allows its recovery and reutilization. Because of this, the feasibility of supporting the photocatalytic active phase in low cost and inert materials is increasingly attractive, due to economic advantages.

Although the mention before, the immobilization of TiO_2 on a support also have disadvantages, once it decreases the surface area of the photocatalyst and its photocatalytic activity, which means a reduction in its performance to remove AOX, comparatively with the performance of TiO_2 no supported.

Support materials should have high adherence and improve the textural properties such as porosity and superficial area. For a material to be considered a good support specifically for TiO_2, it must be transparency to UV light and have a strong chemical and physical bonding with the surface of TiO_2 nanoparticles, without affecting the reactivity of the photocatalyst. Besides that, it should allow to design a reactor that facilitates the mass transfer process and additionally should provide a good adsorption of the organic compounds. [45]

There are several types of supports, which differ in the material used, the technique to produce it and in the method of application. As expected, the performance of each one depends on the target organic compounds desirable to be removed, thus the technique chosen should have this in account.

One of the techniques uses aluminium foils as a support for catalysis, where the nanoparticles of TiO_2 are immobilized on the substract by electrodeposition. Using a novel electrochemical method, TiO_2 films can be deposited on aluminium, by a simultaneous cathodic and electrophoretic deposition of TiO_2 from a stable aqueous suspension, at room temperature. An important parameter that must be controlled is the constant cell voltage, that should be between 2.0 and 4.5V, to provide the better conditions to electrogenerated OH^- in the surrounding of the cathode. This process does

not need thermal post-treatment to impart photocatalytic activity which proves that the TiO_2 nanoparticles are not completely blocked by the matrix created. [46] [47]

Another possibility is the immobilization of the nanoparticles by dip coating in glass raschig rings. Previous studies have shown that this method provides good results for removal of AOX from cyanides, although there is not any comparison with non-immobilized TiO_2, in the same conditions. Furthermore, this method was not tested with pulp mill effluents and owing to the large size of the glass rashing rings, it is not easy to apply in laboratorial reactors. [48]

An alternative method can support the nanoparticles of TiO_2 on nanofibers of silica, by an innovative sol-adhesion method, as presented in the Figure 6. The use of silica allows to keep the particles of TiO_2 small, without agglomeration, and to control the thermal stability of TiO_2. Despite these good advantages, the photocatalytic activity performance will also depend on the compound to be removed and for some compounds TiO_2 non-supported can have a better performance. [49] [50]

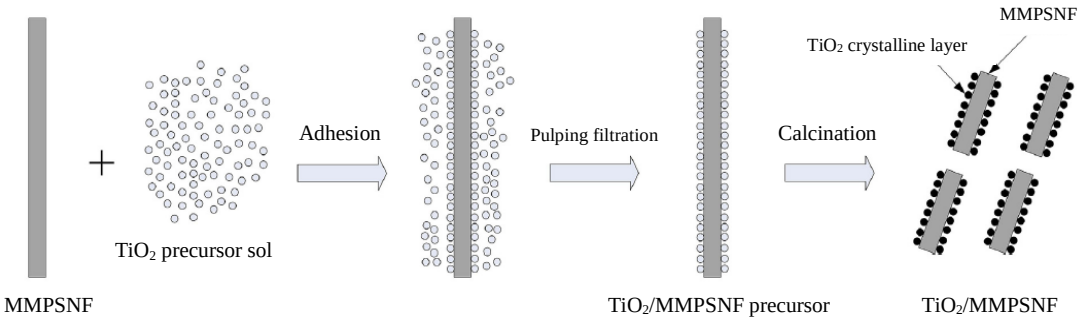

Figure 6 - Process of synthesis TiO_2/micro-meso porous silica nanofibers hybrid photocatalyst, MMPSNF. [50]

Finally, the use of low cost polymers it is another alternative to support TiO_2. The resulting material can be used for several cycles without loss of catalytic activity, which represents an economic advantage. However, the photocatalytic activity of this material compared with TiO_2 P25 non-supported is lower and consequently the quantity of pollutants removed will be lower. [51]

1.4.1 Magnetic nanoparticles

In water treatment processes, an alternative and attractive solution to recover the photocatalyst is the use of magnetic nanophotocatalysts. The biggest advantage of this technique is the easy way to separate the photocatalyst, using an external magnetic field, from the effluent treated. In addition, previous studies have shown that magnetic nanoparticles can be reused and maintain the

good photocatalytic properties, which is important to have a good rate of removal compounds. This method is considered more efficient, economic and environmentally friendly when compared with others and because of that, the number of studies on this topic has grown in the last years. [52]

For example, these magnetic nanophotocatalysts were already tested on Kraft mill effluents. The treatment of organic effluents with nano-TiO_2 and nano-Fe_2O_3 proved the capability to effectively reduce the colour, aromatic compounds, COD and the toxicity of the effluent. [53]

Usually, the magnetic nanophotocatalysts are a composite comprising magnetic and photocatalytic nanomaterials. The magnetic nanomaterials commonly compose the inner core and can be magnetite (Fe_3O_4), maghemite (y-Fe_2O_3) or cobalt ferrite ($CoFe_2O_4$). The photocatalytic materials are usually present in the shell and can be any of the materials described previously, such as TiO_2 and ZnO. Although this represents the most common configuration, other arrangements have been studied, in combination of other supporting materials. For example, some studies focused on the use of a layer of amorphous silica between Fe_3O_4 and TiO_2, which can prevent electron transfer from TiO_2 to Fe_3O_4 and to decrease or eliminate the reductive dissolution of Fe(III). In this way, the photocatalytic activity increased and the magnetic properties are maintained. [54] [55]

For the preparation of these nanomaterials, the most common approach allows to obtain a core@shell configuration and it involves the synthesis of the magnetic core by co-precipitation, microemulsion or sonochemical methods, followed by the adding of the photocatalytic layer, by sol-gel or thermal methods. Besides this method, it is also possible to synthetize the magnetic nanoparticles simultaneously with the adding of the photocatalyst, but the morphology and the organization of the particles will be different. [54] [55]

As shown in Figure 7, after the preparation of the magnetic nanophotocatalysts, they are added to the contaminated solution and the photocatalysis is promoted. After the removal of the pollutants, the magnetic separation can be carried out in a very simple way when compared to the conventional recovery methods, such as sedimentation or centrifugation. It is considered a method more efficient, easier and faster to operate, more selective and not sensitive, because it is suitable for a wide range of working conditions, in terms of pH value and temperature range. Furthermore, several cycles can be performed using the same material and the studies prove that it is possible to reach almost the same level of pollutants removal. However, the photocatalytic performance can decrease in consecutive treatments, as a result of the incomplete recovery of the magnetic nanophotocatalysts and the possible change of their properties, owing to the aggregation of the nanoparticles. [52]

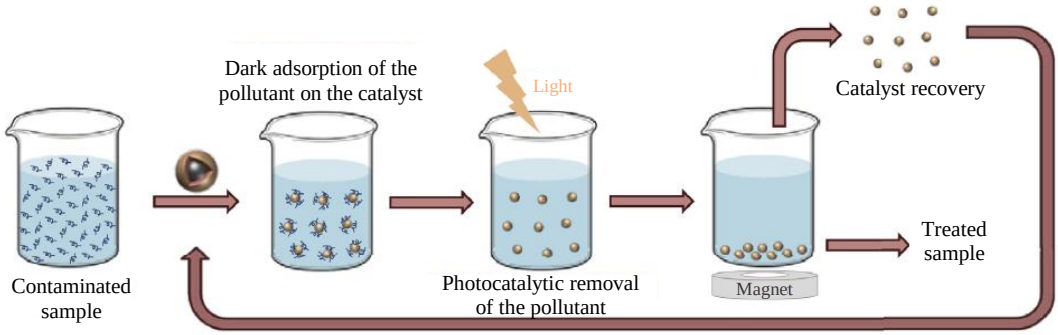

Figure 7 - Scheme of the photocatalytic treatment with magnetic nanophotocatalysts and of the magnetic recovery. [52]

Although these advantages, this method is currently limited to lab scale applications and the challenge nowadays is develop intelligent systems which allows the treatment of large volumes of water and effluents. Some of the most employed filters for magnetic solid separations at industrial scale are the High Gradient Magnetic Separator and the Open Gradient Magnetic Separator, which is schematically represented in Figure 8. [52]

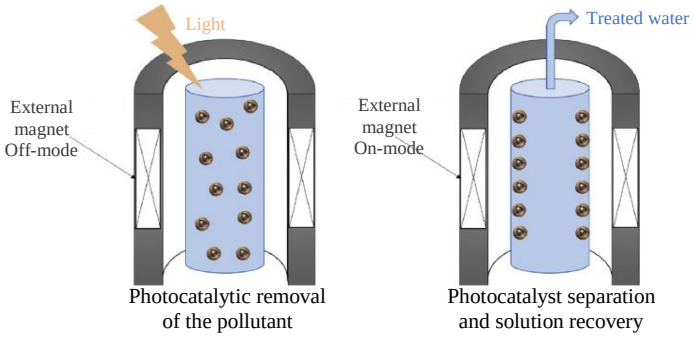

Figure 8 - Proposed Open Gradient Magnetic Separator system for the magnetic nanophotocatalysts separation. [52]

1.4.2 Geopolymer spheres

Besides the examples presented before and according to the idea of circular economy, an alternative way could be the use of geopolymer spheres, prepared with a percentage of ash from the residues of biomass burning of pulp and paper industry. The porous geopolymer spheres were produced through suspension solidification, following a specific procedure. As the purpose of these spheres is to use on photocatalytic experiments, a certain amount of TiO_2 was added while they were being prepared and the colour of the spheres evolve from brown colour to light pink. [56]

2. Materials and Methods

2.1 Materials

The effluent treated in this project is a bleaching stage filtrate of a Kraft pulp mill, denominated D0, and is obtained from the first bleaching stage with chlorine dioxide. The purpose is to oxidize residual lignin still present in the fibers. Among the effluents previously studied in other works, the effluent D0 is the one with the most acidic pH and the highest initial amount of AOX. [57] Note the effluent used is an intermediate of the whole production, however decreasing the amount of AOX in this one, will consequently decrease the AOX concentration in the following streams of the process.

The titanium dioxide used was obtained from Evonik Industries, as AEROXIDE® TiO_2 P25. This material is a white powder and, according to the information provided by the supplier, it is a mixture of anatase and rutile (80:20 wt%), comprising particles with an average diameter of 21 nm. The salts of Fe(II) and Fe(III) $FeCl_2{\cdot}4H_2O$ were obtained from Sigma-Aldrich in form of iron(II) chloride tetrahydrate ($FeCl_2{\cdot}4H_2O$) and iron(III) chloride hexahydrate ($FeCl_3{\cdot}6H_2O$), respectively. The ammonia solution, NH_4OH 25%(w/w) was obtained from LabKem.

For the photocatalytic treatment, the hydrogen peroxide used was an aqueous solution, provided by VWR Chemicals, at a concentration of 30%(w/w). Nitric acid, HNO_3, from Sigma-Aldrich was used to acidify the aliquots of treated effluent prior AOX determination.

2.1.1 Preparation of TiO_2 with magnetic properties

The TiO_2 nanoparticles with magnetic properties were prepared by in situ synthesis of magnetic iron oxides (magnetite, Fe_3O_4) via coprecipitation of iron (II) and (III) cations, performed in presence of TiO_2 P25 particles. The reaction occurs in nitrogen atmosphere and alkaline medium according to the Equation (20).

$$Fe^{2+}_{(aq)} + 2\ Fe^{3+}_{(aq)} + 8\ OH^- \rightarrow Fe_3O_{4(s)} + 4\ H_2O_{(l)} \qquad (20)$$

First, it was necessary to prepare deoxygenated water by adding water milli-Q to a rounded bottom glass flask (500 mL). The water was stirred during two hours by magnetic stirring under a flux of nitrogen. Afterwards, 190 mL of deoxygenated water was transferred to a three-neck round

bottom flask (250 mL) and the TiO_2, previously weighted according to the values on Table 2, was dispersed, with ultrasonic irradiation for 30 minutes and at room temperature. Then, 4.43 g of $FeCl_3.6H_2O$ and 1.625 g of $FeCl_2.4H_2O$ were dissolved in the mixture and 10 mL of NH_4OH were added to the solution and stirred for 10 minutes. The final mixture had a black coloration.

Table 2 - Amount of TiO_2 necessary for the preparation of Fe_3O_4/TiO_2 nanoparticles.

Fe_3O_4/TiO_2	**(1:1)**	**(1:2)**	**(1:3)**
m TiO_2 (g)	0.345	0.690	1.035

After the synthesis, the obtained magnetic nanoparticles were magnetically separated from unreacted reactants and washed with water milli-Q (4 times) followed by absolute ethanol (2 times) and then dried in an incubator at 40°C for 48 hours. In order to improve the results obtained for Fe_3O_4/TiO_2 (1:3) and to reduce the amount of free magnetite in this sample, some of these nanoparticles were centrifuged for 20 min at 2000 rpm, before dried in the incubator, (cfg).

Using the procedure described before, it was also prepared bare magnetite, Fe_3O_4, without the addition of TiO_2 to the deoxygenated water.

2.1.2 Preparation of geopolymer spheres

The geopolymer spheres were prepared in the Department of Materials and Ceramics Engineering of the University of Aveiro, by a specific procedure, which include a step of add TiO_2 to the original spheres prepared with wastes from past and paper industry. The use of this spheres represents a strategy of circular economy, once the wastes of the industry will be used as a raw material for the treatment of the effluents of the same industry. [56]

2.2 Instrumentation

2.2.1 X-Ray powder diffraction

The X-ray diffractograms of the nanoparticles were obtained from X-ray diffractometer Rigaku Geigerflex Dmax-C, equipped with a source of monochromatic radiation Cu-Kα.

2.2.2 Spectroscopy

Fourier Transform Infrared Spectroscopy

The infrared spectra of the materials were acquired in the solid state and recorded in a spectrometer Mattson 7000 at 4 cm^{-1} resolution, using a horizontal attenuated total reflectance (ATR) cell. There were collected 1897 scans, between wavenumbers of 349 and 3998 cm^{-1}.

Ultraviolet-visible Spectroscopy

The samples were dispersed in ethanol and analysed in the UV-Visible Spectrometer Cintra 303, from GBC Scientific Equipment, Ltd..

2.2.3 Microscopy

Transmission Electron Microscopy

First it was necessary to prepare the samples to analyse and for that a small amount of the nanoparticles was dispersed in absolute ethanol using an ultrasonic bath. Then, one drop of that solution was deposited on a copper grid with amorphous carbon film and the solvent was left to evaporate at room temperature. Then, it was dried at room temperature for 4 hours and stored inside of an eppendorf, in a vacuum chamber.

The morphology of the nanoparticles was characterized by transmission electron microscopy (TEM) using a HR-(EF)TEM JEOL 2200FS operating at 200 kV. In addition, there was used the Micro-Analysis System by Energy Dispersion X-Ray Spectrometry, Oxford Inca Energy TEM 250.

Scanning Electron Microscopy

For the preparation of the sample, a geopolymer sphere was fixed in a carbon tape, using a glue of carbon, Plano GmbH D-35578 Wetzlar, and dried in an incubator at 40 °C, for 24 hours. After this time, carbon deposition was carried out in a Turbo Evaporator, model Emitech K950X.

Scanning electron microscopy (SEM) was performed using a Hitachi SU-70 instrument operated at an accelerating voltage of 15 kV.

Optical Microscopy

The geopolymer spheres were observed in a inverted microscope Axiovert 40MAT, from Carl Zeiss.

2.3 Photocatalysis

2.3.1 Photoreactor

For the photocatalysis tests, the heating bath, Figure 9-1, provides the water that circulates on the photoreactor, Figure 9-2. To keep the magnetic nanoparticles in suspension in the effluent during the treatment, a flux of compressed air was bubbled in the solution, Figure 9-3. Photocatalytic tests were carried out using a UV lamp as radiation source, Figure 9-5, and due to the danger of use this type of light, the photoreactor had an external protection of aluminium, Figure 9-4.

Figure 9 - Experimental Set-up used on the photocatalysis treatment: heating bath (1), photoreactor (2), compressed air flux (3), protection of light (4) and UV lamp (5).

This photoreactor is a borosilicate glass jacketed reactor (maximum capacity of 200 mL), Figure 10-1, with a photochemical quartz immersion well (Ace Glass Incorporated), Figure 10-2. In the reactor is added the effluent to be treated, where fit the quartz immersion well, which is a double-walled with inlet and outlet tubes for water circulation, to keep the desired temperature of the effluent. In the inlet of the immersion well is added the radiation source, a UV lamp (SUPRATEC HTC 150-211 UV lamp, supplied by Osram) with a power of 22 W for UVA wavelength (315-400nm) and 6 W for UVB wavelength (280-315nm), nominal wattage 150W, nominal current of 1.5 A and voltage of 230 V, Figure 10-3.

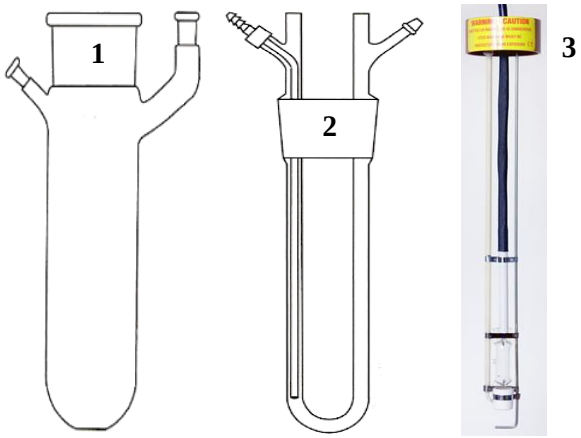

Figure 10 - Scheme of the photochemical reactor: Standard flask (1), immersion well (2) and of the UV lamp (3). [58]

2.3.2 Procedure of the photocatalysis

a) With non-magnetic photocatalysts

The effluent was stored in the refrigerator at 5 °C and before starting the photocatalytic treatment around 250 mL of the effluent was kept in an oven at 60 °C for 1 hour, in the way to reach the same temperature as the working temperature in the photoreactor, interval 57 - 60 °C. Then, two samples were taken, one of 30 mL to measure the concentration of AOX (sample 1) and another of 15 mL to measure the pH value in the initial effluent. After, 0.200 g of TiO_2 was added to 200 mL of effluent, first dispersed for a few seconds using ultrasonic bath and then for 30 minutes with a magnetic stirrer, inside the incubator at 60 °C in the dark.

During the previous preparation, the Set point of the temperature of the thermostatic bath of the photoreactor was turned on to 52 °C and when the temperature stabilized, the solution effluent/catalyst was added to the photoreactor. With absence of light and a magnetic stirrer, it was added 1 mL of H_2O_2 and after 1-2 minutes, two samples of 15 mL were taken from the inside of the photoreactor (sample 2). After, the UV light was turned on and started the time period of photocatalysis treatment. Note that when the photocatalysts were the geopolymer spheres, these do not need any previous mixing with the effluent and 2.0g of spheres were added in the photoreactor.

The test run for 60 minutes and at each 10 minute the temperature was monitored in way to control if it is in the interval 57-60 °C and when not, the temperature of the heating bath was adjusted. In the end, the UV light was turned off and another two samples of 15 mL were taken to evaluate the effect of the photocatalysis treatment on the AOX concentration (sample 3) and the final pH value.

b) With magnetic photocatalysts

When magnetic nanoparticles were used, an alternative procedure was needed, because it was not possible to use magnetic stirrer. In general, the main protocol was maintained with some changes in the stirring method.

In the preparation of the mixture effluent-photocatalyst, a small amount of the effluent was added to the magnetic nanoparticles (0.200 g) and it was dispersed for a few seconds in an ultrasonic bath. Then it was added to the rest of the effluent and it was subjected to the ultrasonic bath again, for 15 minutes, with a protection on the top. In the photoreactor, the dispersion of the magnetic nanoparticles was achieved with a flux of compressed air bubbling in the solution.

2.3.3 Storage of the effluent samples prior to analyse

In the tests performed with non-magnetic photocatalysts, the two aliquots of 15 mL taken from the photoreactor were centrifuged at 600 rpm for 30 minutes, with the aim of separate the TiO_2 from the effluent. Then, with a pipette the supernatant was transferred to plastic tubes. Nitric acid (1 mL HNO_3 1 M was added to the supernatant (30 mL) and all the samples were conserved in the refrigerator (5 ℃) until be analysed.

While, in the tests where magnetic nanophotocatalysts were used, instead of use the centrifuge to separate the nanoparticles, a magnet was placed in the bottom of the aliquots. In this way, the magnetic nanoparticles stay in the bottom and the supernatant could be transferred to the plastic tube and conserved, as explained before.

2.3.4 Recovery of the photocatalysts

After the magnetic separation of the nanoparticles from the effluent, they were washed four times with milli-Q water and two times with absolute ethanol. Finally, the magnetic nanoparticles were dried for 48 hours on an incubator at 40 °C and then crushed on a mortar. In the case of using the geopolymer spheres as photocatalysts, these were separated from the effluent, cleaned two times with milli-Q water and dried.

2.3.5 Determination of AOX concentration

The method to determine the concentration of AOX on the samples was based on the norm ISO 9562:2004. [59]

It started with the dilution of the sample in two steps. First, 5 mL of the sample were dissolved on 50 mL of milli-Q water and second, 2 mL of the last solution were dissolved on 100 mL of milli-Q water. In this way, we obtained a dilution factor of 500. After homogenizing the solution, 100 mL were transferred to an erlenmeyer of 250 mL and it was also prepared an erlenmeyer of 250 mL with 100 mL of HNO_3 (0.2 mol/L), which was the blank test. Then, it was added 5 mL of $NaNO_3$ (0.2 mol/L) and 50 mg of activated charcoal to each erlenmeyer and let the organic compounds be adsorbed on activated charcoal for 1 hour, in a shaking stirrer. After that time, the solution was submitted to pressure filtration and washed with 25 mL of $NaNO_3$ (0.01 mol/L).

The AOX analysis started with the turn on of the equipment Analytikjena multi X 2500, Figure 11. There was added the electrolyte and the temperature of the furnace was increased to 1050°C. After, the filtrate was transferred to the quartz boat which take it automatically to the furnace and the measurement started. The charcoal was incinerated under an oxygen atmosphere in a quartz tube, which is connected to a cell for microcoulometric titration, Figure 11-2.

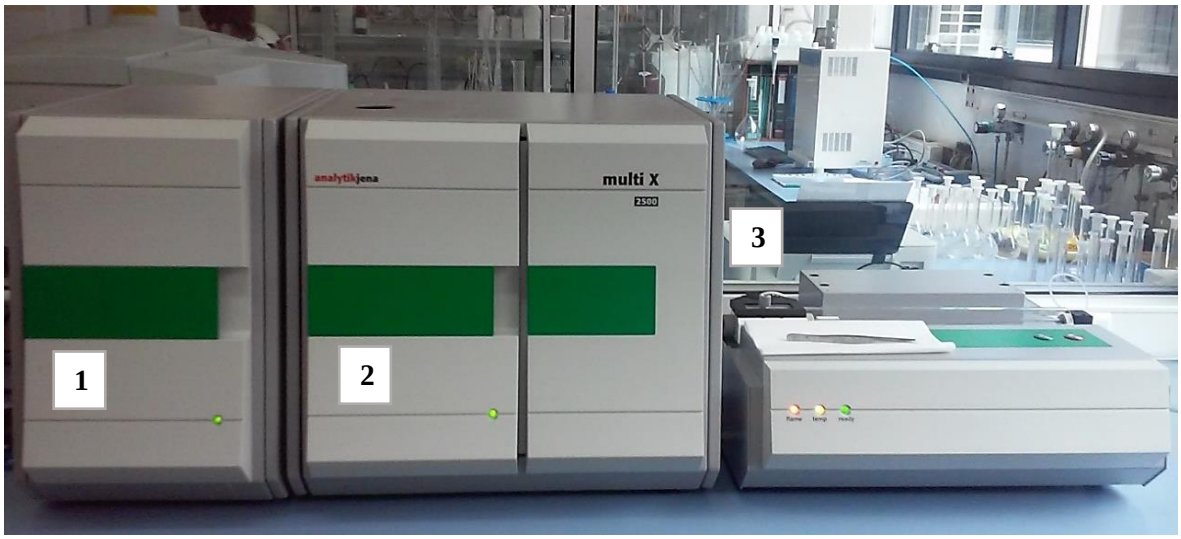

Figure 11 - Analytikjena multi X 2500: electrode location (1), combustion furnace (2) and quartz boat (3).

The value indicated by the microcoulometer corresponds to a charge expressed in microcoulomb units, a value from which the concentration of AOX was calculated. The software of the equipment returned the mass of Cl in the sample, ρ_{sample}, and in the blank test, ρ_{blanck}, this one should not be upper than 30 µg. The determination of the final value of AOX concentration, [AOX], needed to take also in account the dilution factor, f_d = 500, Equation (21).

$$[AOX] = (\rho_{sample} - \rho_{blank}) \times f_d \quad (21)$$

3. Results and Discussion

3.1 Characterization of the effluent

The effluent used on the tests of photocatalysis was taken from a bleaching stage where chlorine dioxide is used and therefore it contains a high concentration of AOX. The effluent was collected in March 2018 and its average AOX concentration was 114 $mg_{Cl}·L^{-1}$.

3.2 Characterization of the photocatalysts

3.2.1 Magnetic nanoparticles and TiO_2

The nanoparticles of Fe_3O_4/TiO_2, Fe_3O_4 and TiO_2 were analysed and characterized using four different experimental techniques: power X-ray Diffraction (XRD), Fourier-Transform Infrared Spectroscopy (FTIR), Ultraviolet-visible Spectroscopy (UV-vis) and Transmission Electron Microscopy (TEM). These techniques allow the identification of the chemical composition of the materials, to visualize the size and shape of the particles, to distinguish the main crystalline phases presented in each material and determine the region of maximum absorption of light.

The magnetic nanoparticles prepared are shown in the Figure 12 and all of them are a black powder, except for Fe_3O_4/TiO_2 (1:3) centrifuged that presents a clearer colour, dark brown, probably due to the higher content of titanium dioxide on the sample.

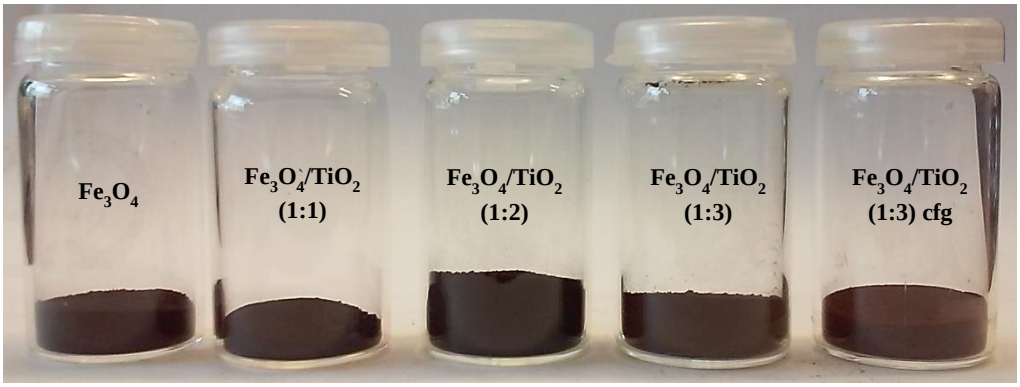

Figure 12 - Photography of the magnetic nanoparticles prepared.[8]

a) <u>X-Ray powder diffraction</u>

The X-Ray Diffraction was used to evaluate the composition of the nanoparticles in terms of crystalline phases. This technique can be used to determine the crystalline structure of the material.

The atoms of the crystalline structure cause the diffraction of a beam of incident X-rays to diffract into many specific directions, which result in a pattern of intensities, called a diffractogram. [60]

This experimental technique was applied to all the nanoparticles prepared and to TiO_2 P25. The diffractograms are shown in the Figure 13 and the Miller indices of the main crystalline phases were identified. [61] [62] [63]

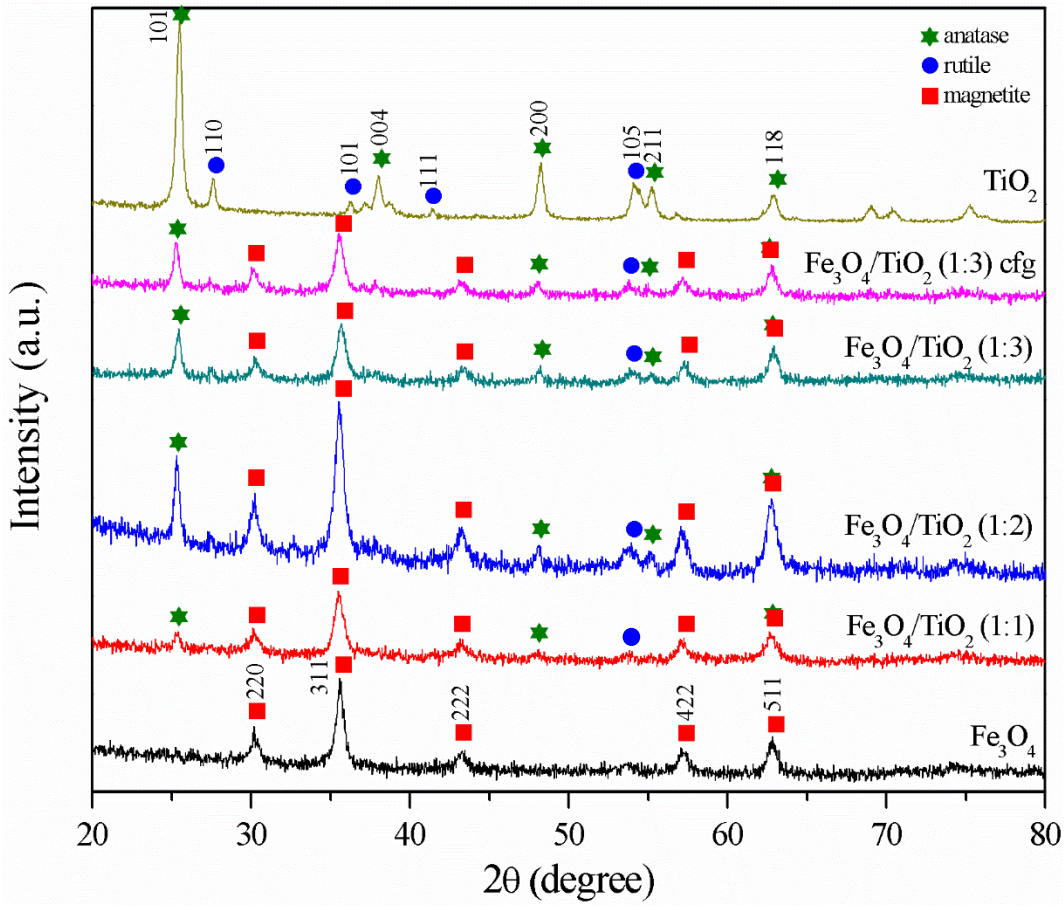

Figure 13 – XFR diffractogram of the nanoparticles prepared and TiO_2 P25.

Analysing the peaks of the diffractograms of the Fe_3O_4/TiO_2 nanoparticles, it is possible to conclude that all of them contain anatase, rutile and magnetite crystalline phases in their composition, because the characteristics peaks of each crystalline phase could be identified in the diffractogram. Since the intensity of the peaks depends on the crystalline phase, it is not possible to predict the composition of the magnetic nanoparticles prepared quantitively.

As referred in the methods section, some of the magnetic nanoparticles Fe_3O_4/TiO_2 (1:3) were centrifuged with the purpose to remove the Fe_3O_4 particles that were not coupled to the TiO_2. The resulting nanoparticles were also analysed by XRD and the diffractogram obtained was similar

to the sample prior centrifugation, which suggests that the step of centrifugation did not induce significant changes in the composition of the sample.

The software of XRD also allows to estimate the weight percentages of each crystal phase, by a Rietveld analysis, and the results obtained are registered on the Table 3. Note that all the weight percentages present on the Table are relative, since it was assessed just the presence of the three crystalline phases (magnetite, anatase and rutile) and possible amorphous components cannot be detected using this technique.

Table 3 - Weight percentages of each component present on the nanoparticles prepared and on TiO_2 P25, assessed by XRD.

		% magnetite (Fe_3O_4)	% anatase (TiO_2)	% rutile (TiO_2)
Fe_3O_4		100	0	0
Fe_3O_4/TiO_2	**(1:1)**	86.1	12.1	1.9
	(1:2)	66.5	23.1	10.4
	(1:3)	66.3	29.4	4.3
	(1:3) cfg	56.5	30.9	12.6
TiO_2 P25		0	83.8	16.2

An estimation of the composition of TiO_2 P25 indicates that the sample comprises around 80/20 wt.% of anatase/rutile, which is in agreement with the supplier information.

It should be emphasized that all the magnetic nanoparticles prepared were washed and separated magnetically, prior to the characterization. Thus, from the results obtained we can conclude that the method of synthesis allows to prepare TiO_2 with magnetic properties and that the content of TiO_2 in the final material can be enhanced by increasing the TiO_2 concentration in the synthesis. According to the XRD data, the highest TiO_2 (anatase and rutile) content was 43.5 wt% and was achieved in the sample Fe_3O_4/TiO_2 (1:3) centrifuged. The content in magnetite was still high (56.5 wt%) but because magnetic separation was used, it is possible that the sample contains also magnetite nanoparticles that are not bonded to TiO_2 particles, even after the step of centrifugation.

The sample (1:3) without centrifugation presented a TiO_2 content slightly lower (9.8 wt% less), which indicates that the step of centrifugation was helpful in the removal of free magnetite. Nevertheless, the conditions of centrifugation (rotation speed and centrifugation time) should be optimized in order to further decrease the content in free magnetite.

Ideally, it would be preferable that a larger amount of titanium dioxide particles would be present in the prepared sample, for photocatalytic applications. However, the presence of magnetite might be also positive, since iron oxide particles can also play a role in photooxidation processes, such as by the photo-Fenton process. [17] [19] [20]

b) Fourier-Transform Infrared Spectroscopy

Fourier-transform infrared spectroscopy is a technique used with solids, liquids and gases and allows to obtain an infrared spectrum of absorption of the sample analysed. Each chemical bond requires a certain energy to vibrate according specific modes and consequently present vibrational bands at specific wavenumber. The analysis of the bands (wavenumber, relative intensity) of the infrared spectrum, returns information about the main components presented on the sample. Likewise, it is possible to prove the presence of same components in a sample, by comparing its spectrum with the spectrum of that desired components. [64]

The Figure 14 shows the FTIR spectra of all the nanoparticles prepared, Fe_3O_4/TiO_2 and Fe_3O_4, and of the TiO_2 P25. In the Table 4, the characteristics bonds corresponding to vibrational bands at different wavenumbers were assigned, based on values that were taken from previous works of Fe_3O_4, and TiO_2.

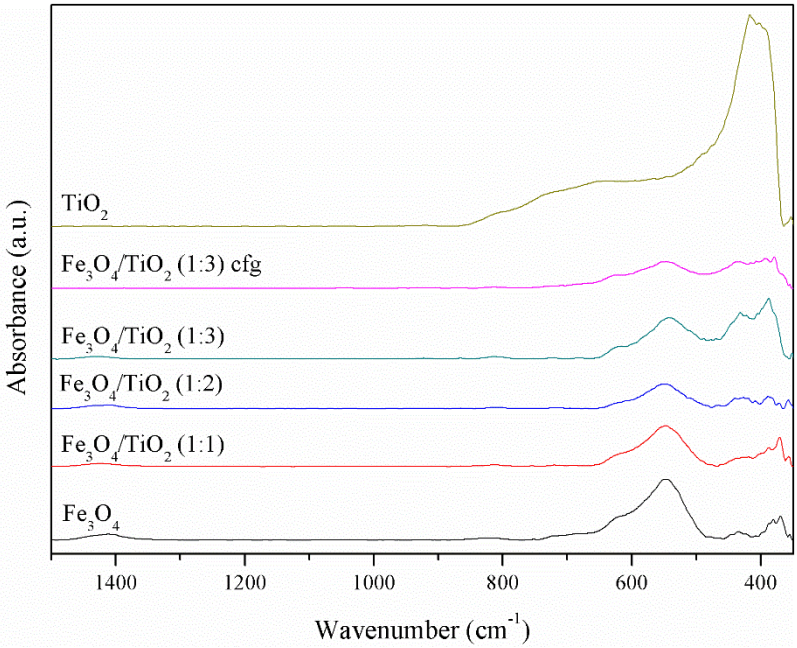

Figure 14 - FTIR spectra of the nanoparticles prepared and TiO_2 P25.

Table 4 - Characteristic wavenumbers of stretching vibrations (ν) and bending vibration (δ).

	Wavenumber (cm^{-1})	Ref
ν (Fe-O)	550	[65]
ν (Ti-O-Ti)	435-535	[66]

The band in the region of 550 cm^{-1} is related to the stretching vibration of the bond Fe-O and looking to the spectrum of Fe_3O_4/TiO_2 (1:1), Fe_3O_4/TiO_2 (1:2) and Fe_3O_4/TiO_2 (1:3), it is possible to see a peak in that region. Therefore, it is concluded that the bond Fe-O is present in all the magnetic

nanoparticles prepared. When the bond Ti-O is present on the sample, the spectrum of FTIR exhibits a band on the region of 435-535 cm^{-1}. Analysing the spectra of the Fe_3O_4/TiO_2 nanoparticles, we can conclude that all the nanoparticles prepared show one band in that region, which is in agreement with the presence of TiO_2. In terms of the Fe_3O_4/TiO_2 (1:3) centrifuged, the spectrum obtained is similar to the Fe_3O_4/TiO_2 (1:3) non-centrifuged, as expected, once the components did not change, just the percentage of each compound on the sample.

c) Ultraviolet-visible Spectroscopy

The ultraviolet-visible spectroscopy is based on the absorption of energy in the form of ultraviolet or visible light by molecules containing π-electrons or non-bonding electrons (n-electrons) to excite these electrons to anti-bonding molecular orbitals of higher energy. Usually, this technique is used in analytical chemistry to determine the compounds present on the sample, but in this work, it was used to check if the photocatalysts prepared absorbed in the region of the UV light. The results are shown in the Figure 15. [67]

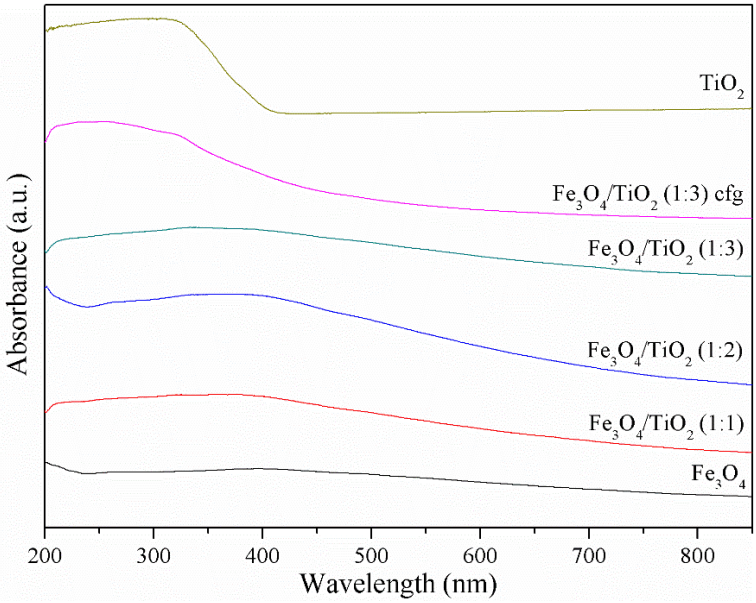

Figure 15 - UV-vis spectra of the nanoparticles prepared and TiO_2 P25.

The TiO_2 absorbs at wavelengths below 400 nm in the UV-Vis region and displays a maximum absorption at 310 nm. The Fe_3O4 absorbs in the UV and visible region, from 800 to 300 nm, with a maximum at 395 nm (Figure 15 and Figure A. 1). All the samples absorb in the range of UVA (315-400 nm) that is the emission range of the UV-lamp. Thus, is it expected a better efficiency on AOX degradation by photocatalysis in the tests performed with UV light, comparing with the tests performed in the dark, without radiation.

d) Transmission Electron Microscopy

A study of transmission electron microscopy was carried out to verify the size and shape of the nanoparticles. In this microscopy technique a beam of electrons is transmitted across the sample to form an image. The sample needs to be an ultra-thin section or a dispersed powder from a suspension and the image obtained is enlarged and focused on an imaging device. [68]

The TEM technique can help to confirm if the information provided by the supplier of TiO_2 P25 corresponds to the characteristics of the product received and to have an idea about the morphology of the particles in order to easily distinguish them from the magnetic iron oxide nanoparticles. In addition, TEM can be helpful to understand if the magnetic nanoparticles and TiO_2 are connected to each other. The Figure 16 shows the TEM imagens of TiO_2 P25 and the magnetic nanoparticles prepared.

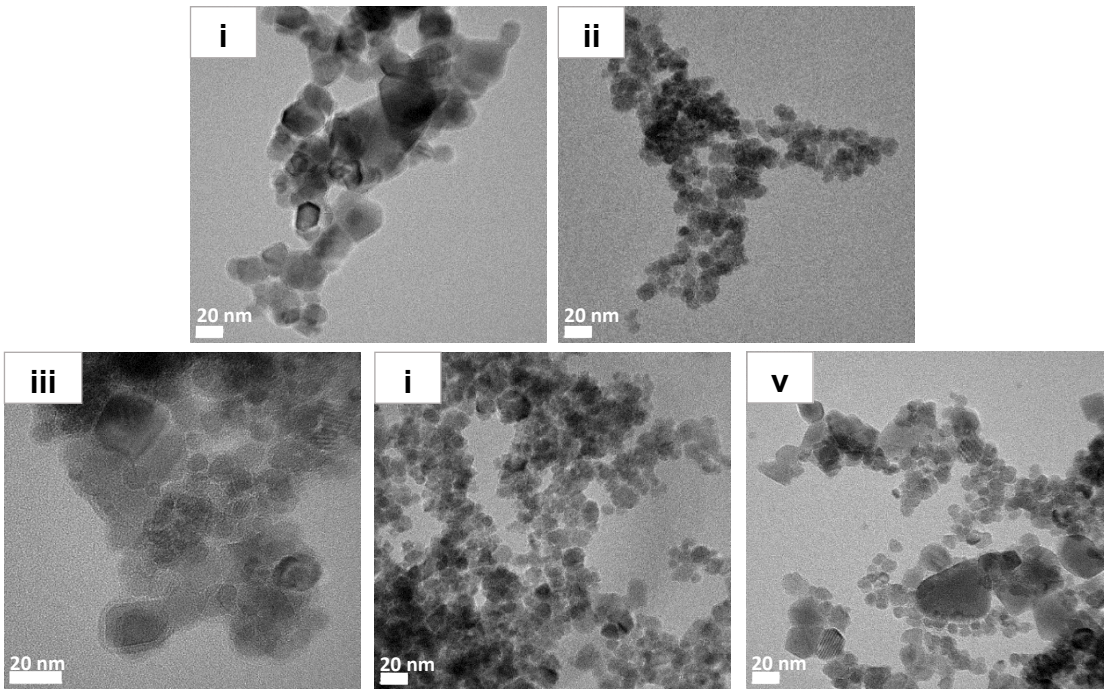

Figure 16 - Images of TEM of TiO_2 (i), Fe_3O_4 (ii), Fe_3O_4/TiO_2 (1:1) (iii), Fe_3O_4/TiO_2 (1:2) (iv) and Fe_3O_4/TiO_2 (1:3) (v).

Analysing the previous images, it is possible to see that P25 particles present irregular shape (rectangular or square) with an average size of [23.6 ± 8.9] nm, image (i). The magnetite nanoparticles are spheroidal and smaller with an average size of [11.8 ± 2.5] nm, image (ii). In the TEM images of the samples Fe_3O_4/TiO_2 it is possible to identify both types of particles. The smallest and spheroidal are ascribed to Fe_3O_4 and the largest and with irregular shape to TiO_2.

Beyond that, no marked differences could be observed among the magnetic nanoparticles prepared with different content of titanium dioxide. No core@shell type particles have been observed

meaning the magnetite is not coating the titanium dioxide. The titanium dioxide nanoparticles are non-homogeneously distributed in the sample.

In the way to confirm the assignment of the particles in the samples of Fe_3O_4/TiO_2, it was carried out an analysis of EDS (Energy Dispersive X-ray Spectroscopy) mapping. This chemical analysis is performed in conjunction with TEM and allows to identify the chemical elements that are present in the sample. The EDS mapping was performed just for the sample Fe_3O_4/TiO_2 (1:3) and the images obtained are shown the Figure 17.

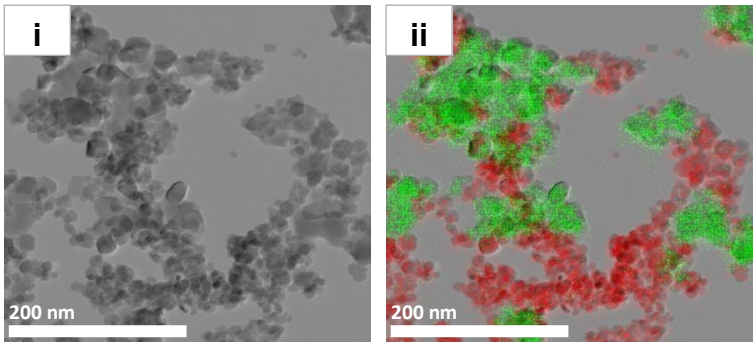

Figure 17 - Images of TEM (i) and TEM with EDS mapping (ii) of the sample Fe_3O_4 /TiO_2 (1:3) (green - titanium and red – iron).

The particles containing titanium and iron, i.e. TiO_2 and Fe_3O_4 particles, appear highlighted with green and red colour, respectively. The results confirm that the sample comprises a mixture of larger and irregular-shaped particles of TiO_2 (green) and smaller and spheroidal nanoparticles of Fe_3O_4 (red) both forming aggregates and with heterogeneous distribution along the sample.

Besides the images presented before, the EDS analysis also returns a spectrum with the peaks that are characteristic of the chemical elements present in the sample, Figure A. 2. The most intense peaks correspond to titanium and iron and, qualitatively, these two elements may be the two most abundant in the sample, even there is also other elements, such as oxygen, associated with the titanium. But, note this analysis was made just for the particles present on the Figure 17 and due to the heterogeneous dispersion of the particles in the sample, this spectrum might not be representative of the all sample. Probably, if EDS analysis was made in other segment of the sample, the intensity of the peaks of each chemical element could be different. Because of this, it is not possible to conclude about reliable weight percentages of each chemical element in the sample, by this method.

3.2.2 Geopolymer spheres

The geopolymer spheres were analysed and characterized using four different experimental techniques: XRD, FTIR, UV-vis and Scanning Electron Microscopy (SEM). The spheres were light pink with an average size of 3 mm and presenting one large pore, as shown in the Figure 18.

Figure 18 - Photography of the geopolymer spheres.

a) X-ray powder diffraction

The geopolymer spheres were analysed by X-ray diffraction to identify the crystalline phases present and to obtain information about the composition of the spheres. The analysis of the diffractogram obtained was made taking as reference the composition of the porous spheres prepared without titanium dioxide. [56] In the Figure 19 is represented the diffractogram of the spheres, with the characteristic diffraction peaks of each component. [61] [62] [69] [70] [71] [72]

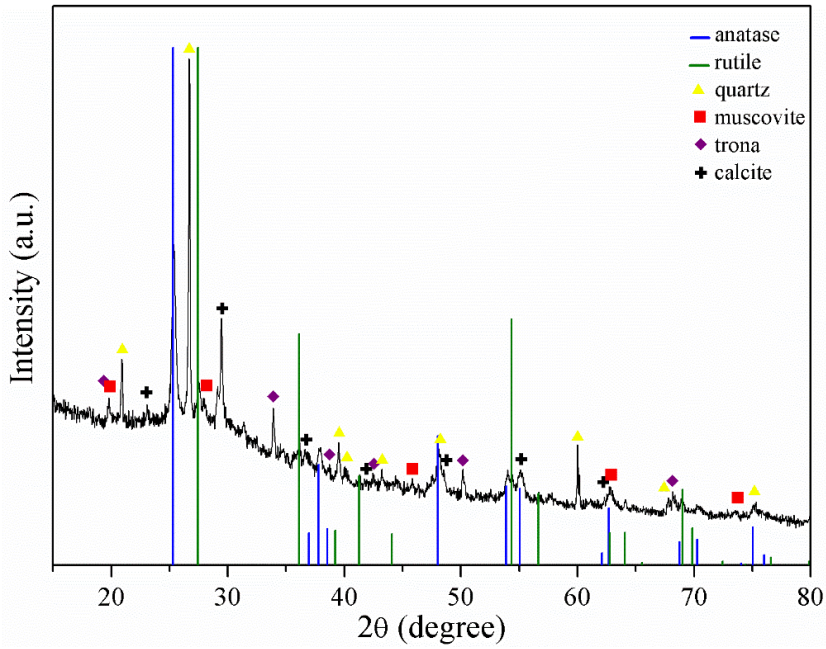

Figure 19 – XRD diffractogram of the geopolymer spheres.

The analysis of the diffractogram indicates the presence of anatase and rutile on the spheres, which means that the geopolymer spheres have in their composition TiO_2, as desired. Overall, the spheres are composed of titanium dioxide, anatase and rutile, and of minerals, such as quartz, muscovite, calcite and trona. Probably there are other components in the spheres, but due to the small expression of them in the diffractogram, they are not going to be consider further.

In the way to know the percentages of each component, there was performed a Rietveld estimation to determine the relative weight percentages of the components present on the porous spheres, as presented on the Figure 20.

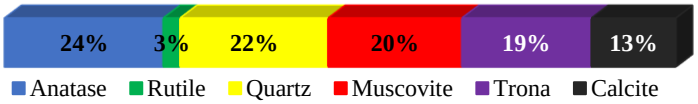

Figure 20 - Weight percentages of each component present on the geopolymer spheres, assessed by XRD.

Anatase and quartz are the components present in higher percentage in the geopolymer spheres, followed by muscovite and trona (carbonated mineral). This high percentage of titanium dioxide (anatase and rutile crystalline phases) is important to the photocatalytic tests, because TiO_2 can induce the production of radicals $^{\bullet}OH$ and consequently promote the photodegradation of the AOX in the effluent. It is admitted that the other components should not have any relevant impact in the removal of AOX by photodegradation, but because of the contact with the effluent, the spheres can suffer some changes morphological and chemically.

b) Fourier-Transform Infrared Spectroscopy

The geopolymer spheres were analysed by FTIR and the respective spectrum is shown in the Figure 21. Using the information summarized on the Table 5 it is possible to identify the main chemical bonds in the spheres.

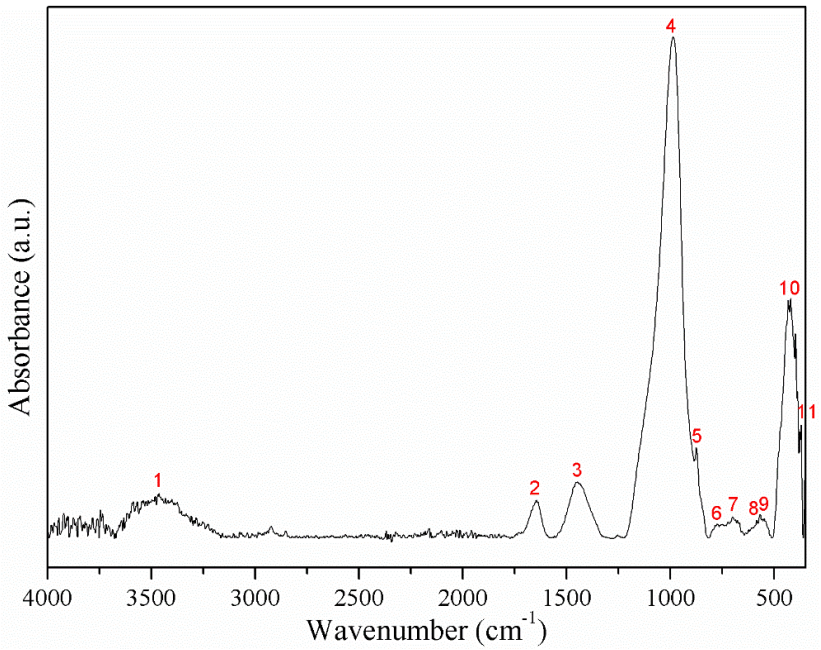

Figure 21 - FTIR spectrum of the geopolymer spheres.

Table 5 - Characteristic wavenumbers of stretching vibrations (ν) and bending vibration (δ).

	Wavenumber (cm^{-1})	Ref
ν (Ti-O-Ti)	435-535	[66]
ν (C-O)	1453	[73]
δ (C-O)	873	
ν (Al-O)	459, 595 and 656 (octahedral structure) 715 (tetrahedral structure)	[74]
δ (Al-O)	1072	
ν (Si-O)	794	[75]
ν (O-H)	3444	
δ (O-H)	1639	

In the Figure 21, the peaks 1 (3458 cm^{-1}) and 2 (1644 cm^{-1}) are ascribed to the stretching and bending vibration of the bond O-H, respectively, due to the presence of residual water in the spheres, but also to OH groups present in the minerals which compose the spheres.

The strong band centred around 1453 cm^{-1} (peak 3) it is characteristic of the C–O stretching mode of carbonate together with a narrow band around 872 cm^{-1} (peak 5) of the bending mode. These peaks are related with the presence of calcite in the spheres.

Besides the calcite, the main bonds of the other minerals present in the spheres are Si-O and Al-O. Metal alkoxides of Si(IV) are reported to show absorption bands attributed to stretching modes around 794 cm^{-1} and the peak 6 are assigned to υ(Si-O) stretching vibration, which is in agreement with the presence of quartz in the sphere. The peaks at 656cm^{-1} (peak 8), 584cm^{-1} (peak 9) and 434cm^{-1} (peak 11) can be assigned to the Al–O stretching mode in octahedral structure, while the bands around 721 cm^{-1} (peak 7) and 992 cm^{-1} (peak 4) are related to Al–O stretching mode in tetrahedron and symmetric bending of Al–O–H, respectively. The broad absorbance bands between 900 and 1100 cm^{-1} (peak 5) are assigned to O–H deformation vibrations.

Finally, the peak in the region of 465 cm^{-1} (peak 10 in the Figure 21) corresponds to the bond of Ti-O-Ti stretching mode and it confirms once more the presence of TiO_2 on the geopolymer sphere.

c) Ultraviolet-visible Spectroscopy

The UV-Vis spectrum of the geopolymer spheres (Figure 22) shows that these absorb light in the visible and UV-Vis region, with maximum peak of light absorption at 335 nm in the region of UV light.

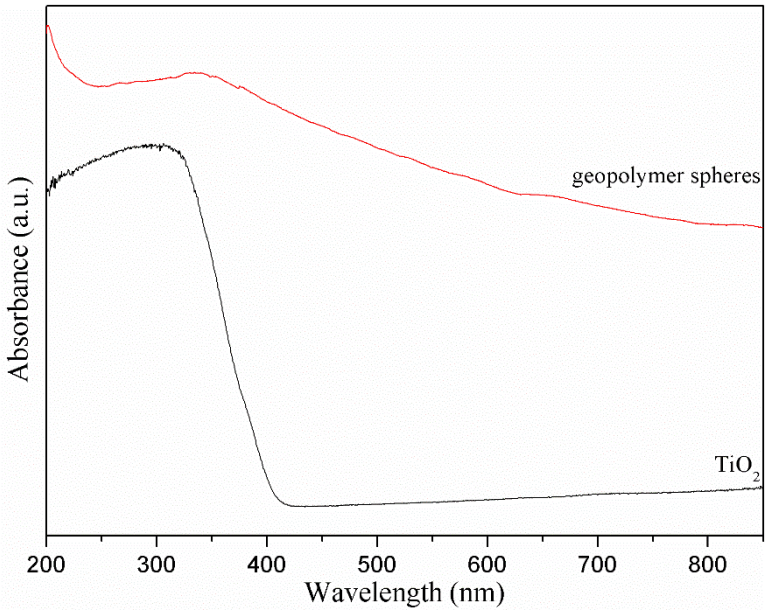

Figure 22 - UV-vis spectra of the geopolymer spheres and TiO_2 P25.

d) Scanning Electron Microscopy

The scanning electron microscopy is a technique which allows to obtain images of the particles present on the samples, by the interaction with a beam of electrons, which is produced by the equipment. With the images obtained, it is possible to study the morphology of the particles. [76]

The SEM images of the porous spheres are included in the Figure 23. Observing them, it is possible to conclude that all the spheres have a big pore and in the surface of the pore, there are other small pores. Besides that, the surface of the spheres it is not homogeneous and presents some microstructures.

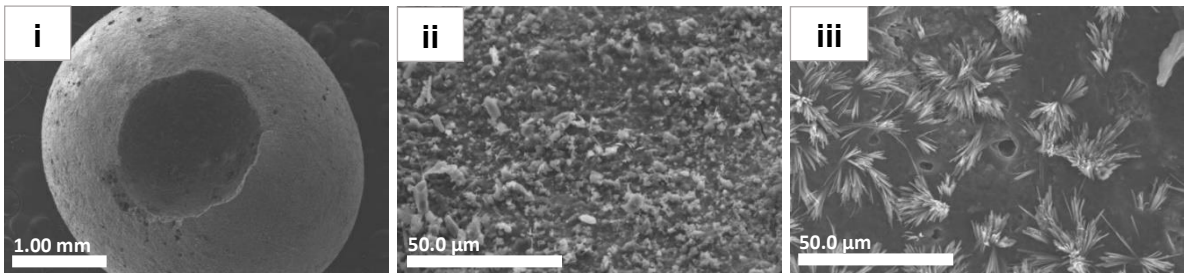

Figure 23 - Images of SEM of the geopolymer spheres: general view of the sphere (i), surface of the sphere (ii) and surface of the inside of the pore (iii).

3.3 Conditions of photocatalysis

Following the protocol previously described in the methods section, the tests of photocatalysis were done with the effluent D0 collected in March 2018. The Table 6 summarizes the experimental conditions of each test. The effect of the type of photocatalyst, the type of stirring and the irradiation conditions (UV light or dark) were investigated and the tests were divided in four groups. In the Sets A and B the photocatalyst prepared was used (in presence and absence of radiation, respectively), in the Set C the experiments were performed with the photocatalyst recovered from Set A and the Set D includes experiments that were performed without photocatalyst.

Table 6 - Summary of the experimental conditions of each test performed.

Set	Test number	Photocatalyst			UV radiation	Stirring		H_2O_2
						Magnetic	Flux of compressed air	
A	1	TiO_2			x	x		x
	2						x	
	3	Fe_3O_4						
	4	Fe_3O_4/TiO_2	(1:1)					
	5		(1:2)					
	6		(1:3)					
	7		(1:3) cfg					
	8	spheres				x		
	9						x	
B	10	TiO2				x		x
	11						x	
	12	Fe_3O_4						
	13	Fe_3O_4/TiO_2	(1:1)					
	14		(1:2)					
	15		(1:3)					
	16		(1:3) cfg					
	17	spheres				x		
	18						x	
C	19	Fe_3O_4		recovered	x		x	x
	20	Fe_3O_4/TiO_2	(1:1)					
	21		(1:2)					
	22		(1:3)					
	23		(1:3) cfg					
	24	spheres				x		
	25						x	
D	26	(-)			x	x		
	27						x	

The temperature of the effluent was monitored during the photocatalytic tests, as presented in the Figure 24 and, in detail, in the Table B. 1, while the temperatures of the heating bath in each test are presented in the Table B. 2.

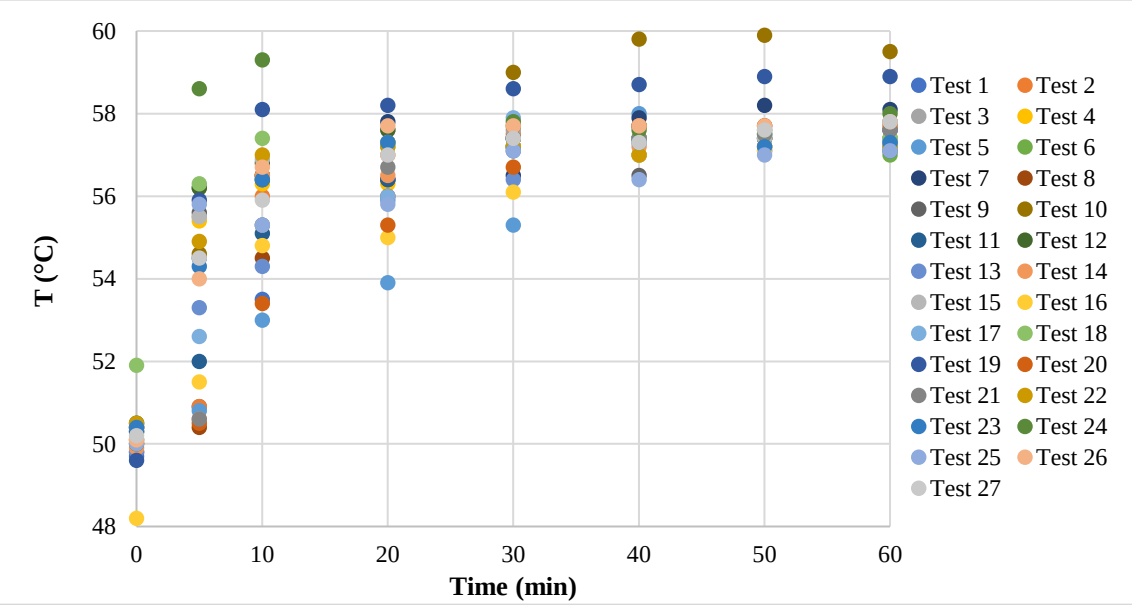

Figure 24 - Register of the temperatures of the effluent during the photocatalytic tests.

For all the tests, the initial temperature of the heating bath was 52 °C and due to the different conditions of each test, the time to reach the minimal temperature of 57 °C in the effluent was different, particularly between the tests performed with/without radiation. The aim was to perform the experiments at temperatures within the range 57-60 °C, that are the working temperatures on the factory, from where the effluent was collected. It is also known that the temperature has a relation with the photocatalysis efficiency and temperatures in the range 20-80 °C have been regard as the desired temperature for effective photo mineralization of organic content. [29]

For each experiment, photos of the effluent were taken at three different stages of the treatment; 1 – untreated effluent, 2 – just after addition of H_2O_2 and 3 – after 1hour of treatment, in order to analyse the colour variation of the effluent. The photos are presented in the appendix C (Figure C. 1 to Figure C. 8) and it is possible to observe that in the tests performed with magnetic nanoparticles, the treated sample is, in general, darker than the samples before the photocatalytic treatment. In contrary, in the tests performed with TiO_2 P25 (test 1 and 2), the effluent became cleared after the photocatalytic treatment.

3.4 Removal of AOX

After the photocatalytic tests, the concentration of AOX of each sample was measured. An overview of the results is shown in the Figure 25 and more in detail in the Table C. 1. The Figure also shows the AOX removal percentage immediately after the addition of H_2O_2, before starting the irradiation of the sample with UV light (or in dark for comparison).

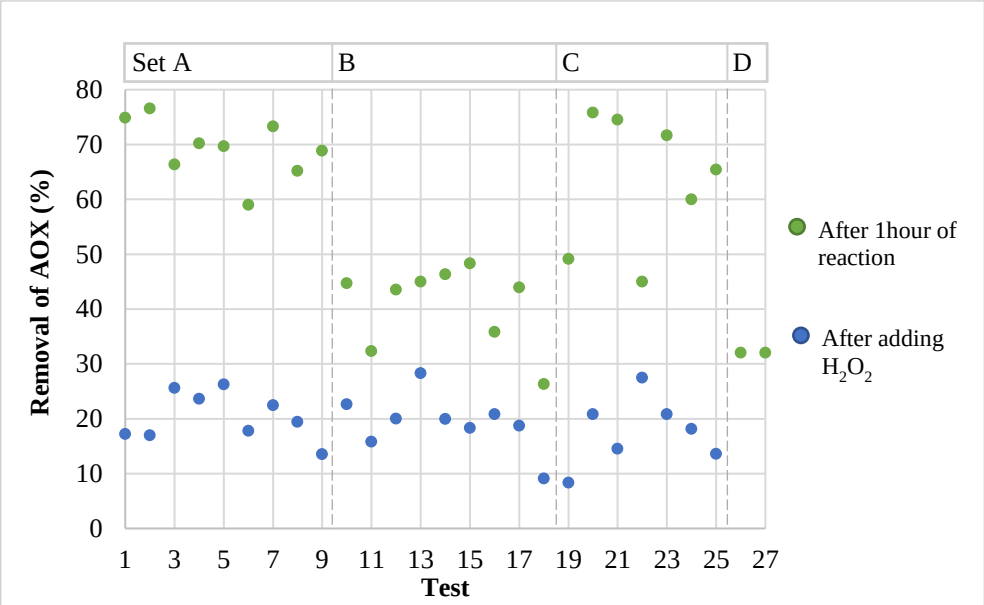

Figure 25 - Percentages of AOX removal from effluent DO in all tests.

Analysing the Figure 25, we conclude that the best results were obtained in the test 2, with a removal percentage of 76.6%. In this test the TiO_2 P25 was used as photocatalyst together with UV radiation. The stirring conditions, magnetic stirring or bubbling compressed air do not seem to affect significantly the removal of AOX, once the removal percentage in test 1 was 74.9%. The percentages of AOX removal using the other materials (tests 3-9) were slightly lower, ranging from 59.0 to 73.3%. The differences observed between the P25 and the photocatalysts supported are probably related with the different mechanisms of AOX degradation associated with each one. Furthermore, in the tests 8 and 9 were used a higher quantity of photocatalyst.

The tests of the Set B (tests 10-18) were performed in the dark, without UV radiation, and, as expected, had a lower AOX removal than in irradiated samples, varying from 32.3 to 48.3%. The UV radiation activates the photocatalyst and consequently induce the production of more radicals. The Set C (tests 19-25) evaluates the reuse of the catalysts and thus correspond to the tests performed with recovered photocatalyst and return values of AOX removal similar to the ones of Set A, however these results will be analysed more in detail further.

Finally, the tests 26 and 27 are control tests and were performed without photocatalyst and H_2O_2, to access the effect of the UV radiation on AOX photodegradation. The resulting AOX removal was relatively low (32.1%), which confirms the importance of use a photocatalyst to improve the amount of AOX removed from the effluent.

In all the tests performed with a photocatalyst, there was addition hydrogen peroxide, before the start of the photocatalysis, and a sample was taken to evaluate the AOX concentration. As shown on the Figure 25, in all the tests it was possible to remove around 20% of the initial concentration of AOX, that can be ascribed to adsorption effects. But the addition of hydrogen peroxide promotes, during the time of photocatalysis, the formation of more $^{\bullet}OH$ radicals, Equation (11), which increases the rate of AOX degradation. Besides that, these radicals can act as electron scavengers inhibiting the electron-hole recombination of the photocatalyst.

3.4.1 Removal of AOX using TiO_2 P25

The effluent was treated with TiO_2 P25 and, for comparison, without any photocatalyst, in different conditions. The results are presented in the Figure 26.

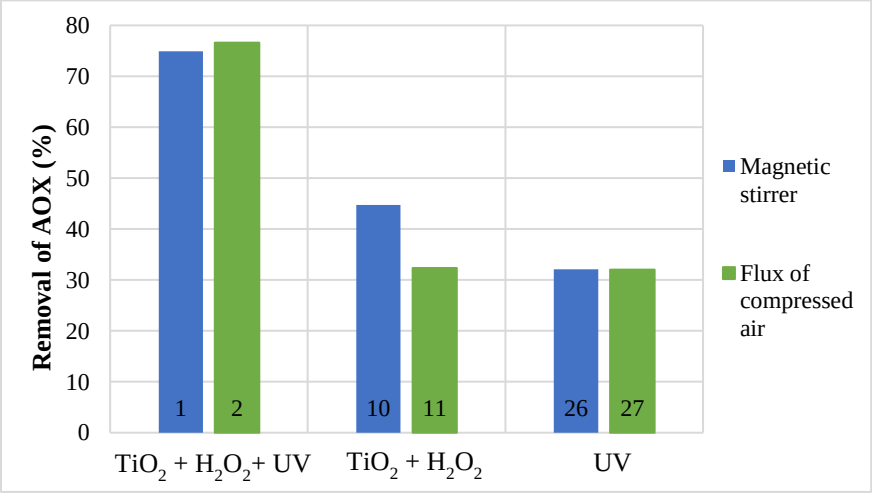

Figure 26 - Percentages of AOX removal in the tests with and without TiO_2 in different conditions. The numbers in the bars correspond to the test number.

As described before, the photocatalyst showing the better performance in the AOX removal was TiO_2 P25 with around 76% of AOX removal after 1h of treatment. Experiments performed with P25/H_2O_2 in the dark (trials 10-11) and without photocatalyst, but with UV radiation (trials 26-27) yielded lower AOX removals, between 44.8% and 32.1%. Another interesting point to note is about the effect of the type of stirring. When a source light was used, the results did not variate with the

stirring method, but in the tests without UV radiation, the magnetic stirring provide better results. By this, we can conclude that in tests with UV radiation, the type of stirrer did not affect the performance of the photocatalyst, which is an important condition for the comparation of this results with the ones performed with magnetic nanoparticles.

3.4.2 Removal of AOX using magnetic nanoparticles

The tests performed with magnetic nanoparticles, Fe_3O_4 and Fe_3O_4/TiO_2, used always a flux of compressed air as method to stirrer the solution and disperse the photocatalyst particle. The results obtained shown in the Figure 27.

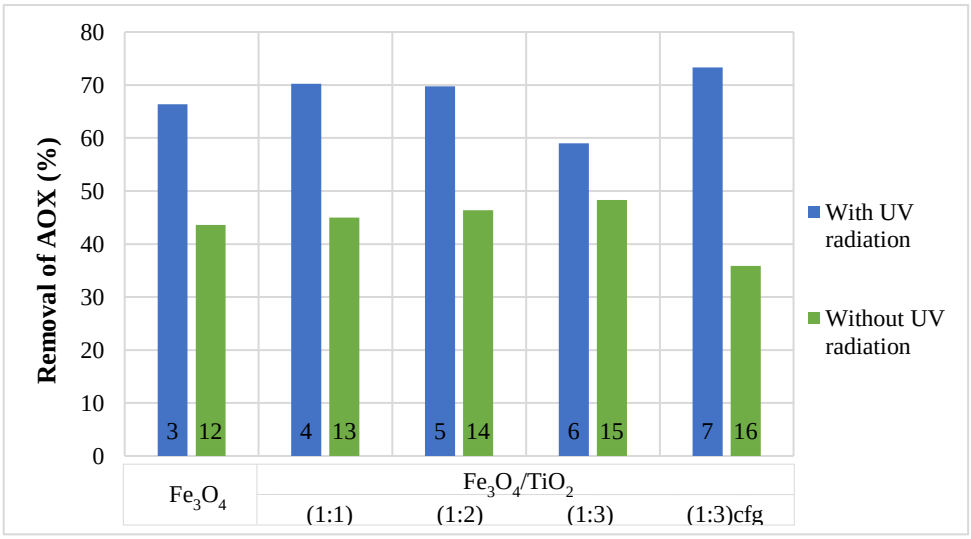

Figure 27 - Percentages of AOX removal in the tests with magnetic nanoparticles. The numbers in the bars correspond to the test number.

As previously mentioned, the results above clearly indicate distinct removal behaviour with and without UV radiation. In the tests 3-7, which were performed with UV radiation, from 59.0% to 73.3% of AOX of the initial effluent was removed, while in the tests 12-16, that were performed without UV radiation, just 36% to 48% of AOX removal was achieved.

In general, the AOX removal was not as high as in the tests performed with TiO_2 P25 alone. In these experiments the mass of photocatalyst used was kept constant (0.200g), but the percentage of titanium dioxide in the magnetic nanoparticles was smaller, because they are also composed by magnetite.

The process of AOX removal using this type of magnetic photocatalysts can be very complex, since two AOP might be involved, the heterogeneous photocatalysis and the Photo-Fenton process.

In the heterogeneous photocatalysis, the particles of TiO_2 absorbs the UV radiation and since the energy of the incident light is larger than the band-gap of TiO_2, electrons in the valence band are excited to the conduction band, leaving holes in the valence band, Equation (4). This promotes the adsorption of AOX on the active sites of the photocatalyst surface and the formation of several radicals, that allows the oxidation and degradation of AOX, as indicated in the Equations (5) to (12). If we would consider just this mechanism to take place, we could expect that the higher the TiO_2 content, the higher the number of AOX compounds oxidized, which would lead to less AOX in the treated effluent. Nevertheless, the results do not show a straight dependence of AOX removal with the TiO_2 content on the magnetic catalysts.

During the photocatalytic treatment, it is possible that some ferric ions from magnetite can be released from the particles surface to the surrounding solution, which would promote the formation of more radicals, by the Photo-Fenton process (see Equations (1) and (2)) and consequently promote the oxidation of AOX.

In addition, magnetite is known to be unstable under oxidizing conditions (in presence of H_2O_2 and/or O_2) and can be converted in hematite or maghemite, Equation (22). [28]

$$2\ Fe_3O_4 + ½\ O_2 \rightarrow 3\ Fe_2O_3 \qquad (22)$$

As reported in the literature, there is the possibility of the photo-generated electrons in the conduction band of the nanoparticles of TiO_2 would be transferred to the nanoparticles of Fe_2O_3, while photo-generated holes are accumulated in the valence band of TiO_2, Figure 28. This facilitate the charge separation, which may resulte in a delay in the electron-hole recombination and accelerates the oxidation efficiency by holes and reduction rate by electrons. However, this is just reported for Fe_2O_3 since the band gap of Fe_3O_4 is much smaller (2.20eV for Fe_2O_3 and 0.10eV for Fe_3O_4). [28]

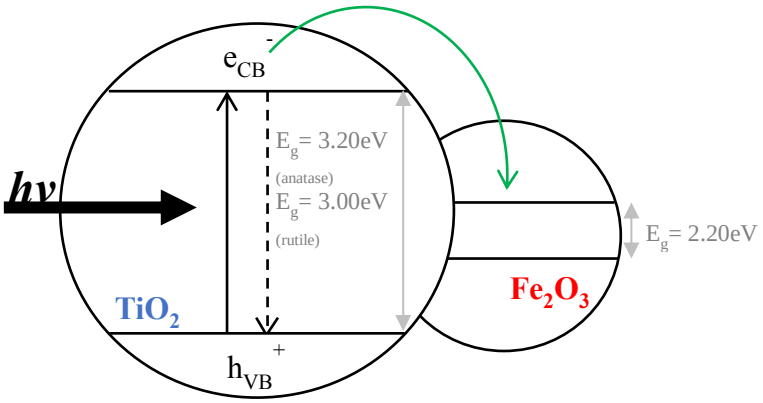

Figure 28 – Possible charge carrier transfer in TiO_2/iron oxide systems. [28]

In conclusion, even at first sight could be admitted that the nanoparticles Fe_3O_4/TiO_2 containing more TiO_2 would be more efficient to remove AOX from the effluent, due to the three possible mechanisms described before, also the magnetite nanoparticles also plays an important role in the process of AOX decomposition.

Although the results obtained with the several magnetic photocatalysts did not fluctuate so much, to confirm their similar ability to remove AOX it would be necessary to make some replica of each test. Beyond that, it would be also interesting to analyse the variation of AOX percentage with time during the test of photocatalysis and not only after 1hour of treatment, since it could give more information about the possible differences between the different photocatalysts.

3.4.3 Removal of AOX using geopolymer spheres

The geopolymer spheres were used as photocatalysts to perform four tests (8,9 17 and 18), with and without UV irradiation and varying the type of stirring. The results obtained are presented in the Figure 29 and show that UV irradiation enhances the AOX degradation.

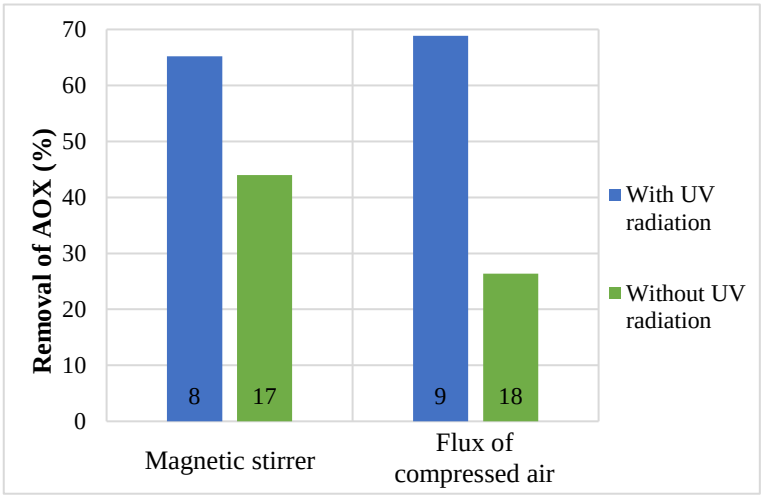

Figure 29 - Percentages of AOX removal in the tests with geopolymer spheres. The numbers in the bars correspond to the test number.

The best AOX removal achieved using spheres was 68.8% which is smaller than the AOX removal using P25. However, note that a direct comparison of these results with those obtained using TiO_2 or magnetic nanoparticles should not be done, since the total amount of catalysts used in the experiments was different. In the tests with the geopolymer spheres, 2.0 g of photocatalyst were used while in the tests with TiO_2 and magnetic nanoparticles the amount of catalysts per trial was 0.2 g. Having in mind that according to the XRD data, the spheres contain around 20wt% of titanium dioxide, corresponding to 0.4g TiO_2, so in a first analysis we could expect better photocatalytic

performance of the sphere. Nevertheless, the spheres are much larger that nanoparticles and most likely with much smaller specific surface area than TiO_2 nanoparticles. Moreover, the TiO_2 might be located also in the inner part of the sphere, so there is a percentage that probably cannot participate in the photocatalysis, until the spheres are broken or disaggregate. These two factors might explain the lower efficiency of the spheres in the photocatalytic treatment.

As for the agitation method used, it was observed that in the tests performed with UV radiation this did not affect the results obtained, since similar AOX removal values were obtained for tests with magnetic stirring and with compressed air flow. However, when no radiation was applied, the magnetic stirring allowed to obtain a higher percentage of removal of AOX.

3.4.4 Effect of the photocatalytic treatment on the pH of the effluent

During the photocatalytic treatment, the pH value may vary depending on the conditions of the tests and on the photocatalyst used. The pH values before and after the photocatalysis tests are presented in the Figure 30 and in the Table C. 2, in detail.

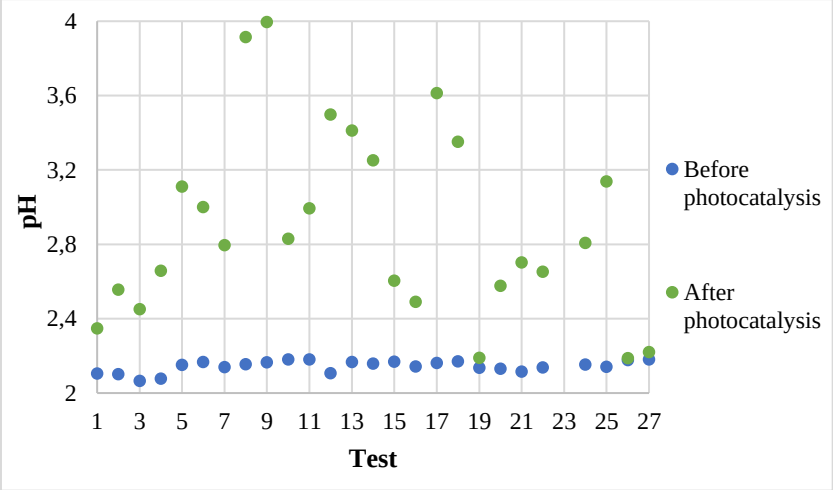

Figure 30 - Register of the pH of the effluent before and after the photocatalytic tests.

In all the tests performed, the pH values of the effluent before and after the treatment were different and increased after treatment, with exception of the tests 26 and 27, where the pH remained invariable. In these two tests, there was not used any photocatalyst or addition of H_2O_2, but both were performed with UV radiation. Based on this result, we can conclude that the use of radiation was not the parameter that inducing the variation of the pH value on the other tests.

Aiming to compare the pH variations on the other tests, the pH increase in percentage was calculated. The results obtained are shown on the Figure 31 and in the Table C. 2.

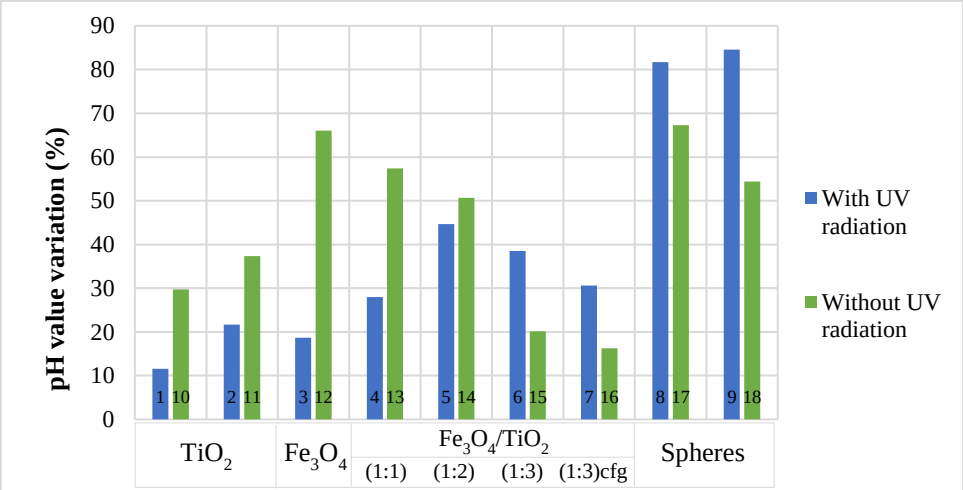

Figure 31 - Percentages of the increase of the pH value of the effluent comparing the tests of Set A (with UV radiation) and Set B (without UV radiation). The numbers in the bars correspond to the test number.

In the tests performed with TiO_2 P25, it was observed increase of the pH value of the effluent, 15% when UV radiation was used and 35% when UV radiation was not used. The type of stirring also influenced the variation of the pH and it seems that using the compressed air flux promotes a larger increase of the pH than when using magnetic stirring.

In the tests performed with magnetic nanoparticles and UV radiation, the increment of the pH value varied from 18.7% to 44.7% and it was observed an increase of the variation with the increase of the amount of the TiO_2 content in the photocatalyst until reaching the ratio Fe_3O_4/TiO_2 (1:2) and a decrease at higher ratios. In opposite, in the tests performed without UV radiation, the increment of the pH value decreased with the increase of the TiO_2 content in the photocatalyst, from 66.1% in Fe_3O_4 to 16.3% Fe_3O_4/TiO_2 (1:3). Overall, when using magnetic nanoparticles, the pH increment was larger in the experiments carried out in dark conditions, with exception of the samples (1:3) and (1:3) cfg, that have shown larger pH increase with UV light exposure. Since the AOX removal results were similar using magnetic photocatalysts of different composition, it is not possible to stablish a correlation between the removal of AOX, the pH variation and the presence or absence of UV radiation.

In the tests with spheres, the pH increase after treatment was the largest and it was more pronounced in the experiments carried out with UV radiation. In the tests performed with UV radiation, the pH value of the effluent increased in 81.7% to 84.6%, while in the tests without UV radiation, the variation was just 54.4% to 67.3%. In the former case, the use of UV radiation, associated with a higher efficiency to remove AOX, induce a higher increase of the pH value of the effluent. These higher results may be probably related with the chemical composition of the spheres and with the fact that they are less stable in acidic media.

3.5 Recovery of the photocatalysts

Having in mind the possible reuse of the catalysts, the magnetic nanoparticles and the geopolymer spheres were recovered after the photocatalytic tests, washed with milli-Q water and absolute ethanol, dried and weighted. The percentage of recovery was calculated and the values are shown in the Figure 32. All the masses obtained, i.e. the mass of photocatalysts before and after the photocatalysis, are presented in the Table D. 1.

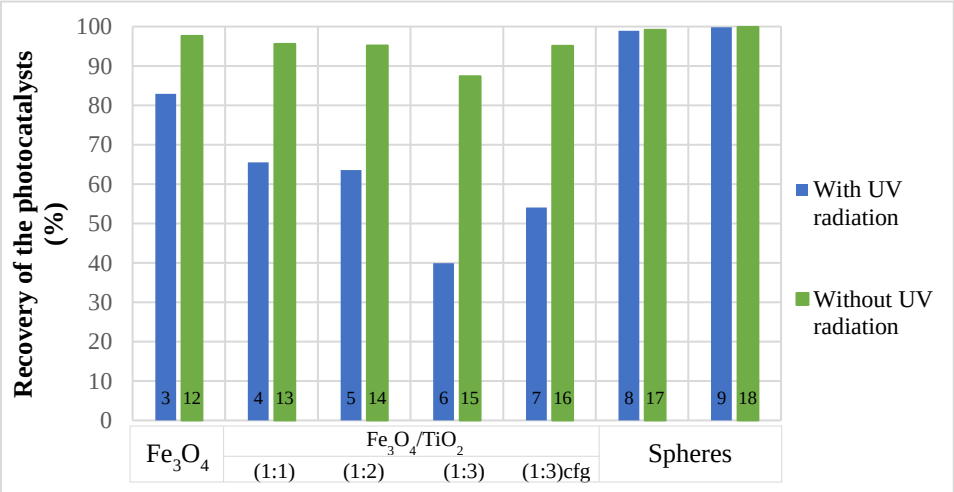

Figure 32 - Percentages of recovery of the photocatalysts used on the tests of Set A (with UV radiation) and Set B (without UV radiation). The numbers in the bars correspond to the test number.

According to the results obtained, it is possible to conclude that the magnetic nanoparticles are sensitive to the UV radiation, because when they were not exposed to the radiation (tests 12-16), the percentage of recovery was much larger and near 100%. This is in agreement with previous works that indicate photodissolution of magnetite nanophases, namely when it is doping the surface of TiO_2. [77]

Besides that, the percentages of magnetite and titanium dioxide present in the nanoparticles also seem to influence the percentage of recovery. Thus, the higher the magnetite content in the magnetic nanoparticles, the larger is the amount of particles recovered magnetically. This tendency is more evident when UV light is used and the explanation can be once more related with the magnetic separation of the nanoparticles, which allow the recovery of more magnetite, while the TiO_2 nanoparticles that are not bonded to the magnetite are lost.

Relatively to the geopolymer spheres, the percentages of recovery are almost 100% in all the tests. These results do not prove that all the spheres were conserved, because after the tests, it was possible to see some of the spheres broken or degraded, Figure 35.

3.5.1 Magnetic nanoparticles

Though, it is important to determine the percentage of recovery, it is also relevant to analyse if the nanoparticles suffered any change in their structure during the photocatalytic treatment, in their morphology or chemical composition. In general, a naked eye observation suggests that the magnetic nanoparticles did not suffer any change in their visual aspect, maintaining the same colour that was dark brown, as presented in the Figure D. 1. The only exception was the magnetic nanoparticles recovered from the test 3, which form a thin film, that was not possible to grind in the mortar.

a) <u>X-ray powder diffraction</u>

XRD technique was used to identify the crystalline phases present in the magnetic nanoparticles after the photocatalysis. The respective diffractograms obtained are presented in the Figure D. 3. In general, the diffractograms obtained for the magnetic nanoparticles after the photocatalysis are very similar to those obtained before photocatalysis, as no new diffraction peaks apperead. This means that the photocatalytic tests did not affect significantly the composition of the nanoparticles, once it was just observed some changes in the intensity of some peaks. The weight percentages of the components of the magnetic nanoparticles were estimated from XRD data and are presented in the Figure 33.

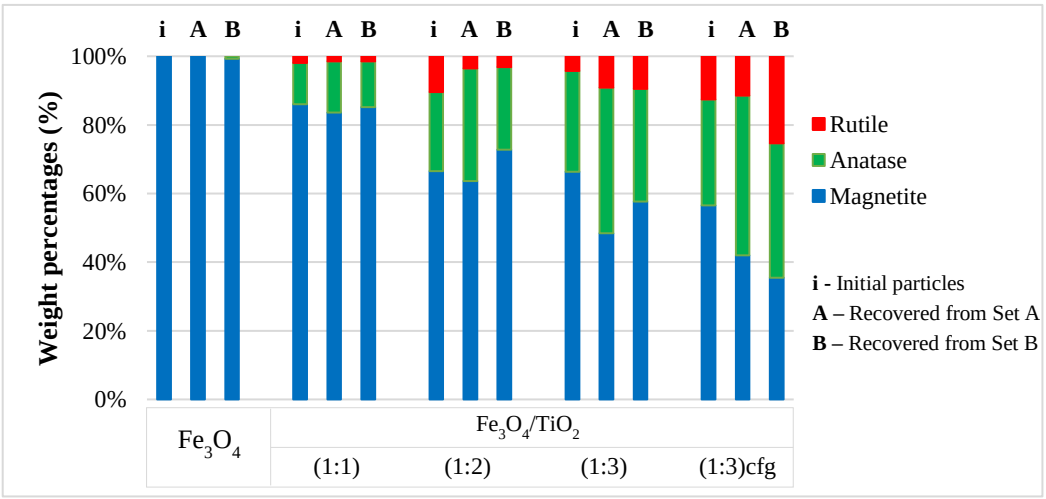

Figure 33 - Weight percentages of magnetite and titanium dioxide (anatase and rutile) on the recovered magnetic nanoparticles from tests of Sets A and B.

In general, the composition of the magnetic nanoparticles did not suffer significant changes during the photocatalytic treatment. The more significant change was observed for Fe_3O_4/TiO_2 (1:3) centrifuged, where the weight percentage of magnetite deceased after the photocatalysis in both Sets and consequently the titanium dioxide content (anatase and rutile) increased.

b) Fourier-Transform Infrared Spectroscopy

To assess if there were changes in the chemical composition of the material the FTIR spectra were acquired, Figure D. 5.

Even the results observed are different according to the photocatalyst used, in all of them the characteristic peaks remain in the same wavenumber, which prove the main bonds were maintained. However, the absorbance of each peak is not the same as in the spectra of the photocatalysts before photocatalysis, with exception to Fe_3O_4/TiO_2 (1:3), which spectrum of the nanoparticles after photocatalysis is very similar, independently of the use or not of UV radiation. In the other particles, when UV radiation was used, the absorbance of the peaks decreased for Fe_3O_4 and Fe_3O_4/TiO_2 (1:1) and increased for Fe_3O_4/TiO_2 (1:2), while in case of dark, the absorbance increased in all the magnetic nanoparticles. Besides this, the spectra of Fe_3O_4/TiO_2 (1:1) and Fe_3O_4/TiO_2 (1:2) after the photocatalysis have a significant peak at wavenumber 1700 cm^{-1}, which can be related with some contamination of the photocatalyst with compounds present on the effluent.

3.5.2 Geopolymer spheres

Following the analysis performed for the magnetic nanoparticles, a similar characterization was performed for the geopolymer spheres. Visually, some of the spheres used in the tests 17 and 18 seemed degraded or broken, while the spheres from the tests 8 and 9 did not broke, but have their pores larger than before the photocatalytic treatment, Figure D. 8. One interesting aspect was the change of the colour of the spheres immediately after the end of the photocatalysis, Figure D. 9. Some of the spheres were half red, half purple, regardless the conditions of the test, but, after dried, the red colour disappeared.

a) X-ray powder diffraction

Aiming to identify the main crystalline components in the spheres after the photocatalysis, the XRD technique was used and the diffractograms obtained before and after treatment were compared, Figure D. 11. In general, the two diffractograms are very similar in terms of the angle of the diffraction peaks and the intensity of each one, which means that the composition of the spheres was not markedly changed by the photocatalytic treatment. More important, the peaks related to the presence of titanium dioxide in the sphere, namely the anatase and rutile phases, are observed in the diffractogram of the spheres recovered, which prove that these spheres keep the titanium dioxide on them. However, there are some slight differences in the XRD data of the spheres before and after the

photocatalytic treatment. In the region of 2θ = 35°, the intensity of the peak is higher in the spheres after the photocatalysis, while in the region of 2θ = 60° the intensity of the peak is lower in the spheres after the photocatalysis. Also, in the region of 2θ = 36°, appears one peak in the diffractogram of the sphere after the photocatalytic treatment. However, these changes were not very significant and did not affect the previous conclusions taken.

The weight percentages of the main components of the geopolymer spheres where estimated from the XRD data and compared with the initial values (Figure 34 and Table D. 2).

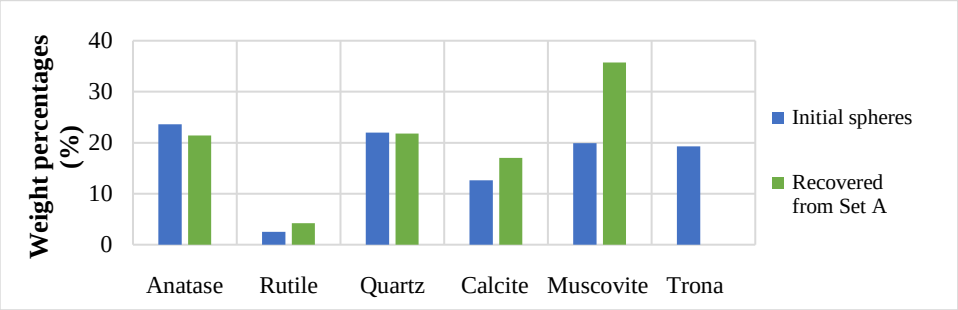

Figure 34 - Weight percentages on the geopolymer spheres before and after the photocatalysis, Set A.

According to the values obtained, the composition of the spheres changed with the photocatalytic treatment, because there are some differences in the percentage of each component.

In terms of the titanium dioxide present in the geopolymer spheres, even the percentage of the rutile phase has increased, the percentage of anatase suffer a small decrease. Combining the two effects, the total percentage of titanium dioxide did not vary and the differences observed can be explained by the loss of mass of titanium dioxide in the step of recovery.

In terms of the minerals of the spheres, the most marked difference is related with the percentage of trona, that is absent after the photocatalysis, while the weight percentage of calcite and muscovite increased. These changes in the spheres can be explained by the experimental conditions used in the photocatalytic tests, as low values of pH and high temperatures, and some components can be more sensitive to these conditions than others.

b) Fourier-Transform Infrared Spectroscopy

Then it was evaluated the changes on the bonds of the components of the spheres, Figure D. 5. In terms of the mains bonds between the components of the geopolymer spheres, the photocatalysis did not affect them, because there were no shifts of the peaks on the FTIR spectra, neither new vibration bands have appeared. Besides that, the different conditions of each test did not influence

the bonds and interactions of the components in the spheres, because the spectrum of each test are similar to the other ones.

c) Scanning Electron and Optical Microscopy

Finally, the spheres were analysed by SEM and it was possible to compare the surface of them before and after the photocatalytic treatment, Figure 35. Note the images of the sphere analysed after the photocatalysis were taken in the opposite side of the pore, which means that the sphere also has a pore, as all the other spheres.

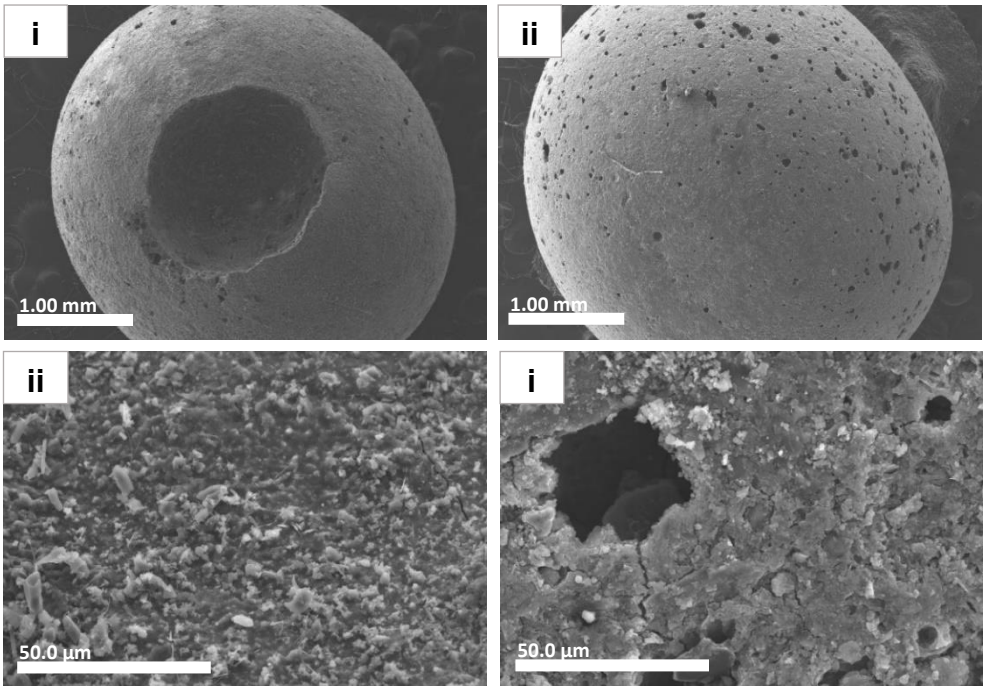

Figure 35 - Images of SEM of the geopolymer spheres before (i, iii) and after the photocatalysis, test 9 (ii, iv).

Comparing the images (i) and (ii) of the Figure 35, it is possible to see the increase of the number of macropores on the surface of the geopolymer sphere. This is also proven on the image (iv), where it is observed a large macropore. In conclusion, the use of the spheres in the treatment of D0 causes the degradation of their surface, regardless of the conditions used in the treatment. They have become more fragile than before, probably due to the photocatalytic mechanism or due to the contact with the effluent.

It was also used the optical microscopy to see the surface and the porous of the spheres after the photocatalysis. The images obtained are in the Figure D. 16 and it was helpful to see the degradation on the wall of the pore. Once it is a technique faster to utilize, there was observed a several number of spheres and it was concluded that the level of degradation on the surface and on the pore of the spheres was not equal for all the spheres.

3.6 Reutilization of the photocatalysts

Once the use of UV radiation to improve the AOX removal in the effluent D0 was confirmed, new photocatalytic tests were performed using the photocatalysts recovered from Set A. The procedure was followed as before, but the conditions were adjusted to the new amount of available photocatalyst to use. The new volumes of effluent and H_2O_2 were calculated and are present in the Table B. 3. The temperatures were also monitored to be in the interval stablished, as presented on the Table B. 1. The percentages of AOX removal after one hour of photocatalysis, for each test, is shown in the Figure 36, which was built with the values of the Table C. 1.

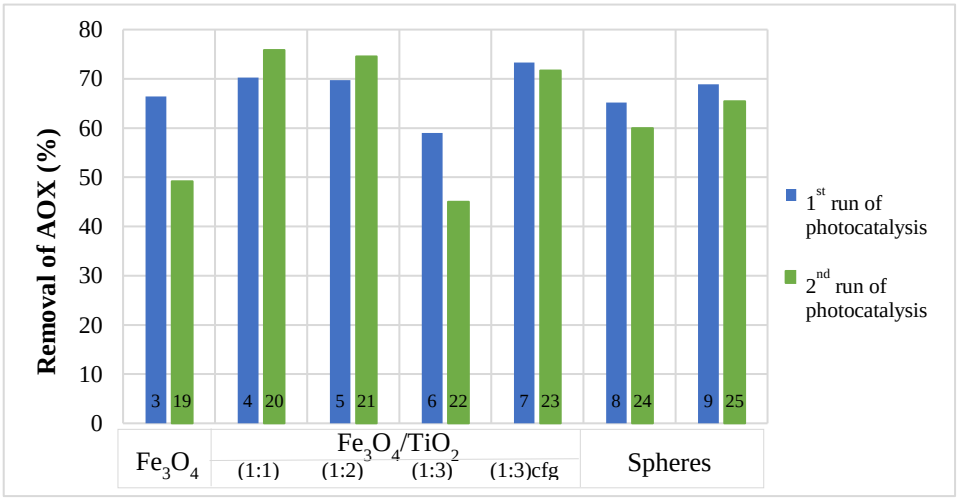

Figure 36 - Percentages of AOX removal in the tests of Set A (1st run of photocatalysis) and Set C (2nd run of photocatalysis). The numbers in the bars correspond to the test number.

For some of the magnetic nanoparticles, the results obtained were similar of those of Set A, namely for Fe_3O_4/TiO_2 (1:1), (1:2) and (1:3) centrifuged, with values varying from 71.7 to 75.8%. For the photocatalysts Fe_3O_4 and Fe_3O_4/TiO_2 (1:3), the percentages of removal were lower than in the tests of Set A, with values of 49.2 and 45.0%, respectively. The decrease of the photoactivity of Fe_3O_4 in this 2nd run of tests is a consequence of the non-dispersibility of the photocatalyst, as it was not possible to grind it in the mortar, as explained before. The lower value of AOX removal of Fe_3O_4/TiO_2 (1:3) is probably related with the lower quantity of effluent used in the test 22. Because the quantity of photocatalyst recovered from test 6 was very small (40%) the adjusted volume of effluent used in the test 22 was in concordance just 74mL (40% of the volume of the initial tests) and when this quantity was added in the photoreactor, it did not cover the level of the UV light, thus the conditions of irradiation were different.

In the tests with the recovered spheres, the removal of AOX from the effluent were lower than in the tests with the initial spheres, however the difference was not as marked as in the magnetic

nanoparticles mentioned before. In terms of the stirring method, the use of an air flux provided the best results (test 24 - 60.0% and test 25 - 65.5%).

In general, the photocatalysts did not lose their ability to reduce the concentration of AOX in the effluent after one run of photocatalytic tests. However, it is still not possible to conclude that they can be used successfully in more consecutive tests, since it would be necessary to repeat these ones and carry out more series of tests, with recovered photocatalysts after 3 or 4 runs, for example.

After the 2nd run, all the photocatalysts used were again recovered, washed, cleaned and dried and the percentages of recovery calculated (Figure 37 and Table D. 1).

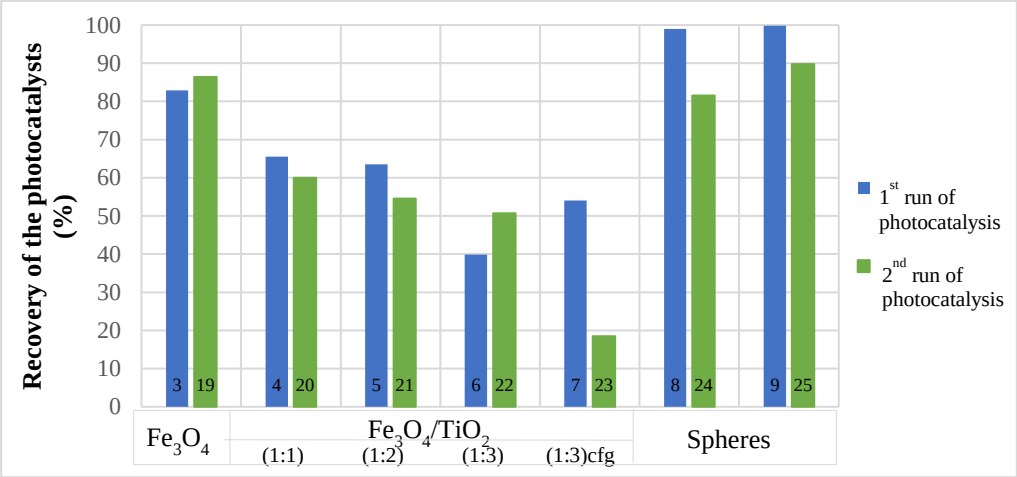

Figure 37 - Percentages of recovery comparing the photocatalysts recovered from the tests of Set A (1st run of photocatalysis) and Set C (2nd run of photocatalysis). The numbers in the bars correspond to the test number.

In general, the percentage of recovery of the photocatalysts in the Set C follow the same tendency as in the Set A, but the results are more evident. For the magnetic nanoparticles, the percentage of recovery decrease with the increase of the percentage of TiO_2 on the photocatalyst, which means values of recover of 86.4% for Fe_3O_4 and 18.5 to 60.0% for Fe_3O_4/TiO_2. These differences can be explained by the Equation (23), that correlates the magnetic force acting on a particle during the magnetic separation process, F_m, with the magnetic permeability of the free space, μ_0, the volume and the magnetization of the particle (V_p and M_p, respectively) and the applied magnetic field intensity, H_a. [52] Thus, the larger the particle, the higher is the volume, V_p, and higher is the force that facilitates the magnetic separation. Furthermore, changes in the chemical composition might affect the value of the magnetization (M_p).

$$F_m = \mu_0 \times V_p \times (M_p \times \nabla) H_a \qquad (23)$$

The low values of recovery might be a consequence of some changes on the properties of the magnetic nanoparticles during the run of the photocatalysis, for example due to exposition of UV

light. This exposure might promote the oxidation and dissolution at the surface of the magnetic nanoparticles and as their size decrease, the force in the magnetic separation also decreases. Besides that, there is the possibility of the photodissolution of the magnetite be promoted by the contact with TiO_2. This contact can cause the electron transference from TiO_2 to Fe_3O_4, which induces the reductive dissolution of Fe(III) on the solution. [77]

Among the three types of iron oxides, the magnetite often shows the highest saturation magnetization due to the electron delocalization that can take place between adjacent site of both Fe^{2+} and Fe^{3+}. As described before, Equation (22), magnetite can be converted in maghemite and hematite, due to the oxidizing conditions, and both display lower magnetization saturation. So, if some of the nanoparticles lose their magnetic force the recovery of the material will not be complete, which also justify the small percentages of recovery obtained. In terms of the geopolymer spheres, the percentages of recover are not around 100%, as obtained in the Set A, but it is still possible to recover a larger amount of photocatalyst, with values in the range of 81.6 - 89.9%. [28]

The pH variations of the effluent after the tests of Set C were also monitored and are included in the Figure 38.

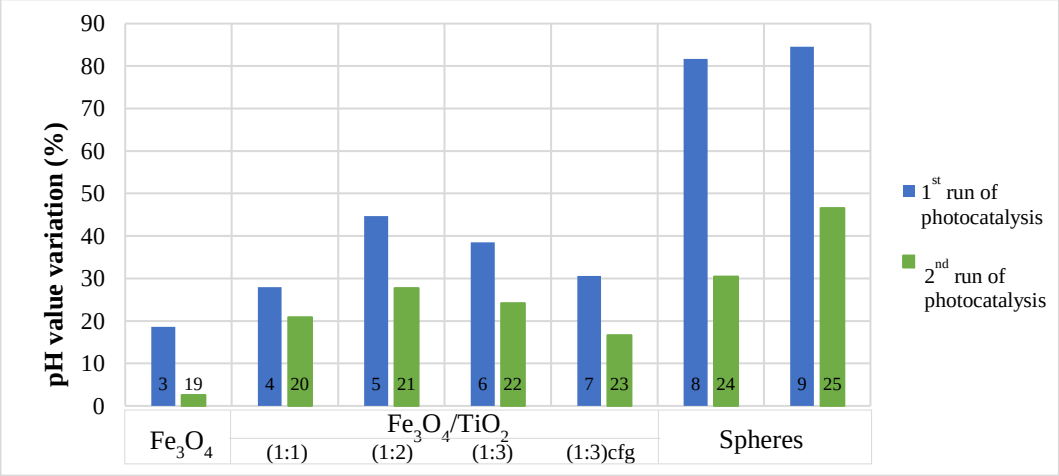

Figure 38 - Percentages of the increase of the pH value of the effluent comparing the photocatalysts recovered from the tests of the Set A (1st run of photocatalysis) and Set C (2nd run of photocatalysis). The numbers in the bars correspond to the test number.

In terms of the variation of the pH value, the behaviour observed at Set C is similar to that observed at Set A, although for all cases the pH increment was markedly lower in the Set C. The magnetic nanoparticles have their highest value of pH variation on the sample Fe_3O_4/TiO_2 (1:2), 27.8%, with a decrease in the two directions. This means, the variation of pH increase with the increase of TiO_2 on the photocatalyst used until Fe_3O_4/TiO_2 (1:2) and after, the pH variation tends to decrease. The pH variations on the geopolymer spheres were lower when a magnetic stirrer was used (test 24).

3.6.1 Magnetic nanoparticles

The visual appearance of the magnetic nanoparticles recovered from Set C is presented on the Figure D. 2. Compared with the nanoparticles previously prepared, these ones have the same colour, but their structure do not allow to crush them totally on the mortar, which not results in a powder as happen in the nanoparticles recovered from tests of Set A.

a) <u>X-ray powder diffraction</u>

As previous, the recovered photocatalysts were analysed by XRD, the diffractograms are presented in the Figure D. 4 and the relative weight percentages on the Figure 39. The diffractograms of all the magnetic nanoparticles recovered from Set C have the characteristic peaks of the crystalline phases of magnetite, anatase and rutile, which prove the presence of these components on the nanoparticles after the two tests of photocatalysis.

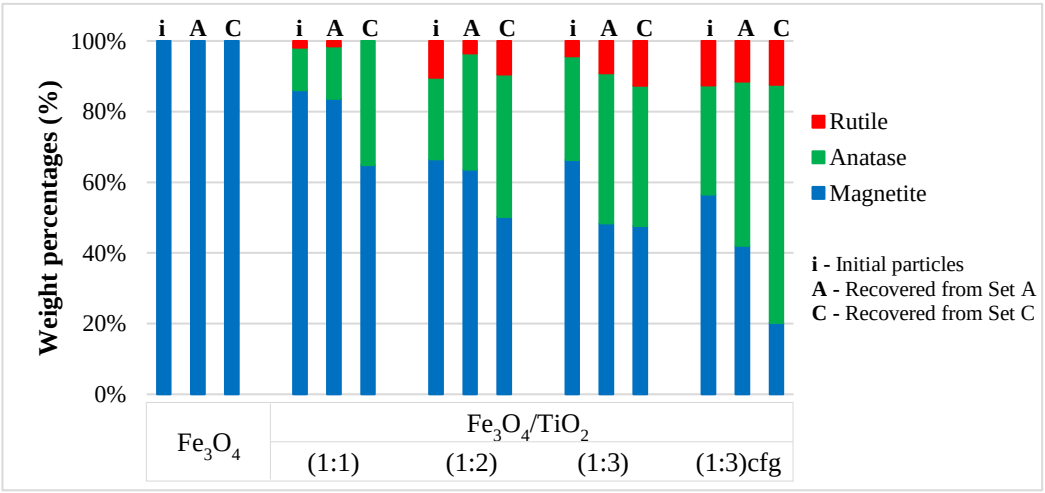

Figure 39 - Weight percentages of magnetite and titanium dioxide (anatase and rutile) on the recovered magnetic nanoparticles from tests of Sets A and C.

According to the weight percentages, it is possible to conclude the percentage of magnetite decreased in Fe_3O_4/TiO_2, from the initial particles to Sets A and C. The magnetite is known to be chemically unstable under oxidizing conditions and can be converted to hematite or maghemite, Fe_2O_3, as described in the Equation (22). Analysing the diffractograms of the nanoparticles after Set C more deeply, it is observed the appearance of a small peak at $2\theta = 27°$, which is a characteristic peak of the hematite.

Otherwise, the magnetite can be dissolved in acidic medium, so, probably during the two runs of photocatalysis, the magnetite in the photocatalysts was converted and/or dissolved in the effluent, which caused the decrease on its weight percentage. [28]

b) Spectroscopy

The Figure D. 6 shows the FTIR spectra of the recovered magnetic nanoparticles from Set C compared with initial particles and with the particles recovered from Set A. Analysing it, it is concluded that the main peaks were conserved, which prove the conservation of the main chemical bonds on the components on the magnetic nanoparticles. However, in these diffractograms were observed a new peak in the region of the characteristic bond of hydrocarbons. This can be related with some adsorption of compounds from the effluent on the photocatalysts.

There was also used the UV-vis spectroscopy, Figure D. 7, to determine the region of maximum light absorbance. Once it is in the region of UV light, we conclude the band gaps of the photocatalysts were not affected with the two runs of photocatalysis.

3.6.2 Geopolymer spheres

The visual appearance of the recovered spheres from Set C is presented on the Figure D. 10Figure D. 2. These spheres are significantly more degraded and broken than those recovered from the Set A, but the colour of them remained unchanged.

a) X-ray powder diffraction

The diffractogram obtained for the recovered spheres is shown on the Figure D. 12. Even the intensities of the main peaks are lower than the ones of the initial particles, there were no displacement of 2θ values. So, the main components were preserved, in particular TiO_2 that is one of the most important components of the spheres, since it is the responsible of photocatalysis efficiency.

b) Spectroscopy

In the Figure D. 14 is presented the FTIR spectra of the recovered spheres of the Set C compared with the initial particles and with the particles recovered from Set A. The spectrum of each sphere recovered from Set C has the characteristic peaks of the initial spheres, which prove the main bonds of the main components of the geopolymer spheres were maintained after two consecutive tests of photocatalysis.

The Figure D. 15 present the UV-vis spectrum of the geopolymer spheres after two runs of photocatalysis and once the region of maximum absorbed light was conserved at wavelengths below those of visible light, which indicates that they are still able to be activated by UV radiation.

4. Conclusions and Prospects

The main objective of the present work was to investigate several strategies for the immobilization of TiO_2 on different supports, in order to obtain an efficient photocatalyst for the photooxidation of AOX compounds present in the effluent resulting from bleaching stage from Kraft pulp mills and that could be easily recovered and reused. Two independent strategies were investigated: the preparation of TiO_2 with magnetic properties aiming easy and fast recovery by magnetic separation and the use of geopolymer spheres containing TiO_2, that were produced with a percentage of ash from residues of pulp and paper mills.

Therefore, the synthesis of TiO_2 with magnetic properties was carried out by co-precipitation of iron salts in the presence of commercial nano-TiO_2. These materials were characterized for the morphology and chemical composition using several techniques, which revealed the successful preparation of TiO_2 materials with magnetic properties, owing to the formation of magnetite (Fe_3O_4) nanophases. The TiO_2 content could be varied from 14.0 to 43.5% by adjusting the initial concentration of TiO_2 in the synthesis. Photocatalytic tests using UV light and H_2O_2 as oxidizing agent were performed to assess the performance of these materials on the photodegradation of AOX from bleaching stream of Kraft pulp making process. It was concluded that the treatment with magnetic TiO_2 for 1 hour allows the AOX removal in a range from 59.0 to 73.7%, when the tests were performed with UV radiation, and between 35.8 and 48.3% of AOX removal, when the treatment was done in dark. However, the results of AOX removal were similar regardless the content of TiO_2 on the photocatalyst. Owing to the magnetic properties of these nanoparticles, it was possible to recover them and it was proved that the chemical composition did not varied significantly.

Photocatalytic tests using the geopolymer spheres with TiO_2, show similar AOX removal results, being between 65.2 and 68.9% in the tests performed with UV radiation and between 26.4 and 44.0% in the tests performed in dark. The X-ray diffraction analysis of the spheres revealed that they are composed of TiO_2 and some other minerals, such as calcite, quartz and muscovite and that after the photocatalysis, their chemical composition in terms of crystalline phases did not suffer significant changes. However, the surface of the geopolymer spheres was degraded and showed increased porosity.

The reusability of the photocatalysts was assessed. The recovered photocatalysts were tested in a second series of photocatalytic tests and the percentages of AOX removal were similar to those obtained in the first run. Using the magnetic nanoparticles, the AOX removal varied from 45.0 to 75.8% and with the geopolymer spheres it was possible to remove 60.0 to 65.5% of AOX from the

effluent D0. The results indicate that the supported photocatalysts maintained their ability to remove AOX compounds, after being used once. Then, both photocatalysts were once again recovered and analysed. The percentages of recovery were lower in this 2nd run of photocatalysis and the weight percentage of magnetite decreased. This could be due to partial dissolution of the surface of the magnetite nanoparticles during the photocatalytic tests in acidic conditions. Besides decreasing the total amount of magnetite, this would decrease the particle size, and consequently weaker magnetic force will act on the nanoparticle during magnetic separation. However, further tests are necessary to be performed in the future, namely to test the reusability in further consecutive cycles.

In conclusion, the supported photocatalysts prepared allows to remove a significant quantity of AOX from the effluents, when the tests were performed with radiation. Although the AOX removal was lower than with unsupported nano-TiO_2 P25, this strategy was successful once it was possible to recover and reutilize the photocatalysts, as desired. In the future, all the tests should be repeated to assess the reproducibility and the working conditions should be studied deeply in the way to improve the performance of the photocatalysts and to develop a good method of recovery, in the way to increase the percentage of recovery as much as possible. Kinetic studies should be also performed to assess the AOX removal dependence with time.

5. Bibliography

[1] "CELPA," Associação da Indústria Papeleira, [Online]. Available: http://www.celpa.pt/. [Accessed 06 February 2018].

[2] E. Y. Hayasaka and S. M. Nishida, "A origem do Papel," UNESP, Universidade Estadual Paulista, [Online]. Available: http://www2.ibb.unesp.br/Museu_Escola/Ensino_Fundamental/Origami/Documentos/indice_origami_papel.htm. [Accessed 06 February 2018].

[3] H. Sixta, Handbook of Pulp, Lenzing, Austria: Wiley-VCH, 2006.

[4] M. Melo and M. Gouveia, *Pasta e Papel em Portugal - Perspectivas para o Sector*, Lisboa: GEPE - Gabinete de Estudos e Prospectiva Económica do Ministério da Economia, 2001.

[5] The Navigator Company, "História - The Navigator Company," [Online]. Available: http://www.thenavigatorcompany.com/Institucional/Historia. [Accessed 06 February 2018].

[6] RAIZ - Instituto de Investigação da Floresta e Papel, "RAIZ," [Online]. Available: http://raiz-iifp.pt/. [Accessed 07 February 2018].

[7] D. N. S. Hon and N. Shiraishi, Wood and Cellulosic Chemistry, New York, USA: Marcel Dekker, Inc., 2001.

[8] P. Bajpai, Environmentally friendly production of pulp and paper, Wiley, 2010.

[9] D. Pokhrel and T. Viraraghavan, "Treatment of pulp and paper mill waste water - a review," *Science of Total Environment,* pp. 37-58, 2004.

[10] M. C. Monte, E. Fuente, A. Blanco and C. Negro, "Waste management from pulp and paper production in the European Union," *Waste Management,* vol. 29, pp. 293-308, 2008.

[11] M. Kamali and Z. Khodaparast, "Review on recent developments on pulp and paper mill wastewater treatment," *Ecotoxicology and Environmental Safety,* vol. 114, pp. 326-342, 2014.

[12] O. Ashrafi, L. Yerushalmi and F. Haghighat, "Wastewater treatment in the pulp-and-paper industry: a review of the treatment processes and the associated greenhouse gas emission," *Journal of Environmental Management,* vol. 158, pp. 146-157, 2015.

[13] M. Suhr, G. Klein, I. Kourti, M. R. Gonzalo, G. G. Santonja, S. Roudier and L. D. Sancho, Best Available Techniques (BAT) Reference Document for the Production of Pulp, Paper and Board, Luxembourg: European Union, 2015.

[14] Official Journal of the European Union, Commission Implementing Decision of 26 September 2014, establishing the best available techniques (BAT) conclusions, under Directive 2010/75/EU of the European Parliament and of the Council, for the production of pulp, paper and board, 2014.

[15] D. V. Savant, R. Abdul-Rahman and D. R. Ranade, "Anaerobic degradation of adsorbable organic halides (AOX) from pulp and paper industry wastewater," *Bioresource Tchnology,* vol. 97, pp. 1092-1104, 2006.

[16] C. C. A. Loures, M. A. K. Alcântara, H. J. I. Filho, A. C. S. C. Teixeira, F. T. Silva, T. C. B. Paiva and G. R. L. Samanamud, "Advanced Oxidative Degradation Processes: Fundamentals

and Applications," *International Review of Chemical Engineering,* vol. 5, pp. 2035-1755, 2013.

[17] J. M. Poyatos, M. M. Muñio, M. C. Almecija, J. C. Torres, E. Hontoria and F. Osorio, "Advanced Oxidation Processes for Wastewater Treatment: State of the Art," *Water Air Soil Pollut,* vol. 205, pp. 187-204, 2010.

[18] P. Bajpai, Bleach Plant Effluents from the Pulp and Paper Industry, Punjab: Springer, 2013.

[19] H. J. H. Fenton, "Oxidation of tartaric acid in presence of iron," *Journal of the Chemistry Society,* vol. 65, pp. 899-910, 1894.

[20] C. Walling, "Fenton's Reagent Revisited," *Accounts of Chemical Research,* vol. 8, pp. 125-131, 1975.

[21] F. K. Ebru Cokay Catalkaya, "Color, TOC and AOX removals from pulp mill effluent by advanced oxidation processes - a comparative study," *Journal of Hazardous Materials,* vol. 139, pp. 244-253, 2007.

[22] N. Serpore and E. Pelizzetti, Photocatalysis: fundamentals and applications, John Wiley & Sons. Inc., 1989.

[23] A. Fujishima and K. Honda, "Eletrochemical Photolysis of Water at a Semiconductor Electrode," *Nature,* vol. 238, pp. 37-38, 1972.

[24] R. F. P. Nogueira and W. F. Jardim, "A Fotocatálise Heterogénea e sua Aplicação Ambiental," vol. 21, Julho 1998.

[25] A. L. Pruden and D. F. Ollis, "Degradation of chloroform by photoassisted heterogeneous catalysis in dilute aqueous suspensios of titanium dioxide," *Environmental Science & Technology,* vol. 10, pp. 628-631, 1983.

[26] A. L. Pruden and D. F. Ollis, "Photoassisted heterogeneous catalysis: The degradation of trichloroethylene in water," *Journal of Catalysis,* vol. 82, pp. 404-417, 1983.

[27] M. Schiavello, Heterogeneous Photocatalysis, vol. 3, Palermo, Italy: John Wiley & Sons. Ltd., 1997.

[28] Y. L. Pang, S. Lim, H. C. Ong and W. T. Chong, "Research progress on iron oxide-based magnetic materials: Synthesis techniques and photocatalytic applications," *Ceramics International,* vol. 42, pp. 9-34, 2016.

[29] M. Umar and H. A. Aziz, "Photocatalytic degradation of organic polutants in water," in *Organic Pollutants - monitoring, risk and treatment,* 2013, pp. 195-208.

[30] G. Sposito, "On Points of Zero Charge," *Environmental Science & Technology,* vol. 32, pp. 2815-2819, 1998.

[31] M. Perez, F. Torrades, J. Garcia-Hortal, X. Domenech and J. Peral, "Removal of organic contaminants in paper," *Journal of Photochemistry and Photobiology A: Chemistry,* vol. 109, pp. 281-286, 1997.

[32] M. Perez, F. Torrades, X. Domenech and J. Peral, "Removal of organic contaminants in paper pulp treatment effluents by TiO2 photocatalyzed oxidation" *Journal of Chemical Technology & Biotechnology,* vol. 77, pp. 525-532, 2002.

[33] A. Hakki, J. Scheider and D. Bahnemann, "Understanding the Chemistry of Photocatalytic Processes," in *Photocatalysis: Fundamentals and Perspectives*, Cambridge, The Royal Society of Chemistry, 2016.

[34] G. Rothenberg, Catalysis: Concepts and Green Applications, The Netherlands: Wiley- VCH, 2008.

[35] A. Khataee and G. A. Mansoori, Nanostructured Titanium Dioxide Materials: Properties, Preparation and Applications, World Scientific Publishing Company, 2011.

[36] Royal Society of Chemistry, *TiO2: Manufacture of titanium dioxide*, The Wolfson Foundation, 2017.

[37] Science Lab.com, *Material Safety Data Sheet: Titanium dioxide*, 2005.

[38] Evonik Industries, *Aeroxide, Aerodisp and Aeroperl, Titanium Dioxide as Photocatalyst - Technical Information 1243,* 2015.

[39] G. S. McNulty, "Production of Titanium Dioxide," in *Naturally Occurring Radioactive Material*, Seville, Spain, 2007.

[40] "Ink World Magazine," 22 09 2017. [Online]. Available: http://www.inkworldmagazine.com/issues/2017-11-01/view_breaking-news/global-forecast-to-2021-titanium-dioxide-market-by-grade-application-region/. [Accessed 14 April 2018].

[41] Grand View Research, "Titanium Dioxide (TiO2) Market Analysis By Application (Paints & Coatings, Plastics, Paper & Pulp, Cosmetics), By Region (North America, Europe, Asia Pacific, CSA, MEA), And Segment Forecasts, 2018 - 2025," 2017.

[42] R. J. Candal, J. Rodríguez, G. Colón, S. Gelover, E. V. Santos, A. J. González and M. A. Blesa, "Materiales para Fotocatálisis y Electrofotocatálisis," in *Eliminación de Contaminantes por Fotocatálisis Heterogénea*, 2001, pp. 143-163.

[43] A. Mills and S.-K. Lee, "A web-based overview of semiconductor photochemistry-based current commercial applications," *Journal of Photochemistry and Photobiology A: Chemistry*, vol. 152, pp. 233-247, 2002.

[44] J. Stráský, "Titanium and titanium alloys," [Online]. Available: http://slideplayer.com/slide/3446045/. [Accessed 15 June 2018].

[45] R. L. Pozzo, M. A. Baltanás and A. E. Cassano, "Supported titanium oxide as photocatalyst in water decontamination: State of the art," *Catalysis Today*, vol. 39, pp. 219-231, 1997.

[46] D. C. Botía, M. S. Rodríguez and V. M. Sarria, "Evaluation of UV/TiO2 and UV/ZnO photocatalytic systems coupled to a biological process for the treatment of bleaching pulp mill effluent," *Chemosphere*, vol. 89, pp. 732-736, 2012.

[47] A. M. Peiró, E. Brillas, J. Peral, X. Domènech and J. A. Ayllón, "Electrochemically assisted deposition of titanium dioxide on aluminium cathods," *Journal of Material Chemistry*, vol. 12, pp. 2769-2773, 2002.

[48] A. Bozzi, I. Guasaquillo and J. Kiwi, "Accelerated removal of cyanides from industrial effluents by supported TiO2 photo-catalysts," *Applied Catalysis B: Environmental*, vol. 51, pp. 203-211, 2004.

[49] M.-J. López-Muñoz, R. v. Grieken, J. Aguado and J. Marugán, "Role of the support on the activity of silica-supported TiO2 photocatalysts: Structure of the TiO2/SBA-15 photocatalysts," *Catalysis Today,* vol. 101, pp. 307-314, 2005.

[50] X. Tang, Q. Feng, K. Liu, X. Luo, J. Huang and Z. Li, "A simple and innovative route to remarkably enhance the photocatalytic performance of TiO2: Using micro-meso porous silica nanofibers as carrier to support highly-dispersed TiO2 nanoparticles," *Microporous and Mesoporous Materials,* vol. 258, pp. 251-261, 2018.

[51] M. R. Dhananjeyan, J. Kiwi and K. R. Thampi, "Photocatalytic performance of TiO2 and Fe2O3 immobilized on derivatized polymer films for mineralisation of pollutants," *Chemical Communications,* pp. 1443-1444, 2000.

[52] J. Gómez-Pastora, S. Dominguez, E. Bringas, M. J. Rivero, I. Ortiz and D. D. Dionysiou, "Review and perspectives on the use of magnetic nanophotocatalysts (MNPCs) in water treatment," *Chemical Engineering Journal,* vol. 310, pp. 407-427, 2017.

[53] V. Nogueira, I. Lopes, T. A. P. Rocha-Santos, F. Gonçalves and R. Pereira, "Treatment of ral industrial wasteqaters through nano-TiO2 and nano-Fe2O2 photocaralysis: case study of mining and kraft pulp mill effluents," *Environmental Technology,* vol. 39, pp. 1586-1596, 2018.

[54] R. E. Kalan, S. Yaparatne, A. Amirbahman and C. P. Tripp, "P25 titanium dioxide coated magnetic particles: Preparation,characterization and photocatalytic activity," *Applied Catalysis B: Environmental,* vol. 187, pp. 249-258, 2016.

[55] P. M. Álvarez, J. Jaramillo, F. López-Piñero and P. K. Plucinski, "Preparation and characterization of magnetic TiO2 nanoparticles and their utilization for the degradation of emerging pollutants in water," *Applied Catalysis B: Environmental,* vol. 100, pp. 338-345, 2010.

[56] R. M. Novais, M. P. Seabra and J. A. Labrincha, "Porous geopolymer spheres as novel pH buffering materials," *Journal of Cleaner Production,* vol. 143, pp. 1114-1122, 2017.

[57] T. Polónio, *Tratamento de Efluentes da Indústria de pasta Kraft,* Universidade de Aveiro, 2016.

[58] Photochemical Reactors Ltd, [Online]. Available: http://www.photochemicalreactors.co.uk/html/contact-us.html. [Accessed 17 May 2018].

[59] Technical Committee ISO/TC 147, Water quality, "ISO 9562:2004 - Water quality, Determination of adsorbable organically bound halogens (AOX)," International Organization for Standardization, 2004.

[60] J. I. Langford and D. Louer, "Powder Diffraction," *Reports on Progress in Physics,* vol. 59, pp. 131-234, 1996.

[61] M. Wagemaker, G. J. Kearley, A. A. Van Well and H. Mutka, "PDF-4+: Anatase (04-014-8515)," ICDD - International Centre for Diffraction Data, 2018.

[62] G. Greenwood, "PDF-4+: Rutile (04-004-4338)," ICDD - International Centre for Diffraction Data, 2018.

[63] R. Ueda and K. Hasegawa, "PDF-4+: Magnetite (04-006-6550)," ICDD - International Centre for Diffraction Data, 2018.

[64] W. M. Doyle, *Principles and Applications of Fourier Transform Infrared (FTIR) Process Analysis*, Hellma Axiom, Inc..

[65] D. S. Tavares, A. L. Daniel-da-Silva, C. B. Lopes, N. J. O. Silva, V. S. Amaral, J. Rocha, E. Pereira and T. Trindade, "Efficient sorbents based on magnetite coated with siliceous hybrid shells for removal of mercury ions," *Journal of Materials Chemistry A*, vol. 1, pp. 8134-8143, 2013.

[66] L. Rodrigues, C. Dias, H. Ceragioli, A. Rodas, F. Monteiro and C. Zavaglia, "FTIR Analysis and Cytotoxicity Test of Titanium Dioxide Nanoparticles," *Key Engineering Materials*, Vols. 493-494, pp. 768-774, 2012.

[67] H.-H. Perkampus, UV-VIS Spectroscopy and Its Applications, Springer-Verlag, 1992.

[68] D. B. Williams and C. B. Carter, Transmission Electron Microscopy - A Textbook for Materials Science, Springer Science & Business Media, 2009.

[69] E. N. Caspi, B. Pokroy, P. L. Lee, J. P. Quintana and E. Zolotoyabko, "PDF-4+: Quartz (04-012-0490)," ICDD - International Centre for Diffraction Data, 2018.

[70] F. Gillery, "PDF-4+: Muscovite-2M1 (00-006-0263)," ICDD - International Centre for Diffraction Data, Penn State Univ., University Park, PA, USA, 2018.

[71] E. N. Caspi, B. Pokroy, P. L. Lee , J. P. Quintana and E. Zolotoyabko, "PDF-4+: Calcite (00-005-0586)," ICDD - International Centre for Diffraction Data, 2018.

[72] M. Van Meerssche, J. M. Dereppe and P. W. Lobo, "PDF-4+: Trona (04-010-0700)," ICDD - International Centre for Diffraction Data, 2018.

[73] H. Boke, S. Akkurt, S. Ozdemir, E. H. Gokturk and E. N. C. Saltik, "Quantification of CaCO3-CaSO3.0.5H2O-CaSO4-2H2O mixtures by FTIR analysis and its ANN model," *Materials letters*, vol. 58, pp. 723-726, 2004.

[74] K. Djebaili, Z. Mekhalif, A. Boumaza and A. Djelloul, "XPS, FTIR, EDX and XRD analysis of Al2O3 scales grown on PM2000 Alloy," *Journal of Spectroscopy*, p. 16, 2015.

[75] R. K. Nariyal, P. Kothari and B. Bisht, "FTIR Measurements of SiO2 Glass Prepared by Sol-Gel Technique," *Chemical Science Transactions*, vol. 3, pp. 1064-1066, 2004.

[76] L. Reimer, Scanning Electron Microscopy, Berlin Heidelberg: Springer-Verlag , 1985.

[77] D. Beydoun, R. Amal, G. K.-C. Low and S. McEvoy, "Novel Photocatalyst: Titania-Coated Magnetite. Activity and Photodissolution," *The Journal of Physical Chemistry*, vol. 104, pp. 4387-4396, 2000.

[78] M. C. Yeber, J. Rodríguez, J. Freer, N. Durán and H. D. Mansilla, "Photocatalytic degradation of cellulose bleaching effluent by supported TiO2 and ZnO," *Chemosphere*, vol. 41, pp. 1193-1197, 2000.

Appendix A - Materials characterization

a) Ultraviolet-visible spectroscopy

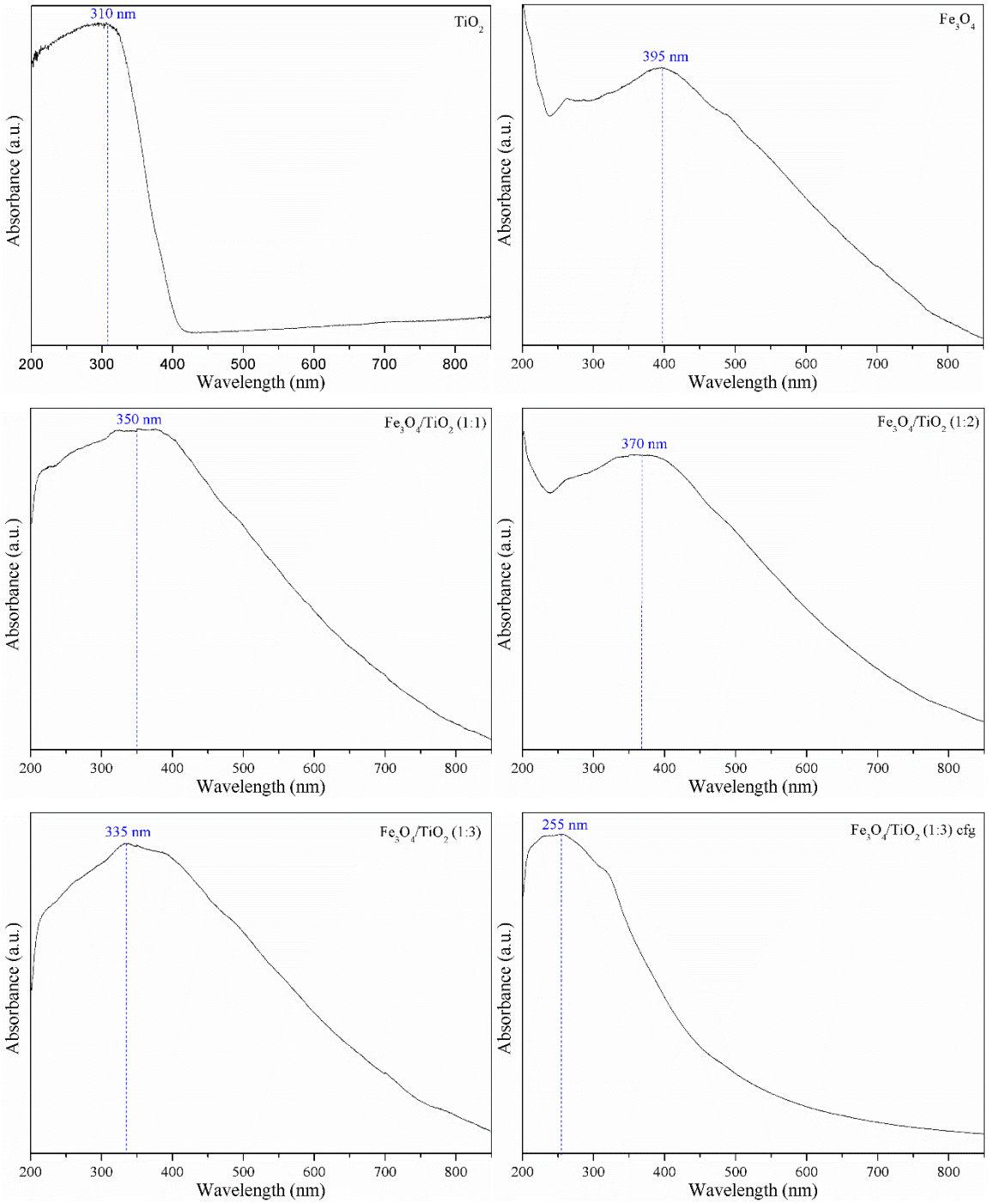

Figure A. 1 - UV-vis spectra of TiO_2 and all the magnetic nanoparticles prepared.

b) Transmission Electron Microscopy

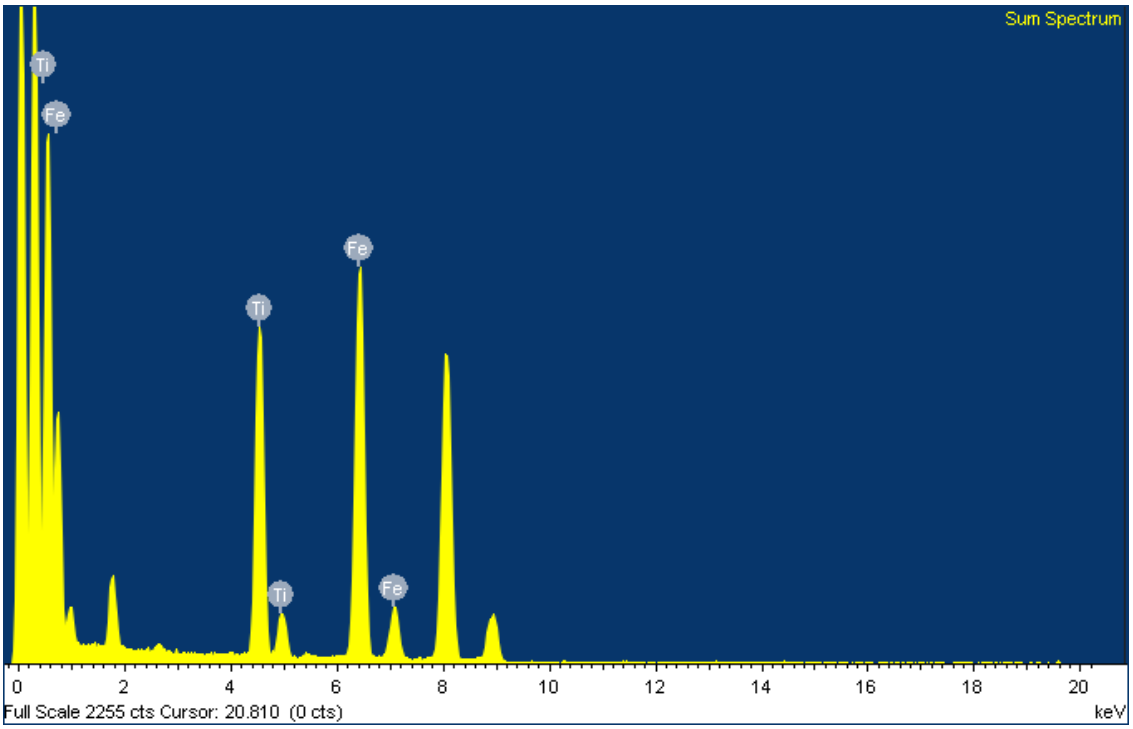

Figure A. 2 – EDS spectrum of the sample Fe_3O_4 /TiO_2 (1:3).

Appendix B - Photocatalysis conditions

Monitoring of the temperatures

Table B. 1 - Register of the temperatures of the effluent, during the photocatalytic tests. The numbers in red represent the temperatures below of the defined interval (57-60°C).

Test	Start time	End time		Test time (min)							
				0	5	10	20	30	40	50	60
1	11:21	12:21		50.3	55.5	56.5	57.6	57.6	57.7	57.6	57.6
2	15:40	16:40		50.4	55.4	56.3	56.3	57.2	57.4	57.2	57.4
3	15:30	16:30		50.5	56.2	56.4	57.3	57.2	57.4	57.4	57.0
4	11:20	12:20		50.5	55.6	56.4	56.4	57.2	56.5	57.4	57.8
5	11:22	12:22		20.1	56.2	56.8	57.6	57.4	57.4	57.5	57.2
6	11:00	12:00		50.1	55.5	56.9	57.3	57.2	57.4	57.4	57.4
7	11:32	12:32		50.5	54.9	57.0	57.2	57.2	57.0	57.2	57.2
8	15:00	16:00		50.4	54.3	56.4	57.3	57.1	57.3	57.2	57.3
9	11:30	12:30		49.7	50.9	53.5	56.4	57.4	57.4	57.4	57.3
10	16:00	17:00		50.4	50.9	56.0	57.0	57.5	57.4	57.4	57.4
11	14:14	15:14		50.3	50.8	53.0	53.9	55.3	58.0	57.2	57.4
12	11:30	12:30		50.1	50.4	54.5	56.0	57.7	57.7	57.7	57.6
13	15:30	16:30		50.3	52.0	55.1	56.4	57.4	57.0	57.1	57.1
14	10:55	11:55		49.9	50.6	56.5	56.5	57.2	57.2	57.2	57.2
15	10:30	11:30		50.0	50.5	53.4	55.3	56.7	57.7	57.7	57.7
16	14:55	15:55		50.4	50.6	55.3	56.7	57.4	57.4	57.5	57.6
17	15:20	16:20		50.1	54.0	56.7	57.7	57.7	57.7	57.7	57.8
18	11:20	12:20		50.2	54.5	55.9	57.0	57.4	57.3	57.6	57.8
19	11:15	12:15		49.8	54.5	56.5	57.8	56.5	57.9	58.2	58.1
20	15:35	16:35		50.4	54.6	56.5	57.3	59.0	59.8	59.9	59.5
21	10:40	11:40		49.8	53.3	54.3	55.9	56.4	57.4	57.4	57.6
22	14:50	15:50		48.2	51.5	54.8	55.0	56.1	57.0	57.1	57.2
23	11:30	12:30		50.0	58.6	59.3	60.1	57.8	57.6	57.6	58.0
24	15:30	16:30		50.0	55.8	55.3	55.8	57.1	56.4	57.0	57.1
25	11:18	12:18		51.9	56.3	57.4	57.2	57.2	57.4	57.5	57.4
26	15:23	16:23		50.4	52.6	55.3	56.0	57.9	57.7	57.5	57.2
27	11:20	12:20		50.2	54.5	55.9	57.0	57.4	57.3	57.6	57.8

Table B. 2 - Register of the temperatures of the bath heating, during the photocatalytic test.

Test	Test time (min)							
	0	5	10	20	30	40	50	60
1	52.0	52.5	53.0	53.0	53.0	53.0	53.0	53.0
2	52.0	52.5	53.0	53.5	53.5	53.5	53.5	53.5
3	52.0	52.5	53.0	53.0	53.0	53.0	53.0	53.0
4	52.0	52.0	52.5	53.0	53.0	53.5	53.5	53.5
5	52.0	53.0	53.5	53.5	53.5	53.5	53.5	53.5
6	52.0	53.5	54.0	54.0	54.0	54.0	54.0	54.0
7	52.0	54.0	54.0	54.0	54.0	54.0	54.0	54.0
8	52.0	53.5	54.5	54.5	54.5	54.5	54.5	54.5
9	52.0	55.0	58.0	59.0	59.0	59.0	59.0	59.0
10	52.0	58.0	59.0	59.0	59.0	59.0	59.0	59.0
11	52.0	55.0	55.5	58.0	60.0	59.0	59.0	59.0
12	52.0	56.0	58.0	59.0	59.0	59.0	59.0	59.0
13	52.0	58.0	58.0	58.5	58.5	58.5	58.5	58.5
14	52.0	58.0	58.0	58.5	58.5	58.5	58.5	58.5
15	52.0	55.0	57.0	58.5	59.5	59.5	59.5	59.5
16	52.0	58.0	58.5	59.0	59.0	59.0	59.0	59.0
17	52.0	54.0	55.0	55.0	55.0	55.0	55.0	55.0
18	52.0	53.0	54.0	54.0	54.0	54.0	54.0	54.0
19	52.0	54.0	55.0	55.0	56.0	56.0	56.0	56.0
20	52.0	54.0	55.0	55.0	55.0	55.0	54.5	54.5
21	52.0	54.0	56.0	56.5	56.5	56.5	56.5	56.5
22	52.0	56.0	58.0	59.0	59.0	59.0	59.0	59.0
23	52.0	52.0	52.0	51.0	51.0	51.0	51.0	51.0
24	52.0	52.0	52.5	54.0	54.0	55.0	55.0	55.0
25	52.0	53.0	53.0	53.0	53.0	53.0	53.0	53.0
26	52.0	55.0	56.0	58.0	58.0	58.0	58.0	58.0
27	52.0	53.0	54.0	54.0	54.0	54.0	54.0	54.0

Experimental conditions of the tests with the photocatalysts recovered

In most of the photocatalytic experiments it was not possible to recover the total amount of catalyst. To test the reuse of the recovered catalysts it was necessary to adjust the volume of effluent and H_2O_2 in order to keep the same experimental conditions. The volumes were calculated based on the initial mass of the first photocatalytic test, test from Set A (test A), and the initial mass of the photocatalytic test performed with recovered photocatalyst, test from Set C (test C), according to the Equations (B.1) and (B.2).

Note that $V_{effluent,test\ A}$ = 200 mL and $V_{H_2O_2,test\ A}$ = 1.00 mL for the all tests. And the new conditions obtained are registered on the Table B. 3.

$$V_{effluent,test\ C}(mL) = V_{effluent,test\ A}(mL) \times \frac{m_{initial,test\ C}(g)}{m_{initial,test\ A}(g)} \quad (B.1)$$

$$V_{H_2O_2,test\ C}(mL) = V_{H_2O_2,test\ A}(mL) \times \frac{m_{initial,test\ C}(g)}{m_{initial,test\ A}(g)} \quad (B.2)$$

Table B. 3 - Conditions of the tests performed with the photocatalysts recovered.

Test	$m_{initial,test\ A}(g)$	$m_{initial,test\ C}(g)$	$V_{effluent,test\ C}$ (mL)	$V_{H_2O_2,test\ C}$ (mL)
19	0.205	0.162	158	0.79
20	0.206	0.125	121	0.61
21	0.203	0.121	119	0.60
22	0.203	0.075	74	0.37
23	0.209	0.108	103	0.52
24	2.014	1.993	198	0.99
25	2.015	2.012	200	1.00

Appendix C - Photocatalysis results

Register of the samples of effluent taken from each test

For each test, pictures of the effluent at three different treatment stages are shown: untreated effluent, effluent after addition of H_2O_2 and effluent after 1h treatment (from left to right).

a) Set A (tests performed with the initial photocatalysts and with UV radiation)

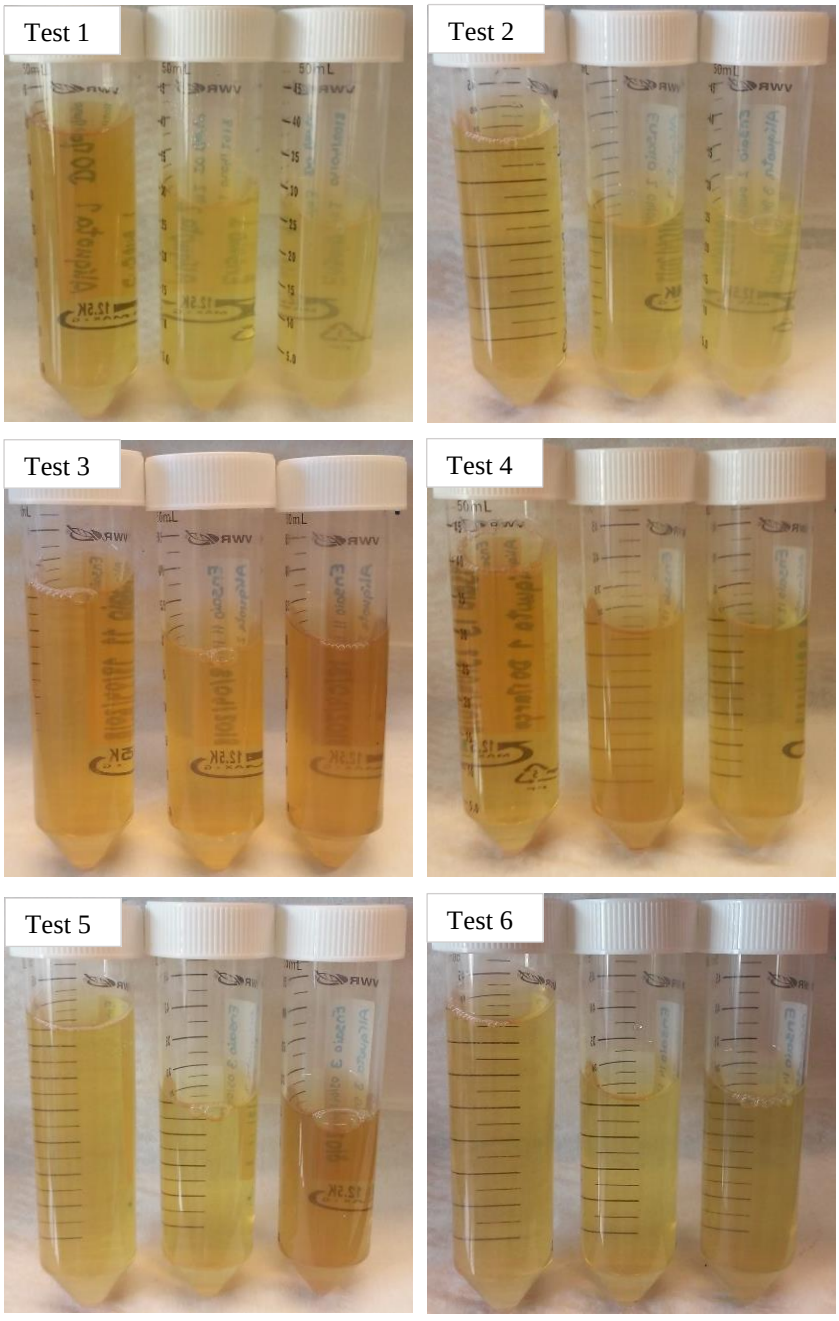

Figure C. 1 - Register of the visual aspect of the aliquots taken from tests 1-6 (Set A)

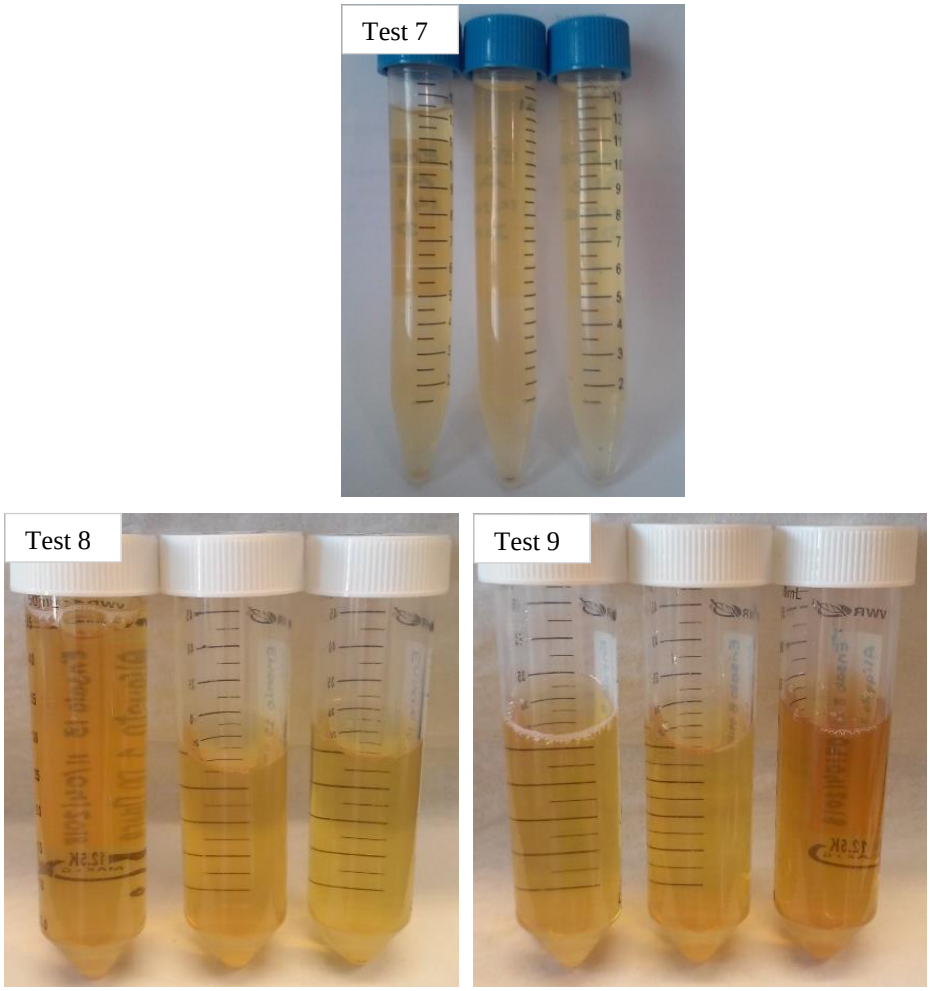

Figure C. 2 - Register of the visual aspect of the aliquots taken from tests 7-9 (Set A).

b) Set B (tests performed with the initial photocatalysts and without UV radiation)

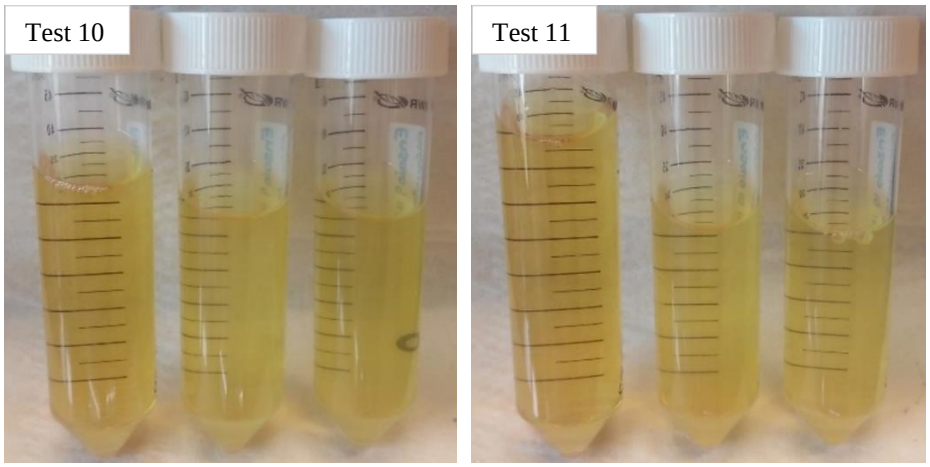

Figure C. 3 - Register of the visual aspect of the aliquots taken from tests 10-11 (Set B).

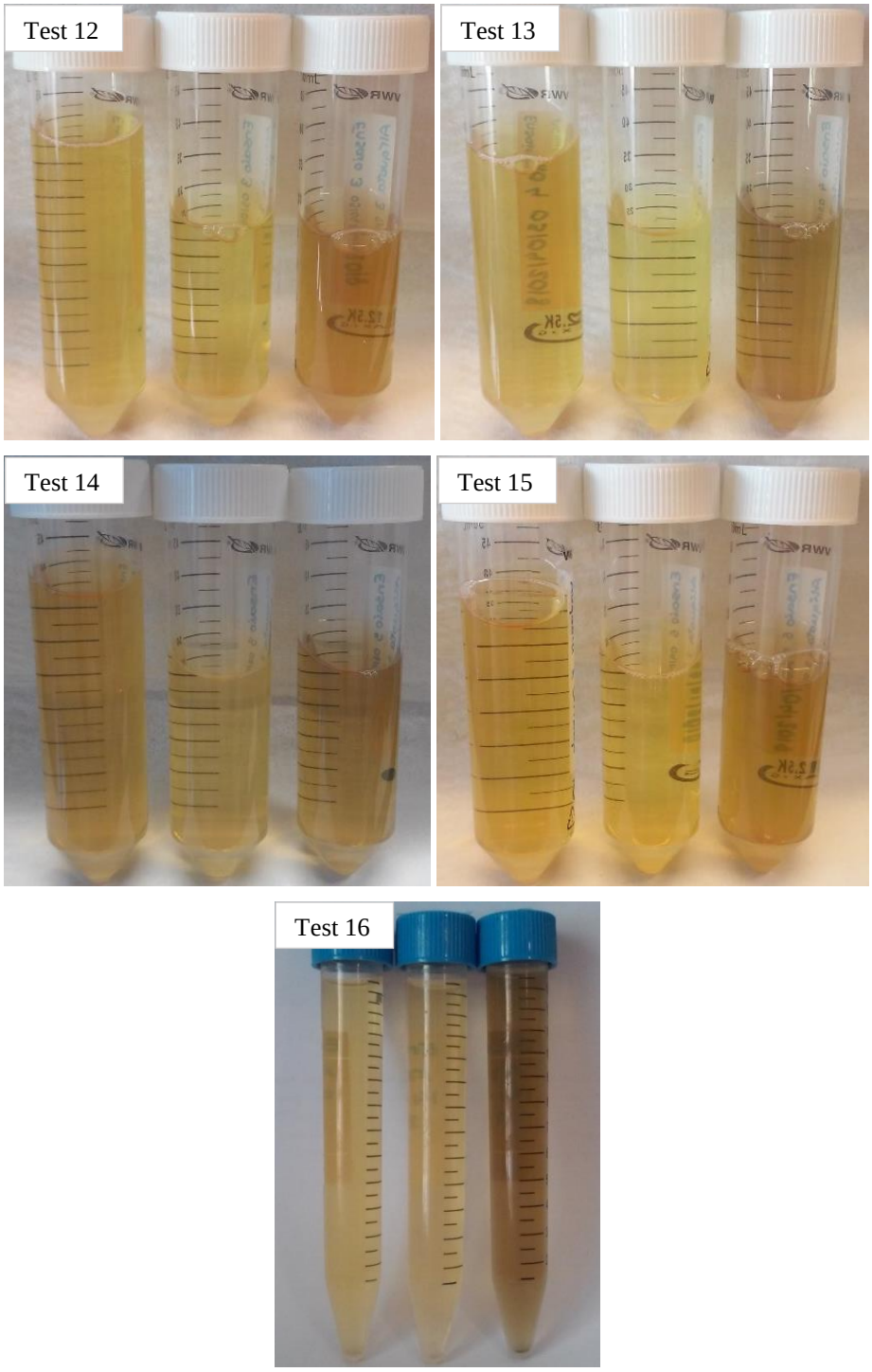

Figure C. 4 - Register of the visual aspect of the aliquots taken from tests 12-16 (Set B).

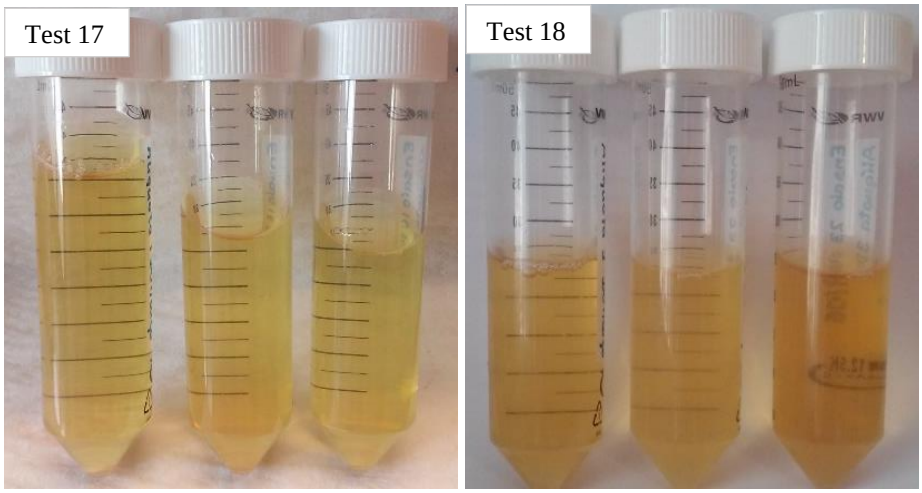

Figure C. 5 - Register of the visual aspect of the aliquots taken from tests 17-18 (Set B).

c) Set C (tests performed with the recovered photocatalysts, from Set A, and with UV radiation)

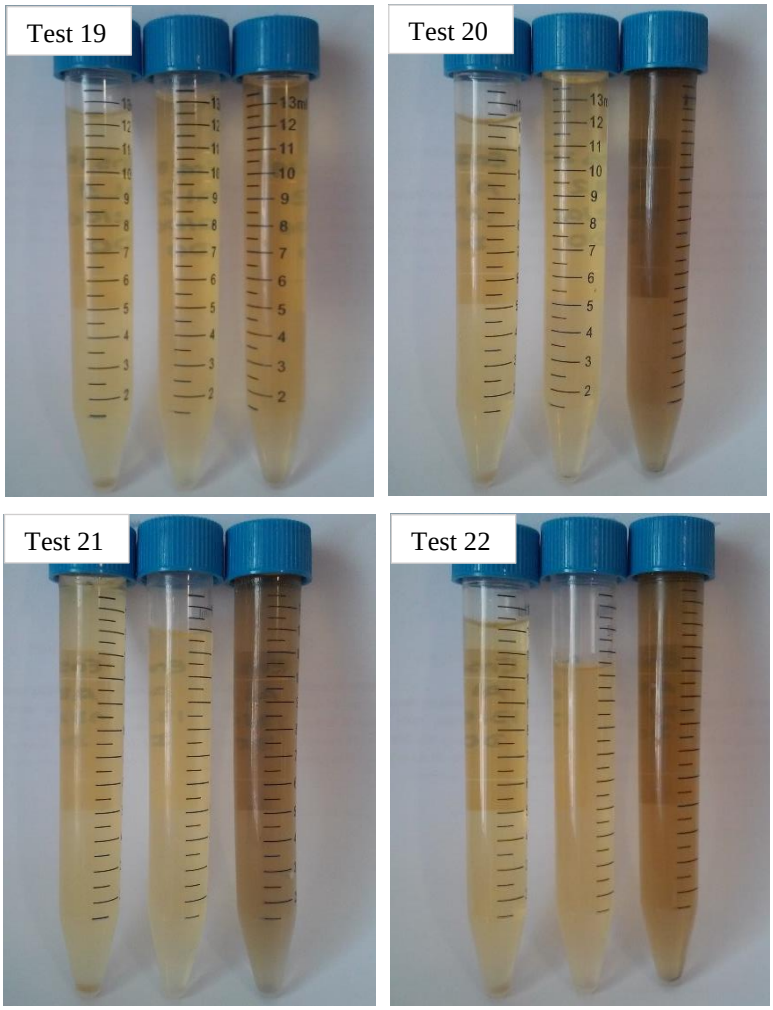

Figure C. 6 - Register of the visual aspect of the aliquots taken from tests 19-22 (Set C).

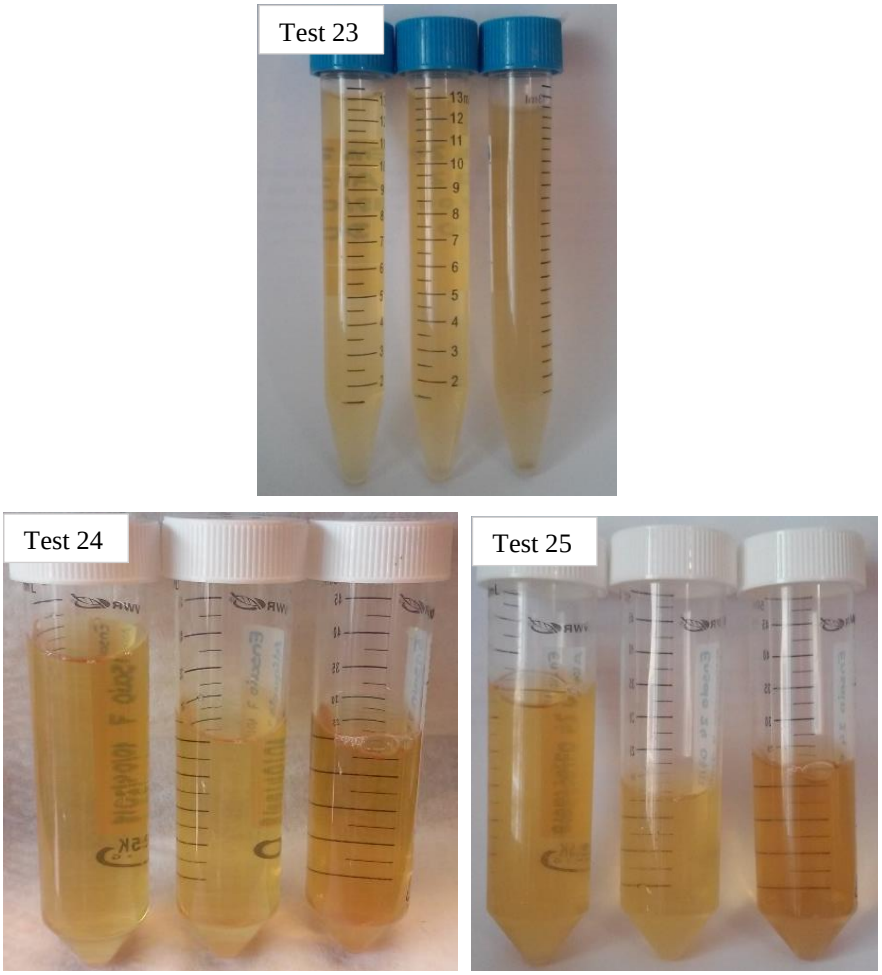

Figure C. 7 - Register of the visual aspect of the aliquots taken from tests 23-25 (Set C).

d) Set D (tests performed without photocatalyst and with UV radiation)

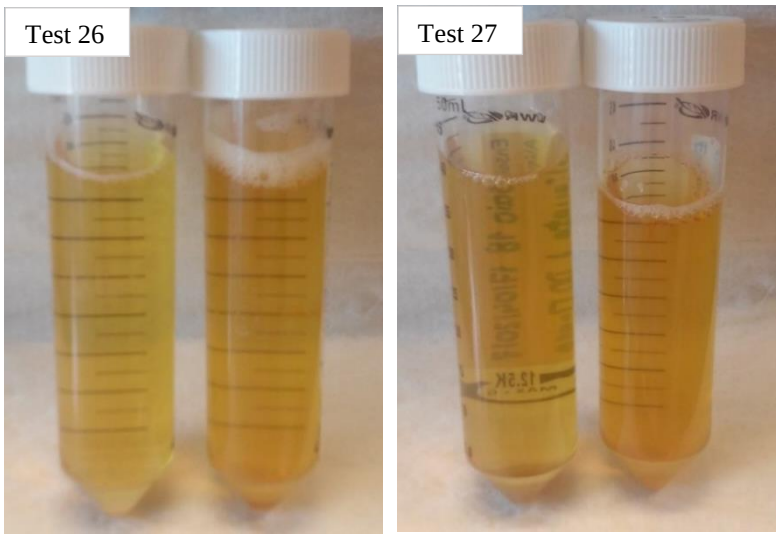

Figure C. 8 - Register of the visual aspect of the aliquots taken from tests 26-27 (Set D).

Removal of AOX

The removal of AOX was calculated with the concentration of AOX in the sample of pure effluent, sample 1, and the concentration of AOX on the sample n, according to the Equation (C.1). If the purpose is to calculate the percentage of AOX removed after adding H_2O_2, sample n it is the sample 2. But, if the purpose it is calculate the percentage of AOX removed after 1 hour of photocatalysis, sample n corresponds to the sample 3. The results are presented on the Table C. 1.

Note for the tests 17 and 18, there was not taken an aliquot after adding H_2O_2.

$$\text{Removal of AOX (\%)} = \frac{[\text{AOX}]_{\text{sample n}} - [\text{AOX}]_{\text{sample 1}}}{[\text{AOX}]_{\text{sample 1}}} \times 100 \qquad \text{(C.1)}$$

Table C. 1 - Concentration of AOX in each sample taken from each test and the respective percentages of AOX removal.

	[AOX] (mg·L^{-1})			Removal of AOX (%)	
	Sample 1	Sample 2	Sample 3	After adding H_2O_2	After 1 hour
1	104	86	26	17.3	74.9
2	103	85	24	17.0	76.6
3	106	79	36	25.6	66.4
4	102	78	30	23.6	70.2
5	119	87	36	26.3	69.7
6	111	91	45	17.8	59.0
7	120	93	32	22.5	73.3
8	110	88	38	19.5	65.2
9	111	96	35	13.5	68.9
10	120	93	66	22.7	44.8
11	112	94	76	15.8	32.3
12	110	88	62	20.0	43.6
13	120	86	66	28.3	45.0
14	110	88	59	20.0	46.4
15	120	98	62	18.3	48.3
16	120	95	77	20.8	35.8
17	115	93	64	18.7	44.0
18	110	100	81	9.1	26.4
19	120	110	61	8.3	49.2
20	120	95	29	20.8	75.8

Test	[AOX] (mg·L^{-1})			Removal of AOX (%)	
	Sample 1	Sample 2	Sample 3	After adding H_2O_2	After 1 hour
21	110	94	28	14.5	74.5
22	120	87	66	27.5	45.0
23	120	95	34	20.8	71.7
24	110	90	44	18.2	60.0
25	110	95	38	13.6	65.5
26	116	-	79	-	32.1
27	118	-	80	-	32.1

Variation of the pH value

In the way to calculate the variation of the pH of the effluent during the photocatalytic tests, there was used the Equation (C.2), which allows to obtain the values present on the Table C. 2.

$$\text{pH variation (\%)} = \frac{\text{pH}_{\text{after test}} - \text{pH}_{\text{before test}}}{\text{pH}_{\text{before test}}} \times 100 \qquad \text{(C.2)}$$

Table C. 2 - Register of the pH values before and after the photocatalytic tests.

Test	pH		pH variation (%)
	Before test	After test	
1	2.104	2.347	11.6
2	2.100	2.555	21.7
3	2.065	2.450	18.6
4	2.076	2.656	27.9
5	2.150	3.110	44.7
6	2.166	3.000	38.5
7	2.139	2.794	30.6
8	2.154	3.914	81.7
9	2.164	3.994	84.6
10	2.180	2.828	29.7
11	2.179	2.992	37.3
12	2.106	3.497	66.1
13	2.166	3.410	57.4
14	2.157	3.250	50.7

Test	pH		pH variation (%)
	Before test	After test	
15	2.168	2.604	20.1
16	2.142	2.490	16.3
17	2.160	3.613	67.3
18	2.170	3.350	54.4
19	2.135	2.189	2.53
20	2.130	2.575	20.9
21	2.115	2.702	27.8
22	2.136	2.652	24.6
23	2.146	2.503	16.6
24	2.152	2.807	30.4
25	2.140	3.137	46.6
26	2.177	2.186	0.41
27	2.180	2.219	1.79

Appendix D - Recovery of the photocatalysts

To determine the weight percentage of recovery of each photocatalyst, it was used the Equation (D.1). Note when the photocatalyst used was TiO_2 P25 non-supported, it was not recovered.

$$\text{Weight recovery (\%)} = \frac{m_{initial} - m_{final}}{m_{initial}} \times 100 \quad \text{(D.1)}$$

Table D. 1 - Initial and final mass of each photocatalyst, when applied, and the weight recovery percentage.

Test	$m_{initial}$ (g)	m_{final} (g)	Weight recovery (%)
1	0.201	-	-
2	0.204	-	-
3	0.205	0.170	82.9
4	0.206	0.135	65.5
5	0.203	0.129	63.5
6	0.203	0.081	39.9
7	0.209	0.113	54.1
8	2.014	1.993	99.0
9	2.015	2.012	99.9
10	0.208	-	-
11	0.206	-	-
12	0.208	0.203	97.6
13	0.206	0.197	95.6
14	0.209	0.199	95.2
15	0.206	0.180	87.4
16	0.204	0.194	95.1
17	2.019	2.002	99.2
18	2.021	2.019	99.9
19	0.162	0.14	86.4
20	0.125	0.075	60.0
21	0.121	0.066	54.5
22	0.075	0.038	50.7
23	0.108	0.02	18.5
24	1.993	1.626	81.6
25	2.012	1.807	89.8
26	-	-	-
27	-	-	-

D.1 - Magnetic nanoparticles

c) Visual appearance

Sets A and B

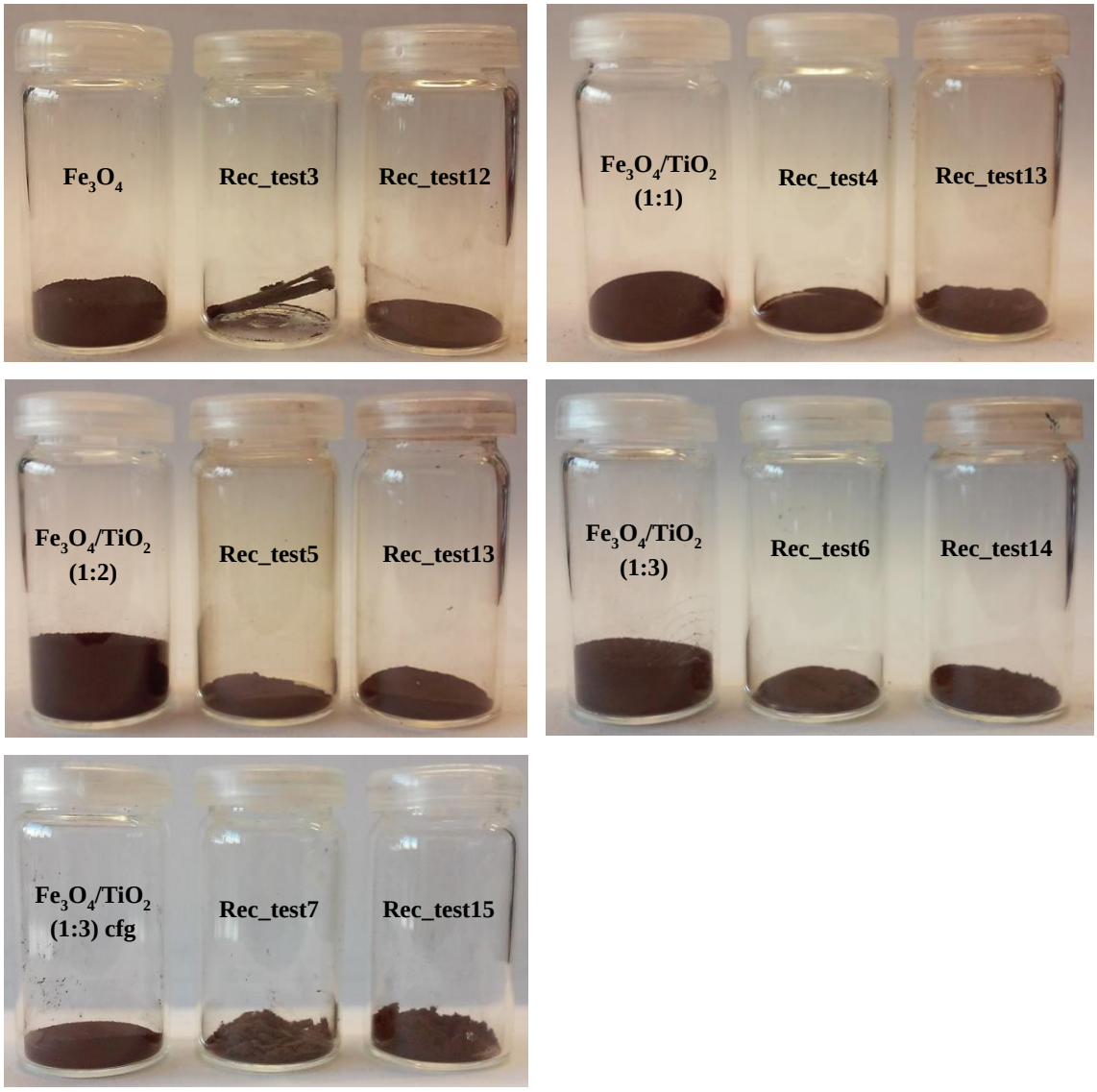

Figure D. 1 – Photography of the magnetic nanoparticles before and after the photocatalytic treatment, Sets A and B.

Set C

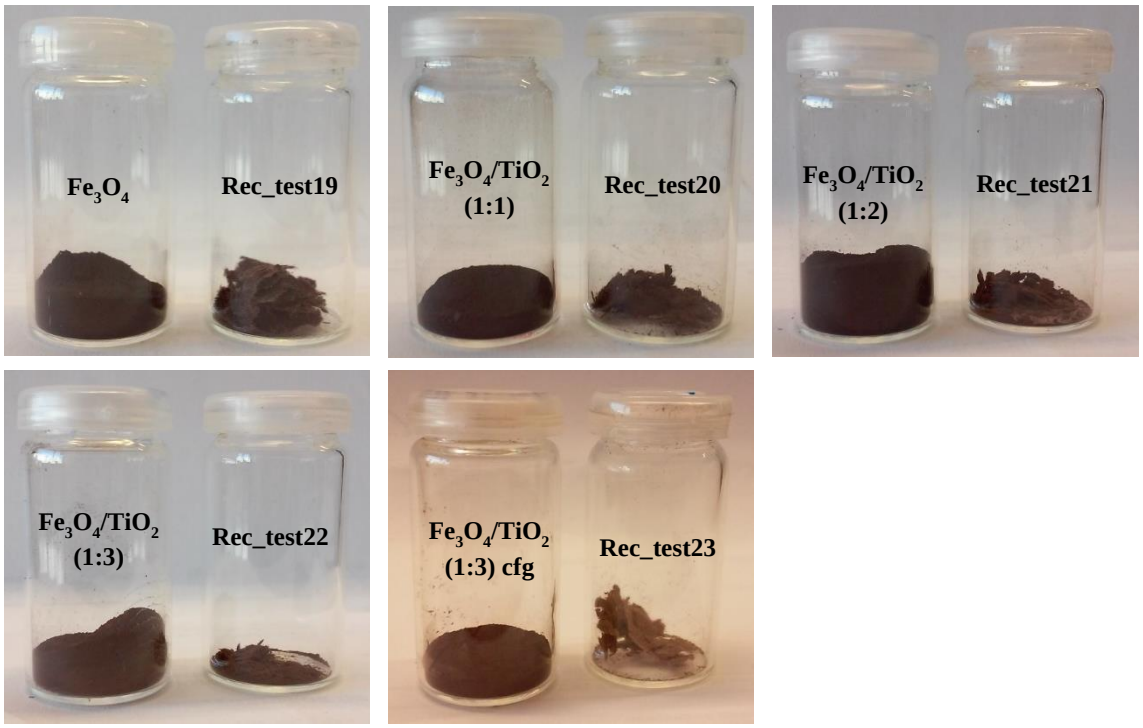

Figure D. 2 - Photography of the magnetic nanoparticles before and after the photocatalytic treatment, Set C.

d) X-Ray powder diffraction

Sets A and B

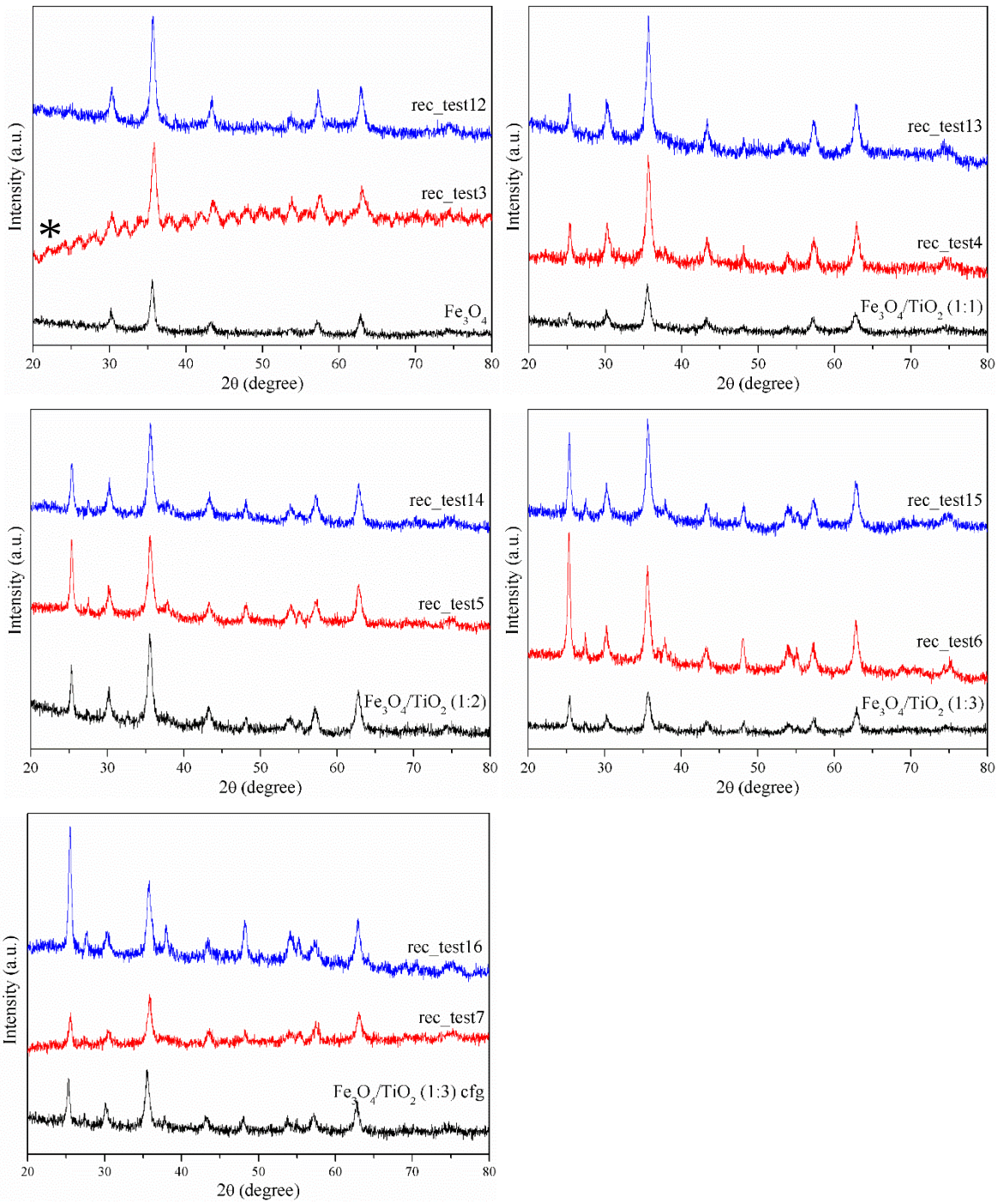

*Figure D. 3 - Diffractogram of XRD of all the magnetic nanoparticles prepared (black line) and after the test of Set A (red line) and Set B (blue line). *Poor quality diffractogram.*

Set C

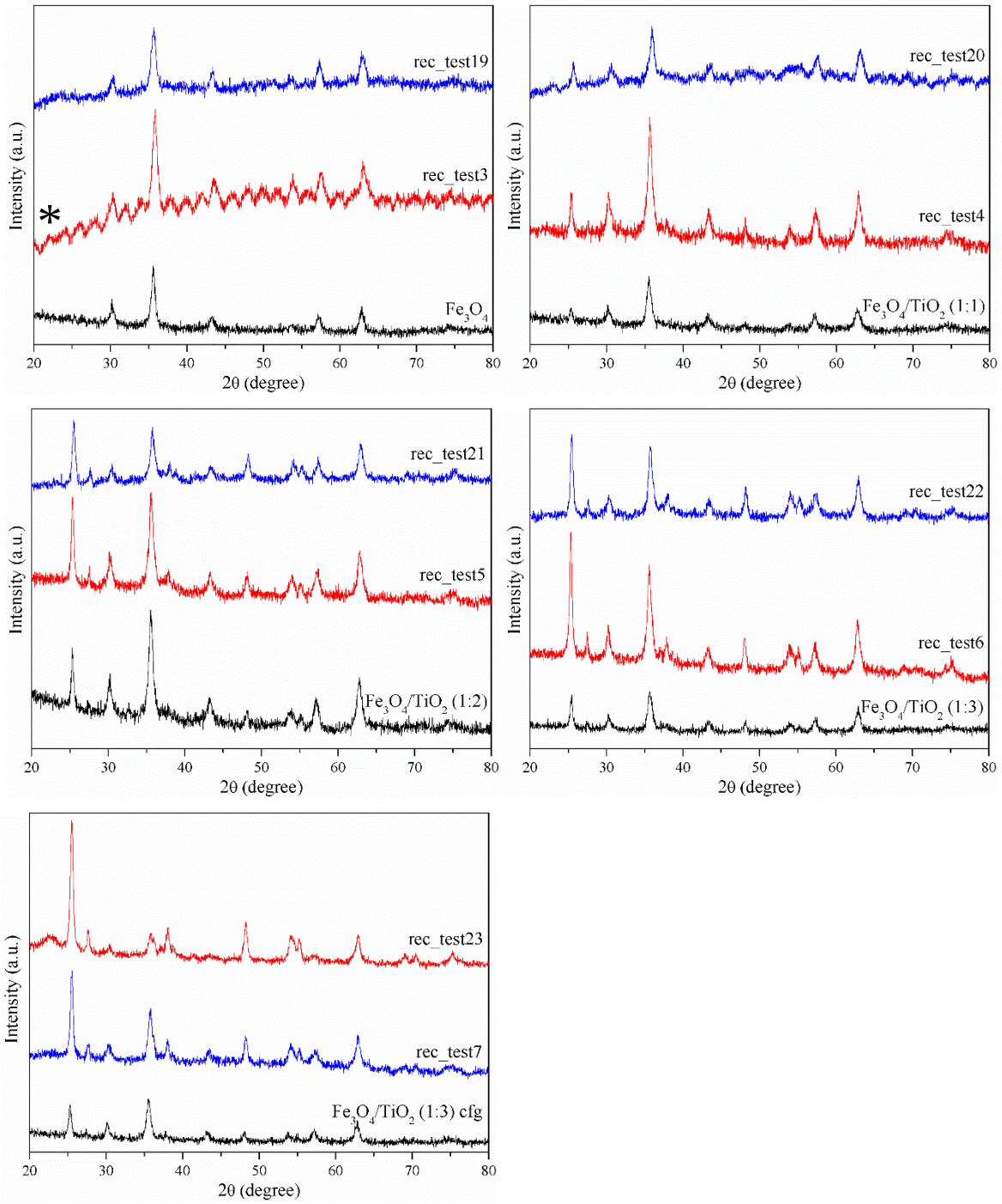

*Figure D. 4 – XRD diffractogram of XRD of all the magnetic nanoparticles prepared (black line) and after the test of Set A (red line) and Set C (blue line). * Poor quality diffractogram.*

e) Fourier-transformed infrared spectroscopy

Sets A and B

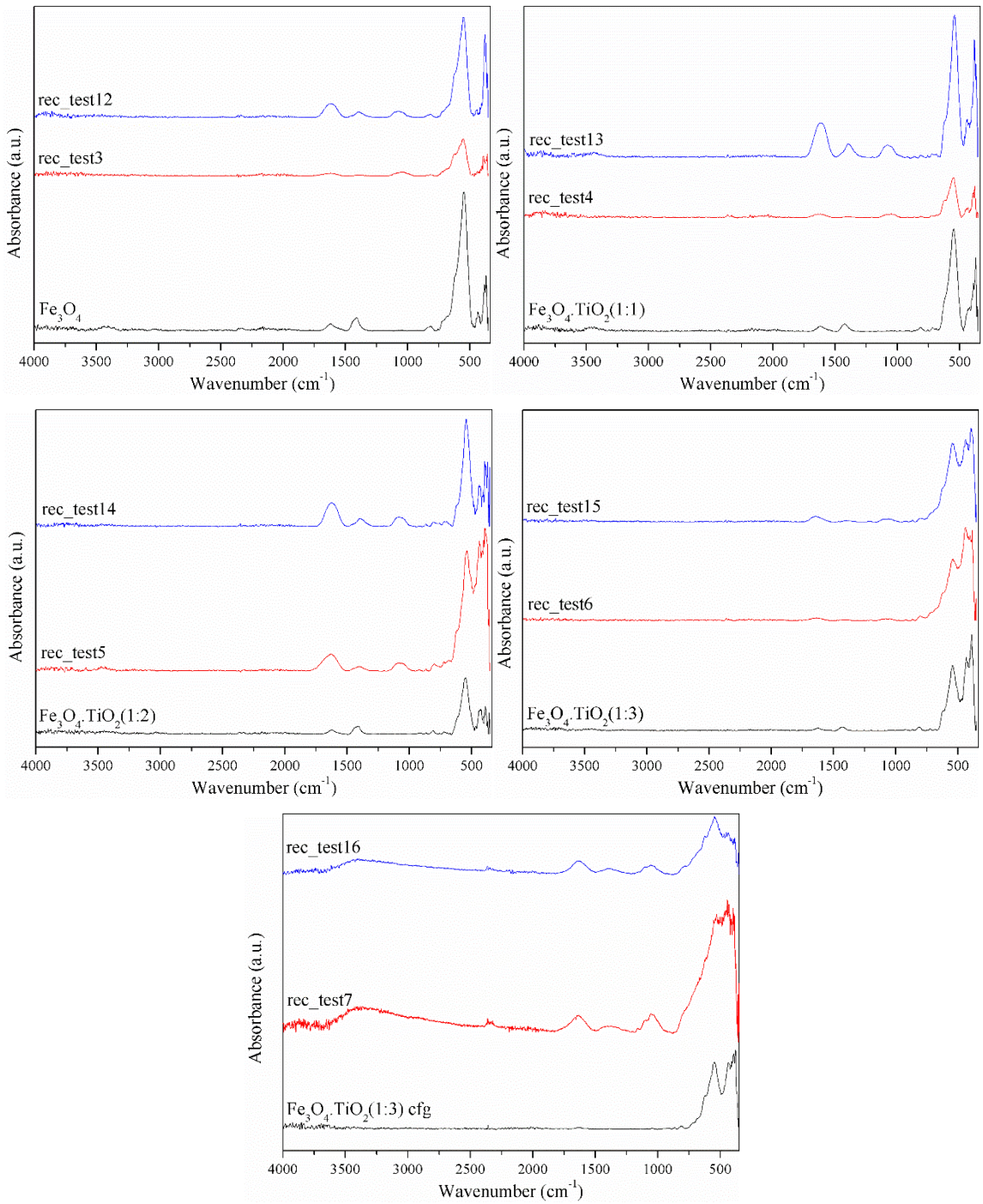

Figure D. 5 - FTIR spectra of all the magnetic nanoparticles prepared (black line) and after the test of Set A (red line) and Set B (blue line).

Set C

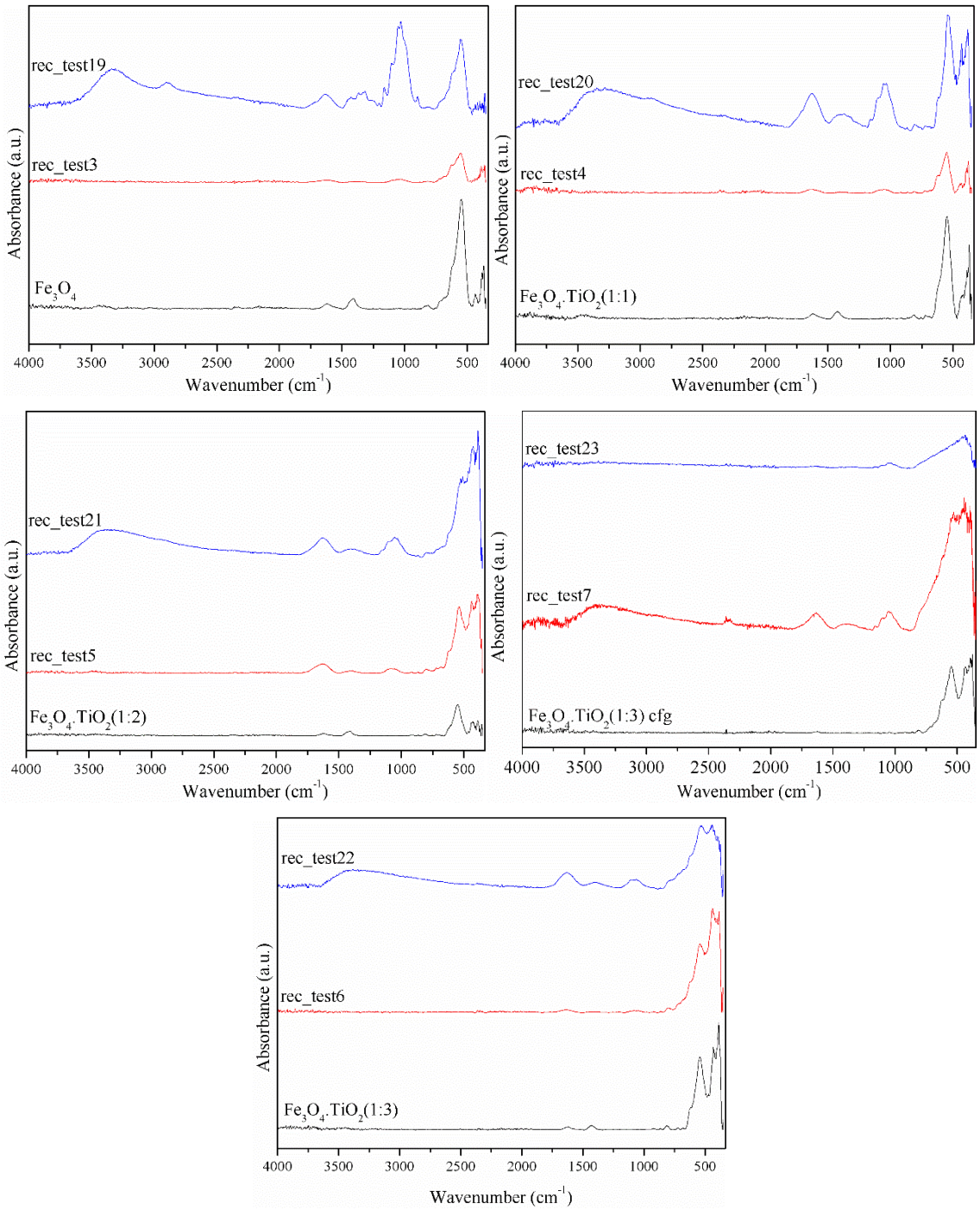

Figure D. 6 – FTIR spectra of all the magnetic nanoparticles prepared (black line) and after the test of Set A (red line) and Set C (blue line).

f) Ultraviolet-visible spectroscopy

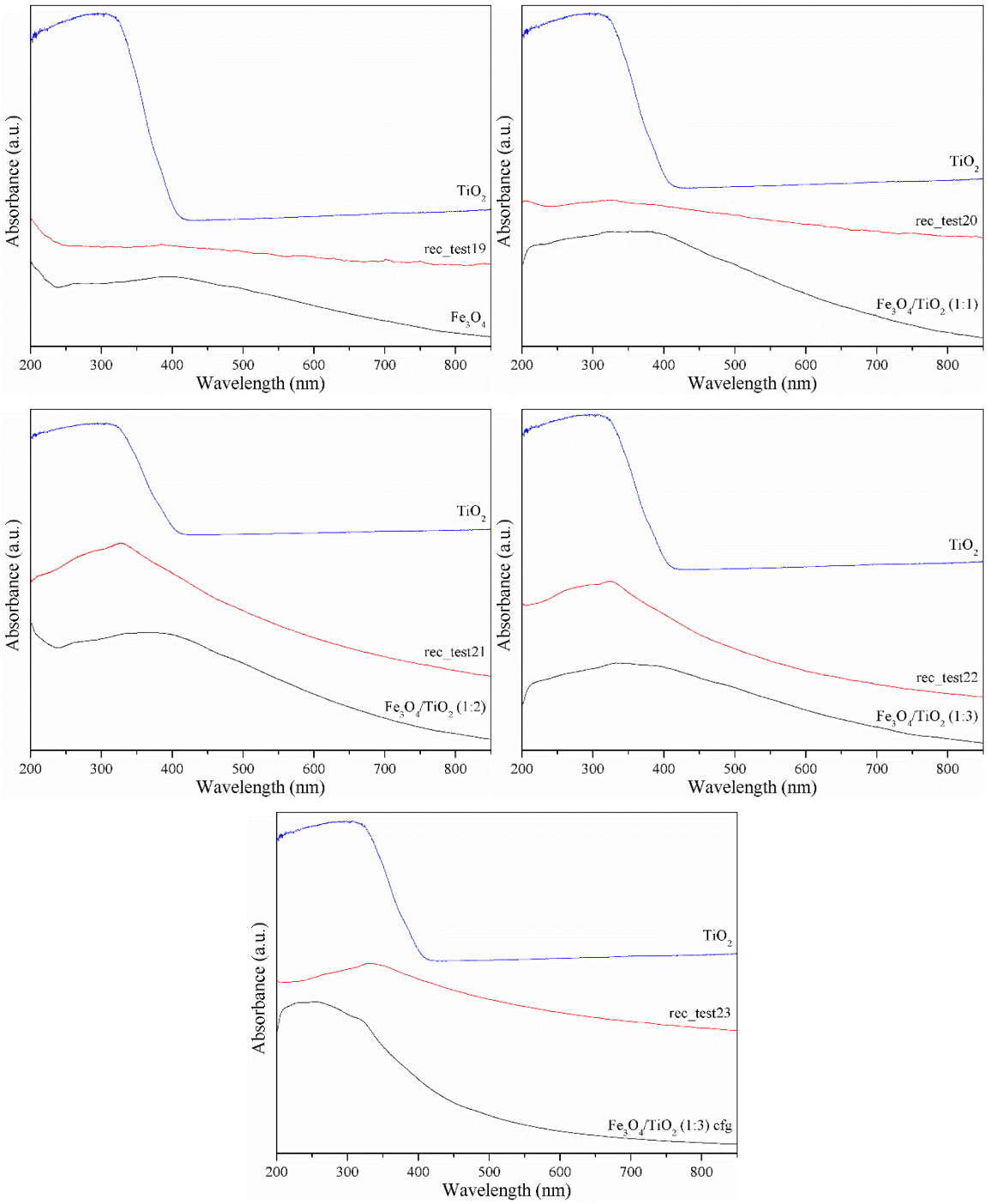

Figure D. 7 - UV-vis spectra of all magnetic nanoparticles prepared (black line) and after two runs of photocatalysis (red line) and spectrum of TiO_2 (blue line).

D.2 - Geopolymer spheres

a) Visual appearance

Sets A and B

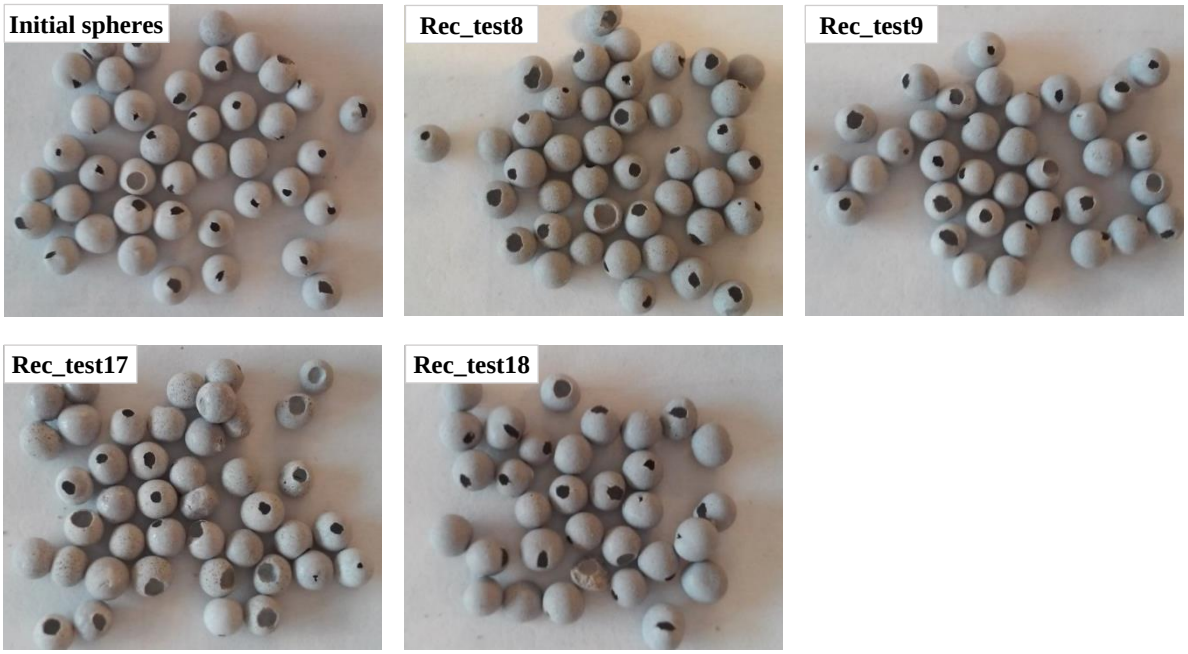

Figure D. 8 - Photography of the geopolymer spheres before and after the photocatalytic treatment, Sets A and B.

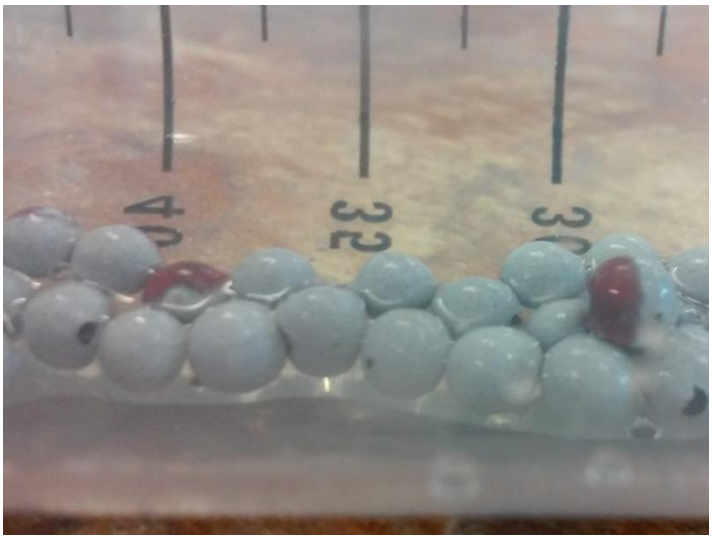

Figure D. 9 - Photography of the geopolymer spheres recovered immediately after the end of the photocatalysis.

Set C

Figure D. 10 - Photography of the geopolymer spheres before and after the photocatalytic treatment, Set C.

a) X-Ray powder diffraction

Sets A and B

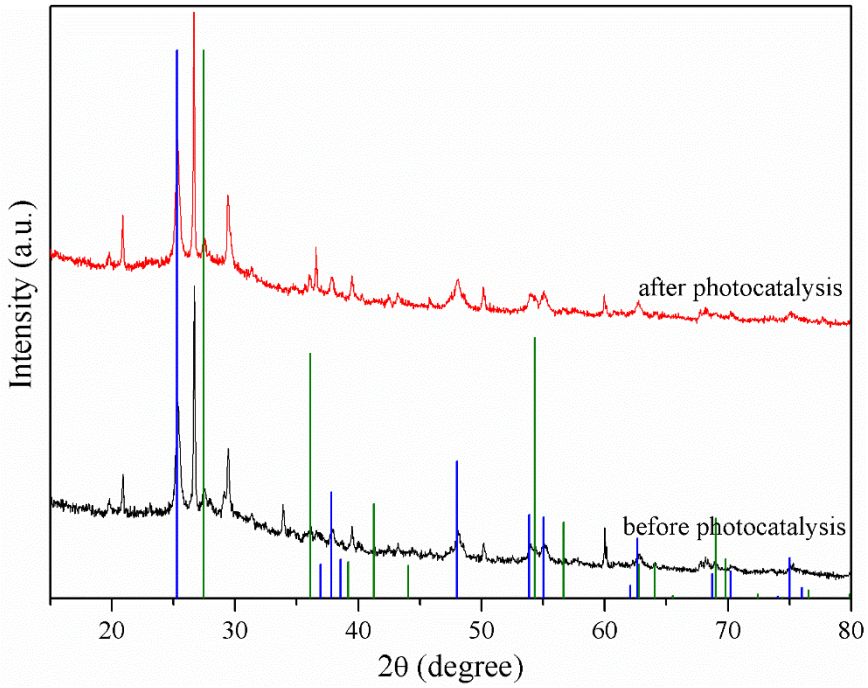

Figure D. 11 – XRD diffractograms of the geopolymer spheres before (black line) and after the test of Set A (red line). Blue vertical straight lines correspond to rutile phase and green lines to anatase phases.

To determine the variation on weight percentage during the photocatalysis, it was used the Equation (D.2).

$$\text{Weight variation (\%)} = \frac{\text{Weight percentage}_{\text{after test}} - \text{Weight percentage}_{\text{before test}}}{\text{Weight percentage}_{\text{before test}}} \times 100 \quad \text{(D.2)}$$

Table D. 2 - Weight percentages of each component present on the geopolymer spheres before and after the photocatalysis (test of Set A) and the variation between that two percentages.

		Weight percentage (%)		Weight variation (%)
		Before test	After test	
Titanium dioxide	Anatase	23.6	21.4	-9.3
	Rutile	2.5	4.2	68.0
Quartz		22.0	21.8	-0.9
Calcite		12.6	17.0	34.9
Muscovite		19.9	35.7	79.4
Trona		19.3	0.0	-100

Set C

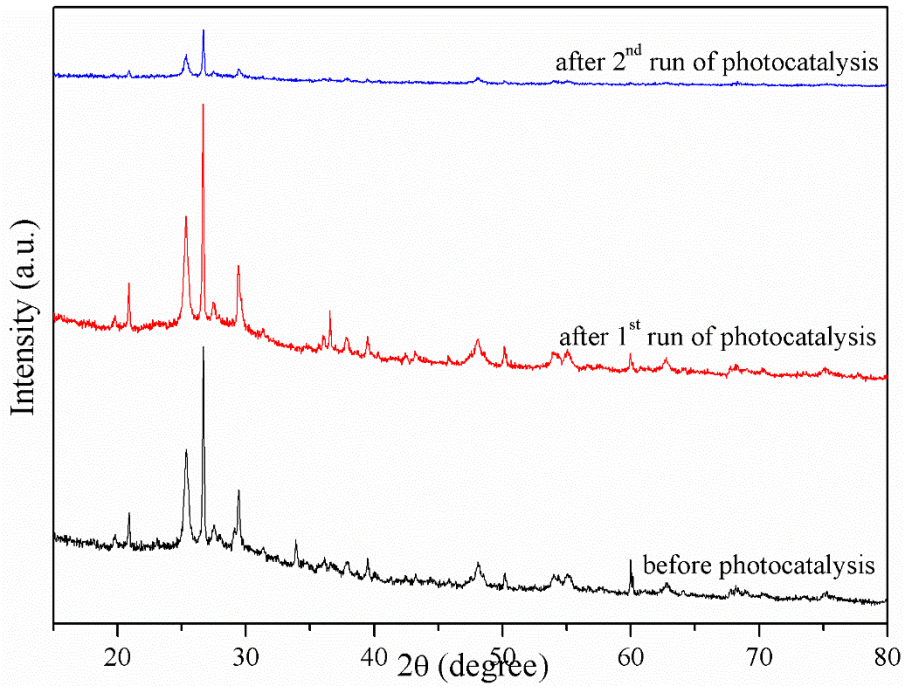

Figure D. 12 - XRD diffractogram of the geopolymer spheres before (black line) and after the test of Set A (red line) and Set C (blue line).

b) Fourier-transformed infrared spectroscopy

Sets A and B

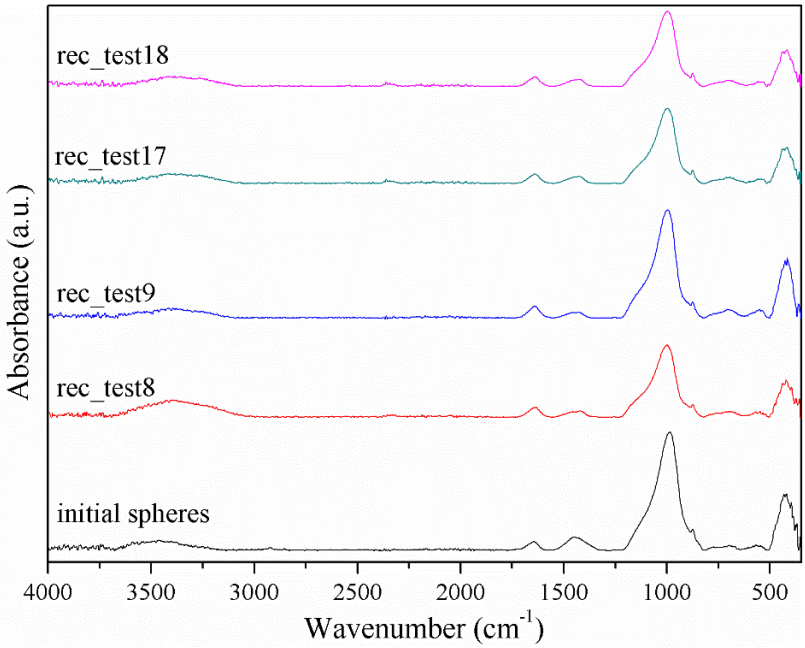

Figure D. 13 - FTIR spectra of the geopolymer spheres prepared (black line) and after photocatalysis, Sets A and B.

Set C

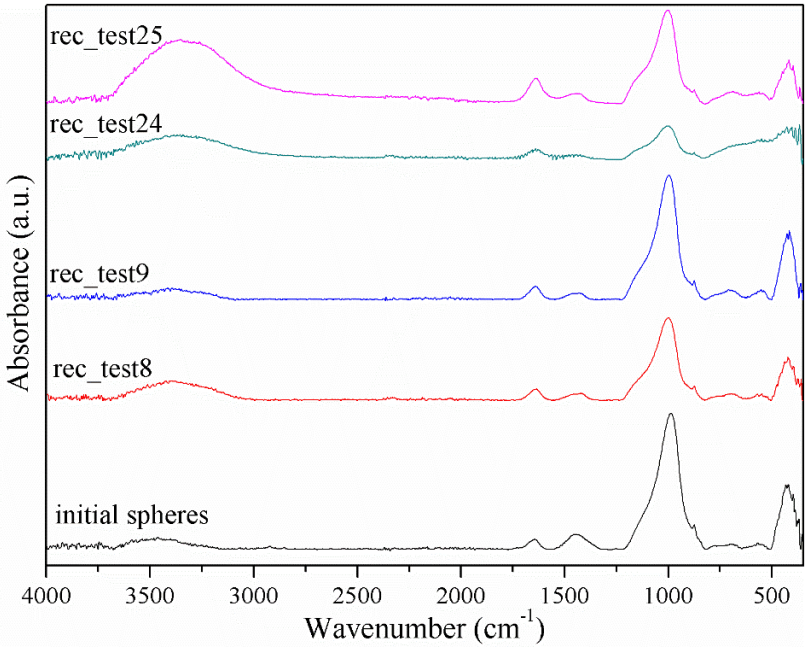

Figure D. 14 - FTIR spectra of the geopolymer spheres prepared (black line) and after photocatalysis, Sets A and C.

c) Ultraviolet-visible spectroscopy

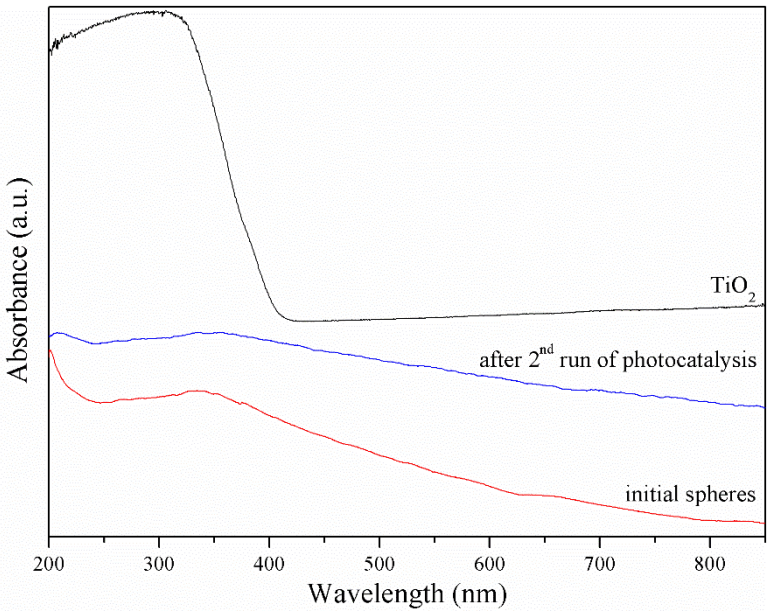

Figure D. 15 - UV-vis spectra of the geopolymer spheres prepared (red line) and after two runs of photocatalysis (blue line) and spectrum of TiO_2 (black line).

d) Optical spectroscopy

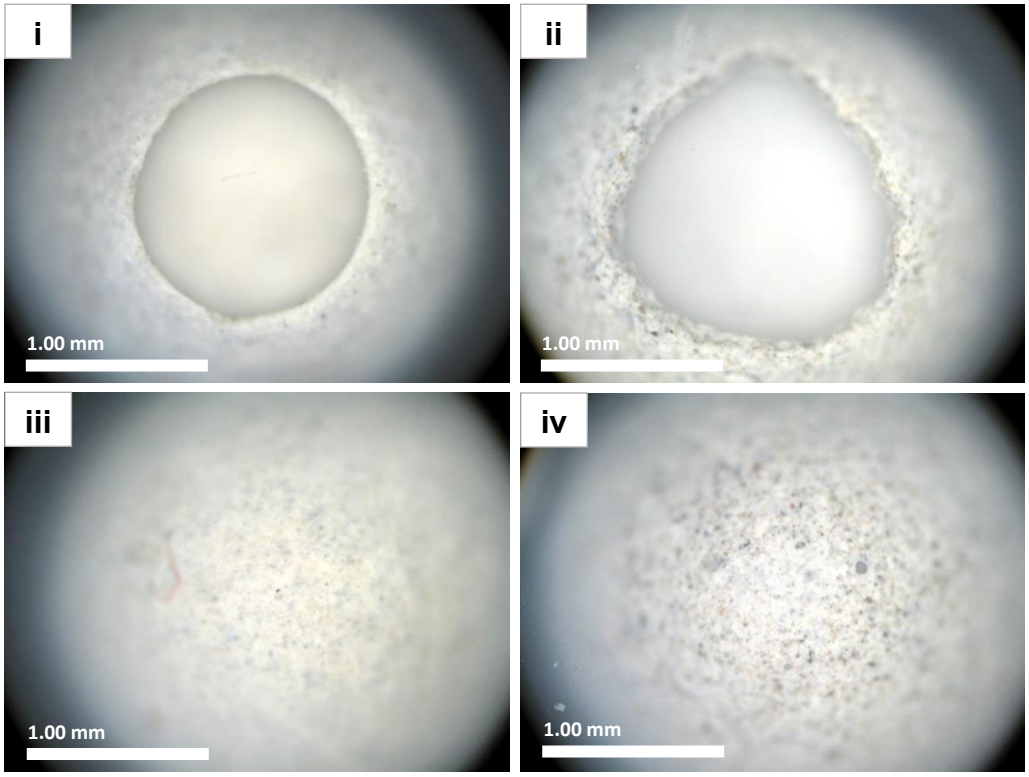

Figure D. 16 - Images of optical microscopy of the geopolymer spheres before (i, iii) and after photocatalysis, test 9 (ii, iv).